University of Massachusetts Amherst

# Electrostatic Effects in Aggregation of Crystallin Proteins



| | |
|---|---|
| Item Type | dissertation |
| Authors | Civay, Deniz Elizabeth |
| DOI | 10.7275/2387381 |
| Download date | 2024-11-24 18:30:19 |
| Link to Item | https://hdl.handle.net/20.500.14394/38878 |

# ELECTROSTATIC EFFECTS IN AGGREGATION OF CRYSTALLIN PROTEINS

A Dissertation Presented

By

DENIZ ELIZABETH CIVAY

Submitted to the Graduate School of the
University of Massachusetts Amherst in partial fulfillment
Of the requirements for the degree of

DOCTOR OF PHILOSOPHY

September 2011

Polymer Science and Engineering

© Copyright by Deniz Elizabeth Civay 2011
All Rights Reserved

ELECTROSTATIC EFFECTS IN AGGREGATION OF CRYSTALLIN PROTEINS

A Dissertation Presented

By

DENIZ ELIZABETH CIVAY

Approved as to style and content by:

Murugappan Muthukumar, Chairperson

Kenneth Carter, Member

Robert Weis, Member

David Hoagland, Department Head
Polymer Science and Engineering

# DEDICATION

To my fiancé Christopher Ziegler, my parents Jim and Sarah Civay, my brothers Greg and Michael Civay, and my puppies Beaker and Lily

ACKNOWLEDGEMENTS

First of all I would like to thank my advisor Professor Murugappan Muthukumar for his guidance and inspiration. My entire committee has been instrumental in the evolution of these projects. Thank you Professor Robert Weis and Professor Kenneth Carter for being on my committee. Your advice on the projects came at important times that helped decide their path. Thank you to Vistakon and the National Science Foundation for your support.

It has been a lot of fun discussing science with all of the group members. Being part of a group of people that have such a variety of strengths and approaches has been invaluable to the process of earning a PhD. Thanks to the Watkins group for making me an "honorary member".

ABSTRACT

ELECTROSTATIC EFFECTS IN AGGREGATION OF CRYSTALLIN PROTEINS

SEPTEMBER 2011

DENIZ ELIZABETH CIVAY, B.A., UNIVERSITY OF WASHINGTON

M.A., UNIVERSITY OF MASSACHUSETTS AMHERST

Ph.D., UNIVERSITY OF MASSACHUSETTS AMHERST

Directed by: Professor Murugappan Muthukumar

The three projects utilized polymer physics theories to investigate polymer aggregation mechanics. Dynamic light scattering (DLS), static light scattering (SLS) and small angle light scattering (SALS) were the primary characterization tools. The goal of the first project was to study the aggregation of bovine $\beta_L$-crystallin and apply that knowledge towards cataract formation, which is caused by aggregation of the crystallins. The first series of experiments characterized the kinetics of $\alpha$-crystallin and $\beta_L$-crystallin in water at room temperature. $\alpha$-crystallin's equilibrium hydrodynamic radius value was kinetically independent. $\beta_L$-crystallin formed an aggregate with an $R_h$ that was kinetically dependent. The packing structure of the aggregate formed by $\beta_L$-crystallin was determined to be loosely packed using SLS. $\alpha$ -crystallin was uniquely demonstrated to be a chaperone in a way that indicated electrostatics played a significant role in aggregation. The role of electrostatics led to an investigation into sodium chloride. Sodium chloride proved to reduce the $\beta_L$-crystallin aggregate size. The next series of experiments simulated biological conditions using a phosphate buffered saline

(PBS). The experiments were performed at 35°C. α -crystallin and $\beta_L$-crystallin were shown to be kinetically independent and demonstrate equilibrium $R_h$ values on the time scale that the experiments were performed. A pH study revealed that multiple size-scales were present only at physiological pH. Above and below physiological pH, only two aggregate size-scales existed. A charge model was made of $\beta_L$-crystallin to compare theory with experimental results. The future goal of project is to reproduce these experiments with human crystallins. In the second project, by changing the order and arrangement of β-spiral elastin (E) and α -helical COMPcc (C) the macroscopic structure was controlled. The EC diblock exhibited a fast and slow mode below the transition temperature of 25°C and single mode behavior above the transition. Phase separation occurred above the transition. CE showed three different size-scales below the transition of 15°C and demonstrated spinodal decomposition above the transition. The ECE triblock demonstrated bimodal behavior below the transition of 25°C and one micellar size above the transition. α-helical COMPcc has the ability to bind to small molecules, making the findings from this project instrumental in creating a drug delivery vehicle. The third project investigated sodium polystyrene sulfonate and polyethylene oxide-polypropylene oxide-polyethylene oxide in solution. Both systems self-assemble into aggregate structures at specific conditions. The significant difference between these two polymers is that sodium polystyrene sulfonate is a polyelectrolyte. It is well known that aggregate structures can be formed by variation in temperature and concentration. However, by having a charged polymer in solution with a neutral polymer the aggregate structure can also be controlled by changing the pH and adding salt to the solution, as was performed in the first project. The third project is an excellent conclusion to the

previous two because it allows for the aggregate structure to be controlled even more so than in the previous projects by mediating the polydispersity index, molecular weight and concentration of each component. Each project focused on a different method of mediating the aggregate structure. A better understanding of aggregation has applications in industry and medicine. Polymer physics theory is instrumental in understanding aggregation mechanics.

TABLE OF CONTENTS

Page

ACKNOWLEDGEMENTS ..... v

ABSTRACT ..... vi

LIST OF FIGURES ..... xii

CHAPTER

1. SELF-ASSEMBLY OF POLYMERS INTO AGGREGATE STRUCTURES ..... 1

1.1 Introduction ..... 1

1.1.1 Relevance ..... 1

1.1.2 Project Overviews ..... 2

1.2 Theories and Methods ..... 4

1.2.1 Electrostatics ..... 4

1.2.2 Dynamic and Static Light Scattering ..... 6

1.2.2.1 Background ..... 6

1.2.2.2 Aggregation Analysis ..... 8

1.2.2.3 Fractal Dimension Analysis ..... 11

1.2.3 Small Angle Light Scattering ..... 14

1.2.3.1 Background ..... 14

1.2.3.2 Aggregation Analysis ..... 14

1.2.3.3 Detailed Instructions ..... 14

1.2.3.3.1 Data Collection ..... 14

1.2.3.3.2 Image Analysis ..... 16

1.2.3.3.2 Data Analysis ..... 17

2. AGGREGATION MECHANISM INVOLVED IN CATARACT FORMATION ..... 18

2.1 Introduction ..... 18

2.2 Materials and Methods ..... 22
2.3 Analysis in Idealized Conditions ..... 24
2.3.1 Evaluation of Equilibrium $R_h$ Values ..... 24
2.3.2 Interaction Between Proteins ..... 35
2.3.3 Determination of Role of Electrostatics Using Salt ..... 38
2.4 Analysis in Biological Conditions ..... 44
2.4.1 Evaluation of Equilibrium $R_h$ Values ..... 44
2.4.2 Interaction Between Proteins ..... 57
2.5 Transmission Electron Microscopy ..... 64
2.6 PH Study ..... 67
2.7 Charge Model ..... 70
2.8 Future Work ..... 71
2.8.1 Depletion Forces ..... 71
2.8.2 Reproduction of Results With Human Crystallins ..... 72
3. LOWER CRITICAL SOLUTION BEHAVIOR OF PROTEIN COPOLYMERS ..... 73
3.1 Introduction ..... 73
3.2 Lower Critical Solution Behavior Theory ..... 74
3.3 Materials and Methods ..... 76
3.3.1 Sample Preparation ..... 76
3.3.2 Light Scattering ..... 79
3.4 Results ..... 79
3.4.1 Analysis of ECE Triblock ..... 79
3.4.2 Analysis of EC Diblock ..... 89
3.4.3 Analysis of CE Diblock ..... 98
3.5 Conclusions ..... 109

3.6 Future Work ..... 112

4. POLYELECTROLYTE COMPLEXATION ..... 113

4.1 Introduction ..... 113

4.2 Materials and Methods ..... 115

4.3 Preliminary Results ..... 117

4.4 Future Work ..... 120

BIBLIOGRAPHY ..... 121

LIST OF FIGURES

Figure Page

Figure 1.1 A schematic of the light scattering set-up used for data collection. ..... 6

Figure 2.1 An illustration of protein aggregation due to denaturation. ..... 18

Figure 2.2 A graph of the conversion of soluble to insoluble proteins for the (a) normal and (b) normal and cataractous lenses.[23] ..... 19

Figure 2.3 An electron micrograph of α-crystallin.[29] ..... 20

Figure 2.4 The (a) monomeric and (b) dimeric form of βB2 crystallin.[32, 33] ..... 21

Figure 2.5 Normalized intensity correlation function data from one of the DLS runs performed on 0.2 mg/mL α-crystallin in water at 23°C. ..... 24

Figure 2.6 A probability distribution function graph of 0.2 mg/mL α-crystallin in water at 23°C. The single peak represents one size-scale being present in the solution, 9 nm. ..... 25

Figure 2.7 A graph of the data points collected from three DLS runs on 0.2 mg/mL α-crystallin in water at 23°C. ..... 26

Figure 2.8 A graph of the average data points of three DLS runs of 0.2 mg/mL α-crystallin in water at 23°C. ..... 26

Figure 2.9 An illustration of the variables used in light scattering. ..... 27

Figure 2.10 This graph shows the kinetic dependence of the hydrodynamic radius of the slow mode of 0.2 mg/mL $\beta_L$-crystallin in water at 23°C. ..... 28

Figure 2.11 The normalized intensity function of one of three DLS runs of 0.2 mg/mL $\beta_L$-crystallin in water at 23°C with $t_{stock}$=214 hours and $t_{tube}$=7 hours. ..... 29

Figure 2.12 A probability distribution function graph of 0.2 mg/mL $\beta_L$-crystallin in water at 23°C. The two peaks represent two size-scales being present in the solution, 2.0 nm and 250 nm. ..... 30

Figure 2.13 The average Γ versus $q^2$ plot of the first peak in the probability distribution functions collected of 0.2 mg/mL $\beta_L$-crystallin in water at 23°C with $t_{stock}$=214 hours and $t_{tube}$=7 hours. ..... 30

Figure 2.14 All of the data collected for the Γ versus $q^2$ plot of the first peak in the probability distribution functions of 0.2 mg/mL $\beta_L$-crystallin in water at 23°C with $t_{stock}$=214 hours and $t_{tube}$=7 hours. ..... 31

Figure 2.15 The average Γ versus $q^2$ plot of the second mean peak in the probability distribution functions collected of 0.2 mg/mL $\beta_L$-crystallin in water at 23°C with $t_{stock}$=214 hours and $t_{tube}$=7 hours. ..... 32

Figure 2.16 All of the data collected for the Γ versus $q^2$ plot of the second peak in the probability distribution functions of 0.2 mg/mL $\beta_L$-crystallin in water at 23°C with $t_{stock}$=214 hours and $t_{tube}$=7 hours. ..... 32

Figure 2.17 An illustration of the dimensions of a subunit of $\beta_L$-crystallin. ..... 33

Figure 2.18 The relative scattered intensity of 0.2 mg/mL $\beta_L$-crystallin in water at 23°C due to the first mean peak, second mean peak and the total intensity. ..... 34

Figure 2.19 A Kratky plot of 0.2 mg/mL $\beta_L$-crystallin in water at 23°C. The closest fit is a fractal dimension of 4.4. ..... 35

Figure 2.20 This is a normalized intensity correlation function from one of three runs performed 0.2 mg/mL $\beta_L$-crystallin, 0.6 mg/mL α-crystallin in water at 23°C..... 36

Figure 2.21 A graph comparing 0.2 mg/mL $\beta_L$-crystallin and 0.2 mg/mL $\beta_L$-crystallin, 0.6 mg/mL α-crystallin in water at 23°C. ..... 36

Figure 2.22 The average Γ versus $q^2$ plot of 0.2 mg/mL $\beta_L$-crystallin, 0.6 mg/mL α-crystallin in water at 23°C. ..... 37

Figure 2.23 A compilation of all of the Γ versus $q^2$ data collected for 0.2 mg/mL $\beta_L$-crystallin, 0.6 mg/mL α-crystallin in water at 23°C. ..... 37

Figure 2.24 The normalized intensity correlation function from one of the DLS runs performed on 0.2 mg/mL $\beta_L$-crystallin with 0.15M NaCl in water at 23°C ..... 39

Figure 2.25 A typical normalized intensity correlation function of 0.2 mg/mL $\beta_L$-crystallin with 0.15M NaCl in water at 23°C. ..... 40

Figure 2.26 A plot of the slow mode of 0.2 mg/mL $\beta_L$-crystallin in water at 23°C with and without 0.15 M NaCl. ..... 41

Figure 2.27 The average Γ versus $q^2$ plot for the second mean peak of 0.2 mg/mL $\beta_L$-crystallin, 0.15 M NaCl in water at 23°C. ..... 42

Figure 2.28 All of the Γ versus $q^2$ data collected for the second mean peak of 0.2 mg/mL $\beta_L$-crystallin, 0.15 M NaCl in water at 23°C. ..... 42

Figure 2.29 The average Γ versus $q^2$ plot for the first mean peak of 0.2 mg/mL $\beta_L$-crystallin, 0.15 M NaCl in water at 23°C. ..... 43

Figure 2.30 All of the Γ versus $q^2$ data collected for the second mean peak of 0.2 mg/mL $\beta_L$-crystallin, 0.15 M NaCl in water at 23°C. 44

Figure 2.31 A normalized intensity correlation function of 0.2 mg/mL α-crystallin in PBS at 35°C. This data is from run one of three runs done on a sample that had a $t_{total}$ time of one month. 45

Figure 2.32 A probability distribution function of 0.2 mg/mL α-crystallin in PBS at 35°C. 46

Figure 2.33 An average Γ versus $q^2$ plot of 0.2 mg/mL α-crystallin in PBS at 35°C with a $t_{total}$ time of one month. 47

Figure 2.34: A Γ versus $q^2$ plot of 0.2 mg/mL α-crystallin in PBS at 35°C. 48

Figure 2.35: The $R_h$ of 0.2 mg/mL α-crystallin in PBS at 35°C is demonstrated have an equilibrium value of 10.0 nm, independent of the time-scale of these experiments. 49

Figure 2.36 The normalized intensity correlation function of 0.2 mg/mL $\beta_L$-crystallin in PBS at 35°C with a $t_{total}$ value of 2 weeks. 50

Figure 2.37 A probability distribution function of 0.2 mg/mL $\beta_L$-crystallin in PBS at 35°C. The two peaks within the reportable range of DLS are highlighted with an arrow. 51

Figure 2.38 An average Γ versus $q^2$ plot of the first mean peak of 0.2 mg/mL $\beta_L$-crystallin in PBS at 35°C. 52

Figure 2.39 A Γ versus $q^2$ plot of all of the data collected on the first mean peak of 0.2 mg/mL $\beta_L$-crystallin in PBS at 35°C. 52

Figure 2.40 An average Γ versus $q^2$ plot of the second mean peak of 0.2 mg/mL $\beta_L$-crystallin in PBS at 35°C. 53

Figure 2.41 A Γ versus $q^2$ plot of the second mean peak of 0.2 mg/mL $\beta_L$-crystallin in PBS at 35°C. 54

Figure 2.42 A plot that established the kinetic independence of the fast mode of 0.2 mg/mL $\beta_L$-crystallin in PBS at 35°C. 54

Figure 2.43 A graph of the slow mode of 0.2 mg/mL $\beta_L$-crystallin in PBS at 35°C. 55

Figure 2.44 The relative scattered intensity of 0.2 mg/mL $\beta_L$-crystallin in PBS at 35oC determined using static light scattering data. 56

Figure 2.45 A Kratky plot of 0.2 mg/mL $\beta_L$-crystallin in phosphate buffered saline (PBS) at 35°C and $t_{total}$ = 5 hours. A fractal dimension of 4.4 was the most accurate fit. This $d_f$ value was verified at other $t_{total}$ values as well. ..... 57

Figure 2.46 The normalized intensity correlation functions of 0.2 mg/mL $\beta_L$-crystallin, 0.6 mg/mL α-crystallin in PBS at 35°C. ..... 58

Figure 2.47 A comparison of the probability distribution functions of 0.2 mg/mL $\beta_L$-crystallin in PBS at 35°C and 0.2 mg/mL $\beta_L$-crystallin, 0.6 mg/mL α-crystallin in PBS at 35°C. The addition of α-crystallin reduces the prevalence of aggregates. .. 59

Figure 2.48 The average Γ versus $q^2$ plot of 0.2 mg/mL $\beta_L$-crystallin, 0.6 mg/mL α-crystallin in PBS at 35°C. ..... 60

Figure 2.49 The Γ versus $q^2$ plot of all of the data collected on 0.2 mg/mL $\beta_L$-crystallin, 0.6 mg/mL α-crystallin in PBS at 35°C. ..... 60

Figure 2.50 A graph of $R_h$ versus $t_{total}$ of 0.2 mg/mL $\beta_L$-crystallin, 0.6 mg/mL α-crystallin in PBS at 35°C. ..... 61

Figure 2.51 A comparison of the fast modes of 0.2 mg/mL $\beta_L$-crystallin in PBS at 35°C, 0.2 mg/mL α-crystallin in PBS at 35°C, and 0.2 mg/mL $\beta_L$-crystallin, 0.6 mg/mL α-crystallin in PBS at 35°C. ..... 62

Figure 2.52 The average Γ versus $q^2$ plot of the second mean peak of 0.2 mg/mL $\beta_L$-crystallin, 0.6 mg/mL α-crystallin in PBS at 35°C. ..... 63

Figure 2.53 The Γ versus $q^2$ plot of all of the data collected for the second mean peak on 0.2 mg/mL $\beta_L$-crystallin, 0.6 mg/mL α-crystallin in PBS at 35°C. ..... 63

Figure 2.54 An illustration of the sample preparation for TEM. ..... 64

Figure 2.55 TEM image of 0.2 mg/mL $\beta_L$-crystallin in water. ..... 64

Figure 2.56 A TEM image of 0.2 mg/mL $\beta_L$-crystallin, 0.6 mg/mL α-crystallin in water. ..... 65

Figure 2.57 TEM image of 0.2 mg/mL α-crystallin in PBS. ..... 66

Figure 2.58 TEM images of 0.2 mg/mL $\beta_L$-crystallin, 0.6 mg/mL α-crystallin in PBS. . 66

Figure 2.59 A graph illustrating the probability distribution functions of 0.2 mg/mL $\beta_L$-crystallin in PBS at 23°C at three different pH values. ..... 67

Figure 2.60 A pH study below physiological pH of 0.2 mg/mL $\beta_L$-crystallin in PBS at 35°C. ..... 68

Figure 2.61 A pH study above physiological pH of 0.2 mg/mL $\beta_L$-crystallin in PBS at 35°C. ..... 69

Figure 2.62 A pH study at physiological pH of 0.2 mg/mL $\beta_L$-crystallin in PBS at 35°C. ..... 69

Figure 2.63 An illustration of the theoretical structure of βb2-crystallin determined using x-ray diffraction.[33] ..... 70

Figure 2.64 These images are still shots taken from a simulation that Jyoti Mahalik made of $\beta_L$-crystallin using the charge distribution model. Image (a) has weak electrostatic interactions and image (b) has strong electrostatic interactions. ..... 71

Figure 3.1 The illustration above depicts the amino acid sequence and corresponding structure of EC, CE and ECE from top to bottom. The molecular weight of EC, CE and ECE is 22,731 Da, 22911 Da and 35,188 Da, respectively. ..... 73

Figure 3.2 Multiple morphologies of the crew-cut aggregates from block copolymers of (a) 200-b-21, (b) 200-b-15, (c) 200-b-8 and (d) 200-b-4.[58] ..... 74

Figure 3.3 A graph showing the LCST behavior of a diblock copolymer in a neutral good solvent with an N equal to 200.[59] ..... 75

Figure 3.4 The normalized intensity correlation function of 0.2 mg/mL ECE in pH 8 water at 5°C. ..... 80

Figure 3.5 The normalized intensity correlation function of 0.2 mg/mL ECE in pH 8 water at 40°C. ..... 81

Figure 3.6 A comparison of the probability distribution functions below, at and above the transition temperature. All data was collected with the goniometer at 50 degrees.. 82

Figure 3.7 A graph of the hydrodynamic radius, $R_h$, versus the temperature of 0.2 mg/mL ECE at pH 8 deionized water. The transition temperature is marked with a dashed line at 25°C. ..... 83

Figure 3.8 The average Γ versus $q^2$ plot of the fast mode of 0.2 mg/mL ECE in pH 8 water at 5°C. ..... 84

Figure 3.9 All of the data collected for a Γ versus $q^2$ plot of the fast mode of 0.2 mg/mL ECE in pH 8 water at 5°C. ..... 85

Figure 3.10 The average Γ versus $q^2$ plot of the slow mode of 0.2 mg/mL ECE in pH 8 water at 5°C. ..... 86

Figure 3.11 All of the data collected for a Γ versus $q^2$ plot of the slow mode of 0.2 mg/mL ECE in pH 8 water at 5°C. ..... 86

Figure 3.12 The average Γ versus $q^2$ plot of 0.2 mg/mL ECE in pH 8 water at 25°C..... 87

Figure 3.13 All of the data collected for a Γ versus $q^2$ plot of 0.2 mg/mL ECE in pH8 water at 25°C..... 87

Figure 3.14 The average Γ versus $q^2$ plot of 0.2 mg/mL ECE in pH 8 water at 40°C..... 88

Figure 3.15 All of the data collected for a Γ versus $q^2$ plot of 0.2 mg/mL ECE in pH 8 water at 40°C..... 88

Figure 3.16 The normalized intensity correlation function of 0.2 mg/mL EC in pH 8 water at 5°C..... 90

Figure 3.17 The normalized intensity correlation function of 0.2 mg/mL EC in pH 8 water at 25°C..... 90

Figure 3.18 The normalized intensity correlation function of 0.2 mg/mL EC in pH 8 water at 5°C..... 91

Figure 3.19 A comparison of the probability distribution functions below and at the transition temperature of 0.2 mg/mL EC in pH 8 water. The measurements were taken with the goniometer set at 55°..... 92

Figure 3.20 The average Γ versus $q^2$ plot of the first mean peak of 0.2 mg/mL EC in pH 8 water at 5°C..... 93

Figure 3.21 All of the data collected in a Γ versus $q^2$ plot of the first mean peak of 0.2 mg/mL EC in pH 8 water at 5°C..... 93

Figure 3.22 The average Γ versus $q^2$ plot of the second mean peak of 0.2 mg/mL EC in pH 8 water at 5°C..... 94

Figure 3.23 All of the data collected in a Γ versus $q^2$ plot of the second mean peak of 0.2 mg/mL EC in pH 8 water at 5°C..... 95

Figure 3.24 The average Γ versus $q^2$ plot of 0.2 mg/mL EC in pH 8 water at 25°C. ..... 96

Figure 3.25 All of the data collected in a Γ versus $q^2$ plot of 0.2 mg/mL EC in pH 8 water at 25°C..... 96

Figure 3.26 A graph of the hydrodynamic radius, $R_h$, versus the temperature of 0.2 mg/mL EC at pH 8 deionized water. The transition temperature is marked with a dashed line at 25°C. ..... 97

Figure 3.27 EC demonstrated evidence of spinodal decomposition, which can be seen from this SALS data taken from a sample of 0.2 mg/mL EC in pH8 water at 25°C. Spinodal decomposition is suggested by the increase in the intensity peak with time. ..... 98

Figure 3.28 A typical normalized intensity correlation function below the transition temperature of 0.2 mg/mL CE in pH 8 water. ..... 99

Figure 3.29 A normalized intensity correlation function at the transition temperature of 0.2 mg/mL CE in pH 8 water. ..... 100

Figure 3.30 A typical normalized intensity correlation function above the transition temperature of 0.2 mg/mL CE in pH 8 water. ..... 100

Figure 3.31 A comparison of the probability distribution functions below and at the transition temperature of 0.2 mg/mL CE in pH 8 water. The goniometer was set at $40^o$ for both measurements. ..... 101

Figure 3.32 A graph showing the two analyzable size-scales produced by 0.2 mg/mL CE in pH8 water using DLS. ..... 102

Figure 3.33 The average $\Gamma$ versus $q^2$ data of the first mean peak of 0.2 mg/mL CE in pH 8 water at $5^oC$. ..... 103

Figure 3.34 All of the $\Gamma$ versus $q^2$ data of the first mean peak of 0.2 mg/mL CE in pH 8 water at $5^oC$. ..... 103

Figure 3.35 The average $\Gamma$ versus $q^2$ data of the second mean peak of 0.2 mg/mL CE in pH 8 water at $5^oC$. ..... 104

Figure 3.36 All of the $\Gamma$ versus $q^2$ data of the second mean peak of 0.2 mg/mL CE in pH 8 water at $5^oC$. ..... 105

Figure 3.37 The average $\Gamma$ versus $q^2$ data of the first mean peak of 0.2 mg/mL CE in pH 8 water at $15^oC$. ..... 106

Figure 3.38 All of the $\Gamma$ versus $q^2$ data of the first mean peak of 0.2 mg/mL CE in pH 8 water at $15^oC$. ..... 106

Figure 3.39 The average $\Gamma$ versus $q^2$ data of the second mean peak of 0.2 mg/mL CE in pH 8 water at $15^oC$. ..... 107

Figure 3.40 All of the $\Gamma$ versus $q^2$ data of the second mean peak of 0.2 mg/mL CE in pH 8 water at $15^oC$. ..... 108

Figure 3.41 SALS data of 0.2 mg/mL CE in pH 8 water indicating spinodal decomposition. ..... 108

Figure 3.42 A sequence analysis of β-spiral elastin where the hydrophobic regions are highlighted in green. ..... 109

Figure 3.43 A sequence analysis of COMPcc where the hydrophobic regions are highlighted in green, the positively charged amino acids are red, and the negatively charged amino acids are blue. ..... 110

Figure 3.44 A sequence analysis of ECE, EC and CE where alternating regions of phobicity are highlighted in yellow. ..... 111

Figure 3.45 A sequence analysis of CEC where alternating regions of phobicity are highlighted in yellow. ..... 112

Figure 4.1 The theoretical graph for a micellar system that follows closed association. 113

Figure 4.2 An illustration of the structure of (a) NaPSS and (b) PEO-PPO-PEO in micelle form and the chemical structure. ..... 115

Figure 4.3 Proposed pearl necklace structure between PAA and pluronic.[71] ..... 116

Figure 4.4 Probability distribution function DLS data collected by Brown *et al.*[13] ... 118

Figure 4.5 A probability distribution function of pluronic showing a peak representative of a small and large size-scale. ..... 118

Figure 4.6 The correlation functions of 0.05 mg/mL pluronic in water at 10$^{o}$C. ..... 119

Figure 4.7 A correlation function 0.1 mg/mL pluronic in water at 10$^{o}$C. ..... 120

# CHAPTER 1

# SELF-ASSEMBLY OF POLYMERS INTO AGGREGATE STRUCTURES

## 1.1 Introduction

### 1.1.1 Relevance

The underlying mechanisms of polymer aggregation have been of considerable interest over the past few decades.[1-3] Light scattering is a powerful characterization technique for analyzing dynamics and studying polymer aggregation at nanometer length-scales.[4-6] The aggregation of three polymer systems was investigated with light scattering. The variables, as pertains to polymer aggregation, explored herein were charge distribution of the polymer, temperature, solubility, pH conditions and salt concentration. One application that will be discussed is the role of protein aggregation in molecular diseases. Another application of interest is polymer aggregate structures used as drug-delivery systems.

This research aims to improve our understanding of molecular diseases at the nano-scale, ultimately determining novel drug delivery mechanisms, and investigates the underlying physics guiding aggregation phenomena. Within this dissertation, an investigation into the aggregation of $\beta_L$-crystallin, protein copolymers, and the complexation between two self-assembling polymers is discussed.

The purpose of studying the aggregation of $\beta_L$-crystallin was to elucidate cataract formation. The presence of cataracts is characterized by opacity in the lens, which is the

result of crystallin aggregation.[7, 8] The lens is primarily composed of α-crystallin, β-crystallin and γ-crystallin.[8] $\beta_L$-crystallin forms two size-scales, an individual $b_L$-crystallin and an aggregate, when in a dilute solution. The data gathered by studying the variables that mediate aggregation of $\beta_L$-crystallin can be used to improve understanding of aggregation that causes cataracts.

The goal of the protein copolymer project was to improve understanding of polymer aggregation in order to design nanostructures for drug delivery. Drug delivery applications were possible in this case because the protein copolymers contained a block which could bind to small molecules.[9]

The third project explored complexation between two polymers that self-assembled under certain conditions. One of the polymers is a polyelectrolyte. It is advantageous to use sodium polystyrene sulfonate because it can be altered to meet experimental criteria. Further, the use of NaPSS is very controlled in terms of impact of molecular forces on aggregation states. Each of the three projects explored a different facet of aggregation with a polyelectrolyte.

### 1.1.2 Project Overviews

The self-assembly of polymers into aggregate systems was analyzed for three different biomolecule-based or polymer systems. One system consisted of a group of proteins called the crystallins, which are involved in cataract formation. The crystallins studied were $\beta_L$-crystallin and α-crystallin. Cataract formation is caused by aggregation of the

crystallins therefore $\beta_L$-crystallin was researched because it aggregates in solution. α-crystallin was selected because it is a molecular chaperone.[10] The kinetics of the aggregation of $\beta_L$-crystallin in a control solution of deionized water at 25°C and physiological conditions were investigated. The packing structure of the aggregate was determined using small angle light scattering (SALS). The role of electrostatics was investigated using salt as an additive. Preliminary experiments were performed with additives in an effort to use depletion forces to reduce the aggregate size. Finally, a simulation of $\beta_L$-crystallin was done by Jyoti Mahalik to compare theory with experimental results.

The second system was made up of multiple arrangements of cartilage oligomeric matrix protein coiled-coil, COMPcc, (C) and β-spiral elastin (E). COMPcc was selected due to its ability to bind small molecules to its hydrophobic pore, 7.3 nm in length and 0.2 nm – 0.6 nm in diameter.[9] β-spiral elastin was chosen because it self-assembled into a helical β-spiral.[11, 12] All three protein copolymers exhibited lower critical solution temperature (LCST) behavior in water. By changing the arrangement of these two proteins different macrostructures were created. The results of this project indicate that these protein copolymers could be used for a tunable drug delivery system.

For the third system, the two polymers investigated were sodium polystyrene sulfonate (NaPSS) and polyethylene oxide-propylene oxide-ethylene oxide (PEO-PPO-PEO) in water at 10°C and 25°C. These polymers were selected because they exist as an isolated chain and an aggregate in solution under specific conditions; NaPSS was also chosen

because it is a polyelectrolyte.[5, 13] The significance of using a polyelectrolyte is that the aggregate structure can be manipulated using electrostatic forces. In the future the aggregation mechanics of PEO-PPO-PEO with polyelectrolytes that have different functional groups can be studied at various pH values to explore the dominant force, be it electrostatics or charge neutral interactions.

All three projects relied on polymer physics to understand aggregation mechanics. Three characterization techniques were primarily used for analysis of these systems; Dynamic light scattering, static light scattering, and small angle light scattering. Electrostatics theory was a significant tool in predicting aggregation behavior.

## 1.2 Theories and Methods

### 1.2.1 Electrostatics

In order to understand why aggregation occurs, the environment and the polymer chain must be studied. The field of electrostatics provides theories that aid in predicting the role of the environment and polymer chain in aggregation. Electrostatics aids in understanding the driving forces for aggregation.

Proteins are made-up of amino acids and typically consist of an irregular distribution of hydrophilic and hydrophobic regions. Depending on the solvent properties and charge distribution, it may be thermodynamically favorable to have either the hydrophobic or hydrophilic regions exposed. The secondary structure of a protein commonly serves to hide the energetically unfavorable amino acid sequence in the interior. If a protein were

to denature, the energetically unfavorable region would become exposed and then seek similar regions on other proteins to once again minimize energy.[14] The result is aggregation. Protein aggregation can also be caused by chemical bonds; however the focus of this paper is electrostatically driven aggregation.

In solution, both long-range and short-range forces exist. Examples of long-range forces are electric potential and electric field. Hydrophobic forces are considered short range because they act over monomeric distances. If a protein solution contained salt, there would be both long-range and short-range forces to consider. The salt would dissolve into cations and anions in solution. Some of these charges would condense on the protein. The other ions would arrange themselves in solution such that they were correlated depending upon their charge.[15, 16]

Electrostatic theories can be applied to experiments to explain aggregation. Some variables that influence the electrostatics are the solution pH and charge distribution of the polymer. The pH of the solution affects polymer morphology; therefore by mediating the pH the polymer conformation can be controlled. Another advantage of applying electrostatic theories is that by doing a charge distribution analysis a model for aggregation can be created. This is accomplished by determining hydrophobic and hydrophilic-dominant regions.

### 1.2.2 Dynamic and Static Light Scattering

#### 1.2.2.1 Background

Dynamic (DLS) and static light scattering (SLS) are powerful techniques that probe polymer properties in dilute solutions. By exposing a dilute polymer solution to a laser beam, and collecting the scattering intensity as a function of angle and time, the system can be described based on its Brownian motion and concentration fluctuations.[4]

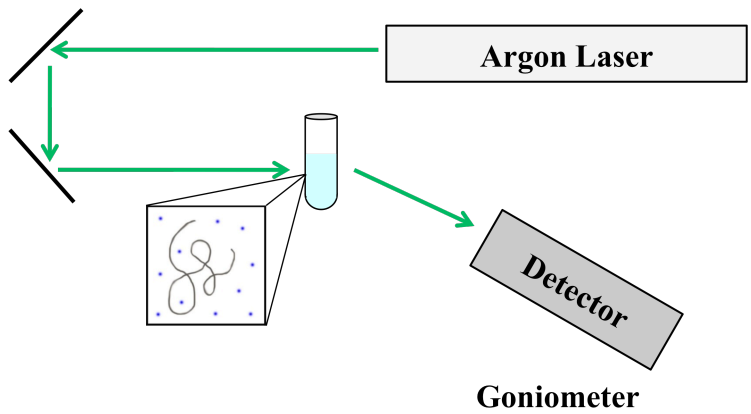


**Figure 1.1 A schematic of the light scattering set-up used for data collection.**

In dynamic light scattering the ALV5000 produces a normalized intensity correlation function of the intensity I(q,t) due to the concentration fluctuations in the system. The axis on the correlation function graph is $g_2(\tau)$ versus log ($\tau$), where $\tau$ is the lag time. The concentration fluctuations are given by the equation below.

**Equation 1.1**

$$\frac{\langle I(q,t)*I(q,t+\tau)\rangle}{\langle I\rangle^2} = g_2(\tau)$$

The variable q is defined as the scattering wave vector and is equal to $4\pi(n/\lambda)\sin(\theta/2)$, $\lambda$ is the wavelength of the scattering radiation in a vacuum, n is the refractive index of the medium, and $\theta$ is the scattering angle.

Next, the ALV5000 correlator is used to produce a probability distribution function. This is done mathematically by first using the Siegert relation, where $g_1(\tau)$ is the Laplace transform of the distribution function $F(\Gamma)$ of decay rates $\Gamma$.

**Equation 1.2**

$$g_2(\tau) = 1 + |g_1(\tau)|^2$$

The y-axis of the probability distribution function is a relative scale dependent on $\tau$ and the x-axis is log ($\tau$). The graph is made up of peaks describing the system being analyzed. If one peak is present, then one size-scale exists in solution. The corresponding x-axis value of the peak is recorded and the inverse is related to $\Gamma$. Typically $F(\Gamma)$ is Laurentzian. A graph of $\Gamma$ versus $q^2$, where q is related to the angle at which the data was collected, gives a slope equal to the diffusion coefficient of the polymer in solution, under the condition that the data follows a linear trendline through the origin. Using the Stokes-Einstein equation, the hydrodynamic radius, $R_h$, can be determined.[4]

**Equation 1.3**

$$D = \frac{k_B T}{6 \pi \eta R_h}$$

In the above equation $k_B$ is the Boltzmann constant, $\eta_o$ is the solvent viscosity, and T is the temperature in Kelvin.

An ALV instrument with an argon laser ($\lambda$ = 514.5 nm) was used to collect the light scattering data from $35^o$-$65^o$ in $5^o$ increments and from $70^o$-$90^o$ in $10^o$ increments. The temperature of the samples was mediated during the experiments using a xylene bath. The samples were each analyzed three times. In the case of kinetic studies, the three runs were performed one after another. The time noted was the average.

**1.2.2.2 Aggregation Analysis**

SLS and DLS are ideal for studying aggregation physics as they provide a means to determine the hydrodynamic radius [10], diffusion coefficient (D), and fractal dimension ($d_f$) of polymers in dilute solutions. Although DLS and SLS are typically used to study solutions with only one isolated chain present in solution, these tools can also be used to analyze aggregates. When aggregates exist in solution the probability distribution function can exhibit one or more peaks, (the probability distribution function is the La Place transform of the normalized intensity correlation function). If an isolated chain and an aggregate are present in solution two peaks appear, corresponding to a fast and a slow mode. The fast mode describes the diffusion of the isolated chain in solution and the slow mode contains information about the collective motion of aggregates. Counterions, ionic strength and dielectric constant can significantly affect the properties of the fast and slow mode.[17-19]

The $\Gamma$ versus $q^2$ data produced by DLS and SLS typically follow a linear relationship such that a trend line through the data points passes through the origin and the slope of the trend line represents the diffusion coefficient. In the case of aggregate analysis the high q-value data points are sometimes found to deviate from the linear trend line to follow an exponential relationship. When the data exhibits this trend it is typically a product of the size-scale being probed. DLS has resolution limits imposed by the laser wavelength utilized. The Argon laser used in the discussed set-up can accurately analyze aggregates on the order of a few hundred nanometers. If an aggregate is so large that it is at the edge of the resolution limit imposed by the laser's wavelength, the laser will probe and analyze local properties of the aggregate instead of global properties. The Stokes-Einstein equation is still valid for determining an approximate $R_h$ value of the aggregate so long as the linear relationship is obeyed at low q-values and the deviation from linearity at high q-values is not significant enough to greatly impact the slope of the trend line.

The advantage of static light scattering over dynamic light scattering is that the molecular weight, second virial coefficient and the radius of gyration can be determined. The molecular weight and radius of gyration can be obtained by creating a Zimm plot. In order to make a Zimm plot multiple sample concentrations must be made and then analyzed at a sequence of at least five different angles. The concentrations chosen for this study must be below the overlap concentration of the sample. Below the overlap concentration the chains remain isolated.

**Equation 1.4**

$$c^* = \frac{3\,M_w}{4\pi N_A R_G^3}$$

In the above equation $M_w$ is the weight averaged molecular weight, $N_A$ is Avagadro's number and $R_G$ is the radius of gyration. The overlap concentration is essentially the mass of one chain divided by the volume of one chain.

A Zimm plot requires the data describing the angular dependence of scattered light for each of the dilute samples. The equation below describes the angular dependence of scattered light mathematically.

**Equation 1.5**

$$\frac{I(0)}{I(q)} = 1 + \frac{R_G^2}{3} q^2 + \ldots$$

The Rayleigh ratio, R, quantifies the scattered intensity, $I_S$, as a function of the incident beam intensity, $I_{total}$ using the distance between the detector and the sample, r, and the scattering volume, V.

**Equation 1.6**

$$R = \frac{I_s\, r^2}{I_{total} V}$$

The Rayleigh ratio can then be used to describe the scattering intensity in terms of polymer concentration, $c_p$, using the following equation.

**Equation 1.7**

$$\frac{kc_p}{R} = \frac{1}{M_w}(1+2A_2M_wc_p + \ldots)$$

The variable k contains information about the refractive index of the solvent and polymer. This equation can be changed into experimental variables by combining is with the equation for the angular dependence of scattered light. The result is the Zimm equation.

**Equation 1.8**

$$\frac{kc_p}{R} = \frac{1}{M_w}(1+R_G^2q^2/3)(1+ 2A_2M_wc_p + \ldots)$$

A trendline for q = 0 has an intercept of $M_w$ and a slope of $A_2$. Extrapolating a line for $c_p$ = 0 creates a trendline with a slope of $R_G$ and $M_w$ as the intercept.

**1.2.2.3 Fractal Dimension Analysis**

The fractal dimension is of particular interest because it indicates the packing of a structure. Static light scattering data on the slow mode can be used to determine the aggregate's fractal dimension by applying a generalized form of the structure factor equation.[5]

In the case of a monodisperse, homogeneous solution being analyzed, one peak will appear in the probability distribution function. This singular peak represents one $R_h$ size being present within the solution. In the case where two peaks occur for a single polymer solution, the peaks generally represent the individual chain and aggregate forms of the

polymer in solution. When multiple size-scales occur within a solution, the relative intensity can be determined for each size-scale based on the weighted integral of each peak that appears for a particular probability distribution per angle. The first step to determine the relative intensities is to determine the integrals of each peak using the equation below.

**Equation 1.9**

$$\int F(\Gamma)\, d\Gamma = {}_{o}\int^{a} F(\Gamma)\, d\Gamma + {}_{a}\int^{b} F(\Gamma)\, d\Gamma = F_1 + F_2$$

The integral evaluated from 0 to a represents a fast decay rate and is known as the fast mode. The second integral is called the slow mode and is evaluated from a to b. The integrals of the fast and slow mode are $F_1$ and $F_1$ respectively. If more than two peaks exist, this equation should be modified by adjusting the limits of the integrals and adding additional integrals. By determining $F_1$ and $F_2$ for each angle and applying the relative weight to the static scattering data collected for each angle, $I(q)_{total}$, using the following three equations the relative scattering intensities due to the individual, $I(q)_1$, and aggregates, $I(q)_2$, can be determined.[20]

**Equation 1.10**

$$I(q)_{total} = I(q)_1 + I(q)_2$$

**Equation 1.11**

$$I(q)_1 = I(q)_{total} \cdot \frac{F_1}{F_1 + F_2}$$

**Equation 1.12**

$$I(q)_2 = I(q)_{total} \cdot \frac{F_2}{F_1 + F_2}$$

It was stated earlier that $qR_g$ must be less than 1 for the Zimm condition to be true. However, for the experiments discussed herein, in the case of large aggregates with a radius of gyration, $R_g$, greater than 100 nm, this condition is violated. When an aggregate is larger than 100 nm the scattering intensity includes information about the fractal dimension, polydispersity, and the local monomer density. Of particular interest is the fractal dimension, $d_f$, as it provides some insight into the shape of the aggregate. In order to back out information about the $d_f$ the relative static intensity data was fitted to the form factor, P(q) in the equation below.

**Equation 1.13** $$P(q) = P(0)*[1+2/(3*d_f)*(qR_g)^2]^{-d_f/2}$$

Where P(0) is the scattered intensity at the 0 angle. Because this value cannot be determined experimentally it must be determined by fitting data. The above equation was rearranged into a linear form, seen below.

**Equation 1.14** $$y = A + (AB)*x$$

Where $y = [I(q)]^{-2/d_f}$, $A = [I(0)]^{-2/d_f}$, $B = 2/(3d_f)*Rg^2$, and $x=q^2$. Different values of $d_f$ were plugged into the equation to determine the best fit. The ideal $d_f$ value can be determined by taking the slope of the graph of ln[I(q)] versus ln(q) multiplied by negative one using the equation below.

**Equation 1.15** $P(q) \alpha (qRg)^{-d_f}$, $qRg>1$

### 1.2.3 Small Angle Light Scattering

#### 1.2.3.1 Background

One of the limitations of DLS and SLS is its resolution (300 nm or less). This limitation is dependent on the wavelength of laser being used in the set-up. To compensate for this limited resolution, small angle light scattering, SALS, can be used to study micron size-scale ranges. The vertical SALS apparatus consisted of a He/Ne laser (l = 633 nm) and a charge-coupled device (CCD) camera as the detector. The laser is directed through the sample, which results in an image. The image differentiates intensity variances with different colors. The intensity fingerprint gives an indication of dominant micron size-scales present in the sample with rings. Anisotropy can be detected by the presence of spots. The theory behind SALS is essentially the same as for static light scattering.

#### 1.2.3.2 Aggregation Analysis

SALS is particularly useful for studying aggregates because the d-spacing, which is the center to center distance between aggregates, can be calculated for polymer systems using this technique. Another advantage of SALS is that it can be used to analyze the turbidity of a sample.

#### 1.2.3.3 Detailed Instructions

##### 1.2.3.3.1 Data Collection

1.) Put your sample in the sample holder

a.) Use a 1 mm pathlength cell

b.) They are typically purchased from Starna cells 37-px-1, and then trimmed to fit the holder at the glass shop

2.) Make sure the wire that communicates the temperature to the computer is touching your sample

3.) Check that the sample holder is level

4.) Adjust the temperature controls as needed

5.) Place a piece of black paper on the stage beneath the sample holder if you plan on doing image analysis, if however, you plan on collecting turbidity measurements make sure that the laser path is unobstructed to the detector.

6.) Turn on the laser

7.) Click the folder, "SALS_modTEMPERATURE"

8.) Click the icon, "salsn_tempMOD_FAST," the program will then open.

9.) Click the "background ON" button so that it displays "background OFF"

10.) Adjust the sampling interval according to your sample

a.) A minimum sampling time of 10 seconds is needed for the image to be captured

b.) A good number to start with is 20 seconds

11.) Adjust the number of samples taken

a.) 200 is a good number to start with, the experiment can be stopped early to if enough data is collected before 200

12.) Once all of the parameters are adjusted turn off the lights

13.) Click the "start video" button

14.) Click the “start experiment” button

15.) Click the run arrow in the upper left corner

16.) Once the image appears click the “stop video” button

17.) The program will display save option when data collection is complete

**1.2.3.3.2 Image Analysis**

1.) After collecting the data and saving it using the data collection program open the folder marked “image analysis” on the desktop

2.) Open the first program listed

3.) You need to tell the program what images to analyze, you do this by entering the file path in the upper left box (second one down)

a.) The program will only let you choose an image, however after clicking that image it is important that you delete the image name leaving only a directory path to a folder.

4.) Next click the “background subtract” button so that it displays “no”

5.) Click the three buttons down the right hand side so that they display “delete” in red

6.) Enter the values for “$R_{inner}$”, “$R_{outer}$”, and “Stop” according to what is displayed on the left hand side, leave the x and y radii as 0, because you do not yet know their values.

7.) Change the start and stop angle to 0 and 360 respectively

8.) Input the pixel/cm ratio and sample height according to the values on the left side

9.) Press the play arrow in the upper left corner

10.) Press stop

11.) Open the folder which is being analyzed, in it two “.dat” files are being produced for every image file analyzed

12.) Rename the I vs q plot for the 1st file produced to “background.dat”

13.) Change the wait time to 0 ms

14.) Find the approximate center of the first image by scrolling the mouse over it and entering the coordinates into the appropriate boxes.

15.) Press play

**1.2.3.3.2 Data Analysis**

1.) Look at the I vs q plot after the background is subtracted

2.) Take the q value for any peaks that occur beyond the initial one and $2\pi/q = d^*$, which gives you the size scale in microns of any features.

# CHAPTER 2

# AGGREGATION MECHANISM INVOLVED IN CATARACT FORMATION

## 2.1 Introduction

In some cases, when a protein unfolds from its native state, charged groups that were previously hidden in the internal structure, become exposed. This can lead to aggregation.

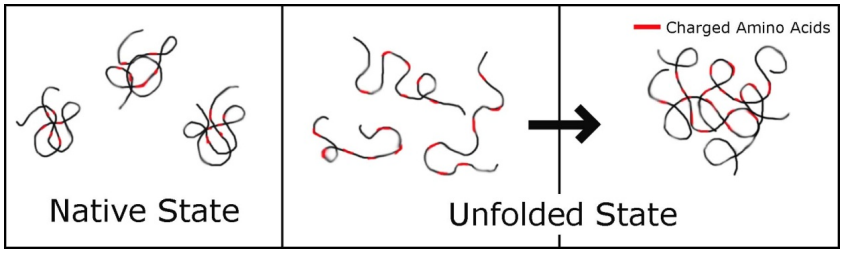


**Figure 2.1 An illustration of protein aggregation due to denaturation.**

Protein aggregation can also occur when the natural protein ratio that occurs in the biological system is not maintained. Many diseases are caused by protein aggregation, such as Alzheimer's disease, Parkinson's disease and cataracts.[7, 21, 22] The conditions for aggregation in the lens of the eye, as it related to cataract formation, were explored by studying $\beta_L$-crystallin.

Cataracts are defined by cloudiness in the lens of the eye. Left untreated, cataracts can lead to vision loss or even blindness. Cataract formation is a serious problem that affects a significant percentage of the population. Of people age 55-64 and 65-74, 45% and 88%, respectively, have cataracts.[14] On the molecular level, opacity within the lens

occurs as a consequence of the aggregation of proteins.[7, 23] By studying these proteins, more can be learned about cataract formation and, subsequently, its prevention.[24]

The lens consists of both soluble and insoluble proteins; together they constitute 35% of the wet weight of the lens. Within a young, healthy lens the soluble proteins, crystallins, constitute 90% of the lens proteins.[25]

As a person suffering from a cataract ages, the amount of crystallins present in the lens decreases as the protein aggregates responsible for cataracts grow.[23] A reduction in the amount of crystallins compromises the health and function of the lens.

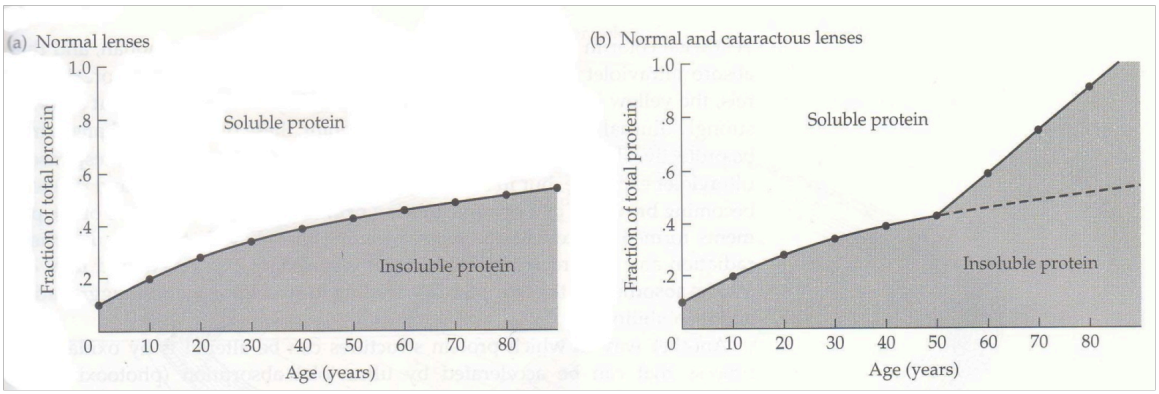


**Figure 2.2 A graph of the conversion of soluble to insoluble proteins for the (a) normal and (b) normal and cataractous lenses.[23]**

The two regions of the lens are the cortex (exterior) and the nucleus (interior).[8] According to the Beaver Dam Study, 60%, 30% and 10% of cataracts are found in the nucleus, cortex and posterior subcapsule, respectively.[26] these regions of the lens define different environments for the aggregation of the crystallins. For example, it has been suggested that as a person ages a barrier forms between the nucleus and cortex.

This barrier is said to prevent the flow of glutathione between the nucleus and cortex. If the glutathione concentration drops below 2mM then protein oxidation and posttranslational modification by reactive small molecules can occur.[27] Due to the two different environments the nucleus and cortex are exposed to, the aggregates found in these two regions are of a slightly different nature. The aggregates found in the cortex are high molecular weight with disulfide bonds, whereas aggregates in the nucleus are large protein-membrane aggregates.[23]

The crystallins in the lens consist of three proteins; α-crystallin, β-crystallin and γ-crystallin. In mammalian lenses, α-crystallin is present in the largest amount at 40-50 wt%. β-crystallin is present at 30-40 wt% and γ-crystallin accounts for 10-40 wt%.[28]

α-crystallin is made up of two subunits, αA and αB. Both subunits are approximately 20 kDa. α-crystallin can contain any combination of the subunits.[28] Although the assembled structure and molecular weight has not yet been determined, electron micrographs reveal α-crystallin to have a diameter of 12 - 15 nm.[29]

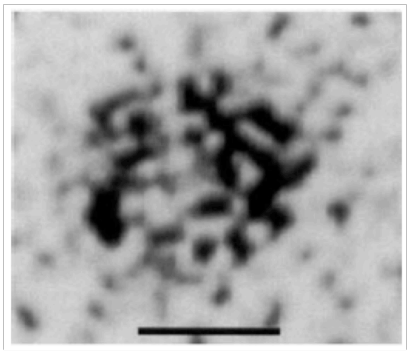


**Figure 2.3 An electron micrograph of α-crystallin.[29]**

β-crystallin consists of two subunits; $\beta_L$-crystallin and $\beta_H$-crystallin.[30] The L and H subscripts is shorthand to indicate low and high molecular weight.[31] $\beta_L$-crystalllin can be further broken down into $\beta_{L1}$ and $\beta_{L2}$. $\beta_{L1}$ is an oligomer and $\beta_{L2}$ is a dimer made up of some combination of βA1, βA2, βA3, βB1, βB2, and βB3.[28] βB2 accounts for 50% of the subunits in the oligomers and is believed to be responsible to aggregation due to its exposed charge distribution.[32]

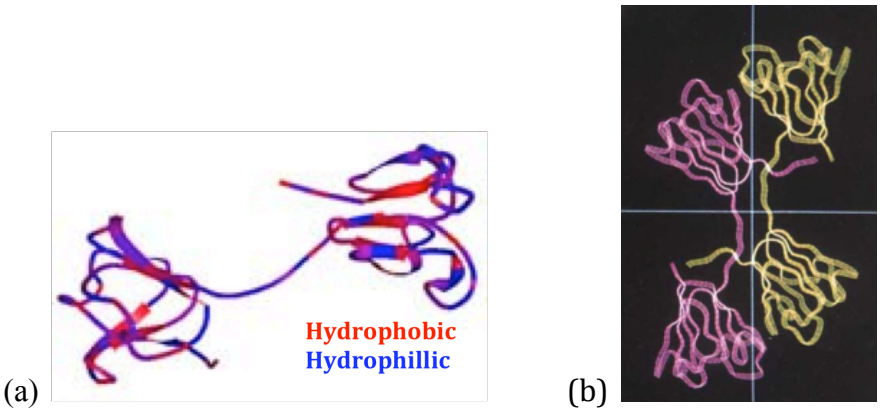


**Figure 2.4 The (a) monomeric and (b) dimeric form of βB2 crystallin.[32, 33]**

The mechanism that the lens relies on for keeping the lens healthy is called the heat shock response. A lens fiber cell will send α-crystallin to refold a protein because α-crystallin can function as a molecular chaperone.[10, 29, 34] Once a lens fiber cell matures it can no longer produce α-crystallin, thereby inhibiting the lens' natural defense mechanism against aggregation.[14] The chaperone ability of α-crystallin is particularly salient to this discussion because the chaperone abilities serve to suppress protein aggregation.[35-38]

Heat shock proteins are categorized based on their molecular weight. α-crystallin is called a small heat shock protein, sHSP, due to its relatively low molecular weight. sHSPs act as molecular chaperones by preventing aggregation of denatured proteins.[39] The prevention of aggregation is accomplished by binding to a partially denatured protein. It is believed that the flexible carboxy-terminal extension is responsible for a sHSP's ability to be a molecular chaperone.[40]

The goal of this project was to determine the origin of clumping of $\beta_L$-crystallin and apply that knowledge to cataract formation in order to gain new insight into the field. In order to learn more about the aggregation of $\beta_L$-crystallin, the interactions of α-crystallin and $\beta_L$-crystallin were studied. The system's electrostatics were also mediated to control the aggregation phenomenon.

**2.2 Materials and Methods**

$\beta_L$-crystallin (C5163 Sigma-Aldrich,) and α-crystallin (C4163 Sigma-Aldrich,) from a bovine eye lens were stored in a biological freezer. The four stock solutions prepared for these experiments were 2.0 mg/mL $\beta_L$-crystallin in water, 2.0 mg/mL $\beta_L$-crystallin in PBS, 2.0 mg/mL α-crystallin in water, and 0.15M NaCl in water. All water used in these experiments was filtered and deionized. A stock solution of 2.0 mg/mL $\beta_L$-crystallin in water was prepared by mixing 10.0 mg of $\beta_L$-crystallin with 5.0 mL water in a decontaminated 20.0 mL scintillation vial. A similar procedure was followed to prepare 2.0 mg/mL α-crystallin in water and 2.0 mg/mL $\beta_L$-crystallin in PBS.

A dilution of these stock solutions was used to create 2.0 mL samples of 0.2 mg/mL $\beta_L$-crystallin in water, 0.2 mg/mL $\alpha$-crystallin in water, 0.2 mg/mL $\beta_L$-crystallin, 0.15M NaCl in water, 0.2 mg/mL $\beta_L$-crystallin, 0.6 mg/mL $\alpha$-crystallin in water, and 0.2 mg/mL $\beta_L$-crystallin in PBS.

The 20 mL scintillation vials were cleaned by sonication for one hour in an extremely dilute solution of Micro-90 surfactant, (Z281506 Sigma-Aldrich) and then rinsed with filtered deionized water eight times and subsequently cleansed with acetone eight times. The crystallin concentrations were verified using an Agilent 8453 UV spectrophotometer equipped with ChemStation software. The molar absorptivity of $\alpha$-crystallin and $\beta_L$-crystallin at 280 nm is 0.75 and 1.3, respectively.[41]

For the pH study, the 2.0 mg/mL $\beta_L$-crystallin in PBS stock solution was used to create the samples tested. HCl and NaOH served to mediate the pH. The pH was checked periodically to ensure a stable reading.

An ALV instrument with an Ar laser ($l$ = 514.5 nm) was used to collect the dynamic light scattering (DLS) data from $35^o$-$65^o$ in $5^o$ increments and from $70^o$-$90^o$ in $10^o$ increments. An ALV5000 correlator was used to analyze the data.

## 2.3 Analysis in Idealized Conditions

### 2.3.1 Evaluation of Equilibrium $R_h$ Values

The initial experiments were carried out to characterize α-crystallin and $\beta_L$-crystallin in water at room temperature. A temperature of 23°C and water as solvent was selected as a control. When 0.2 mg/mL of α-crystallin in water at 23°C was analyzed with dynamic light scattering (DLS), it was determined that only one size-scale was present in solution. This size-scale corresponded to an $R_h$ of 9 nm. Based on the molecular weight of α-crystallin's subunits, and the possibility of forming a hollow sphere, there are from 20 to 30 subunits in the structure.[42]

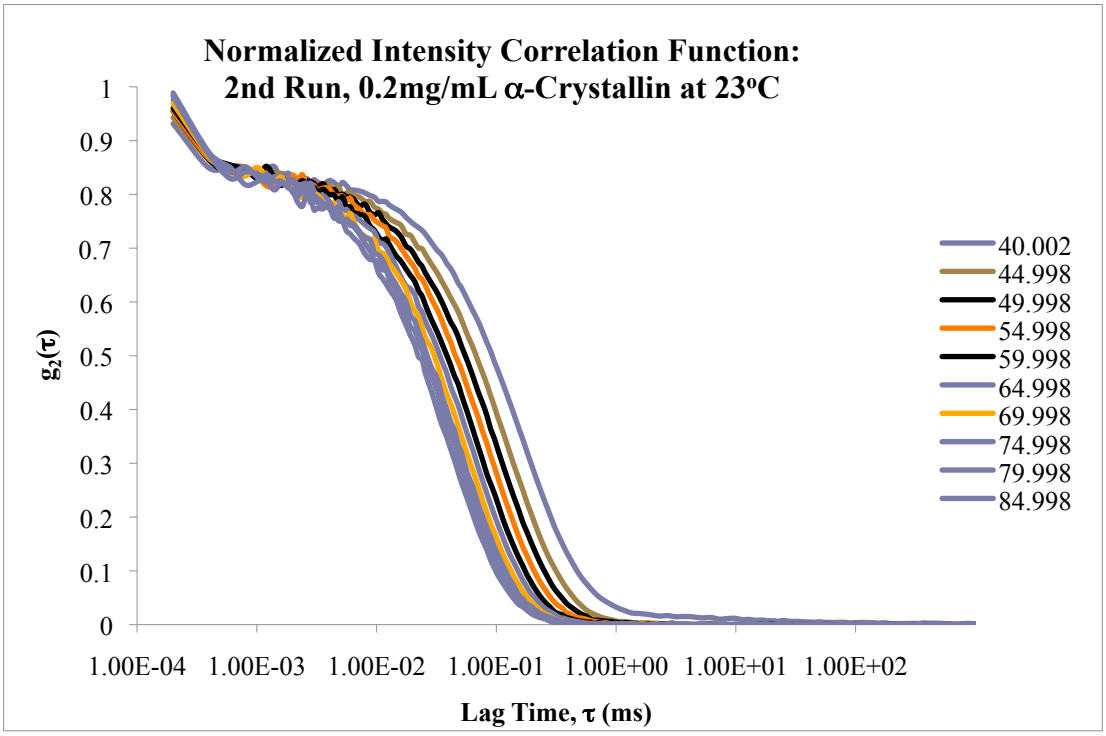


**Figure 2.5 Normalized intensity correlation function data from one of the DLS runs performed on 0.2 mg/mL α-crystallin in water at 23°C.**

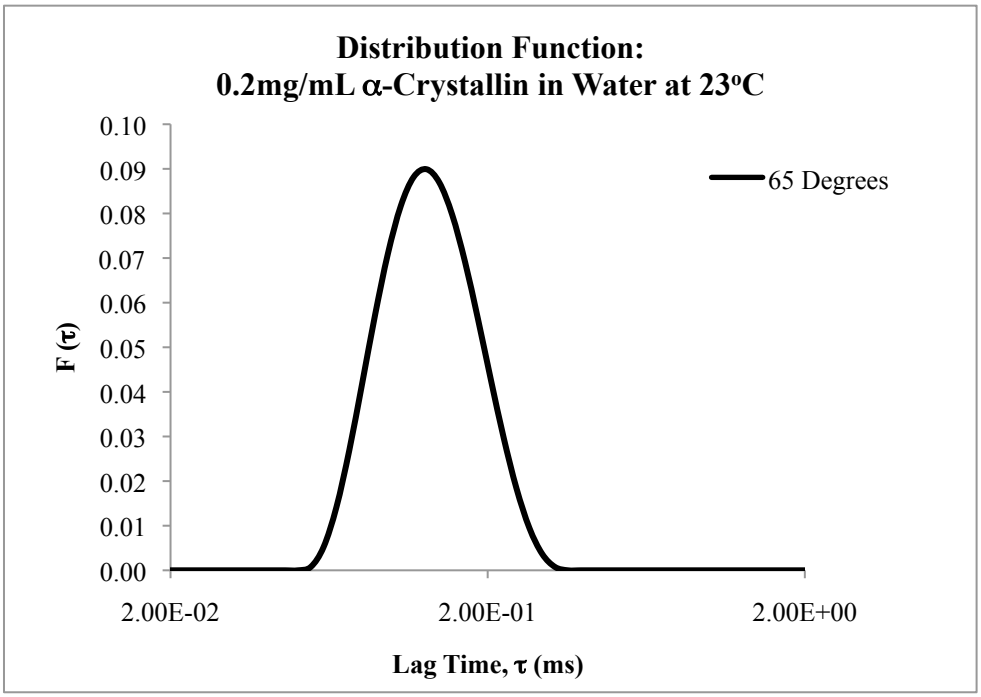


**Figure 2.6 A probability distribution function graph of 0.2 mg/mL α-crystallin in water at 23°C. The single peak represents one size-scale being present in the solution, 9 nm.**

The best way to confirm the accuracy of DLS results run each sample three times and make two plots. One plot should include all of the data points collected and the other plot should illustrate the average data point for each angle. By comparing the fits, or $R^2$ values, of these plots the accuracy of the data can be ascertained. The closer that $R^2$ is to one, the better the fit. Both graphs should demonstrate similar fits.

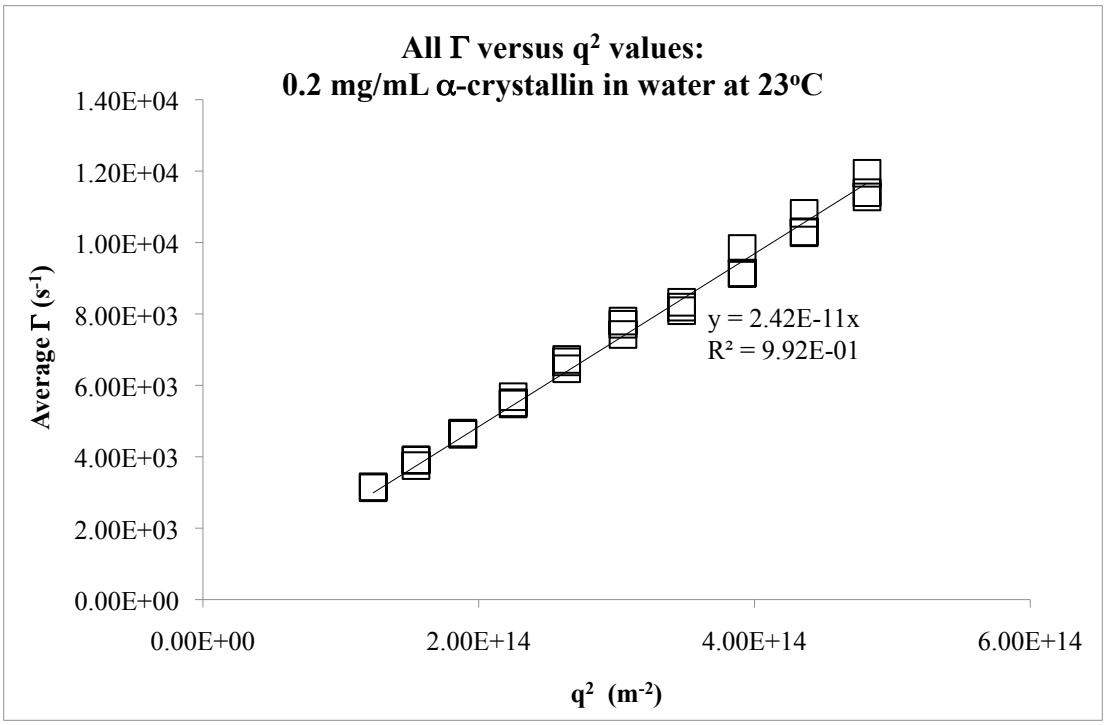


**Figure 2.7 A graph of the data points collected from three DLS runs on 0.2 mg/mL α-crystallin in water at 23°C.**

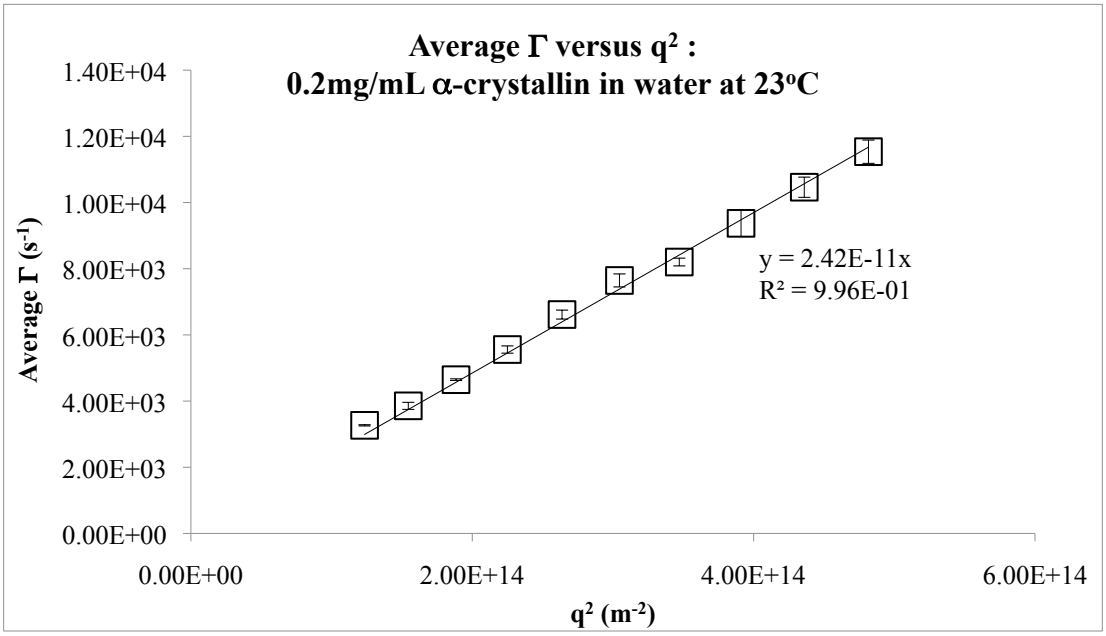


**Figure 2.8 A graph of the average data points of three DLS runs of 0.2 mg/mL α-crystallin in water at 23°C.**

A comparison of the $R^2$ values of the two previous graphs confirms that there were no unexplainable deviations during data acquisition. Both $R^2$ values are extremely close to one and therefore the result of 9 nm is accurate.

In contrast to α-crystallin, $\beta_L$-crystallin demonstrated a bimodal probability distribution function at 23°C in water. The two peaks were indicative of two size-scales being present in solution. The first peak, fast mode, gave information about the $R_h$ of one isolated $\beta_L$-crystallin in solution. The second peak, slow mode, was representative of an aggregate. The next step was to establish if the kinetics of aggregation were occurring on a time-scale that would impact data collection.

The samples that were analyzed were diluted from a stock solution. The stock solution was 2.0 mg/mL $\beta_L$-crystallin in water and the dilute solution was 0.2 mg/mL $\beta_L$-crystallin in water. Because concentration can affect the kinetics of aggregation, three variables were established: $t_{stock}$, amount of time sample existed in a concentrated state before being diluted, $t_{tube}$, amount of time sample existed in dilute state before light scattering data was collected, and $t_{total}$, which is equal to the sum of $t_{stock}$ and $t_{tube}$.

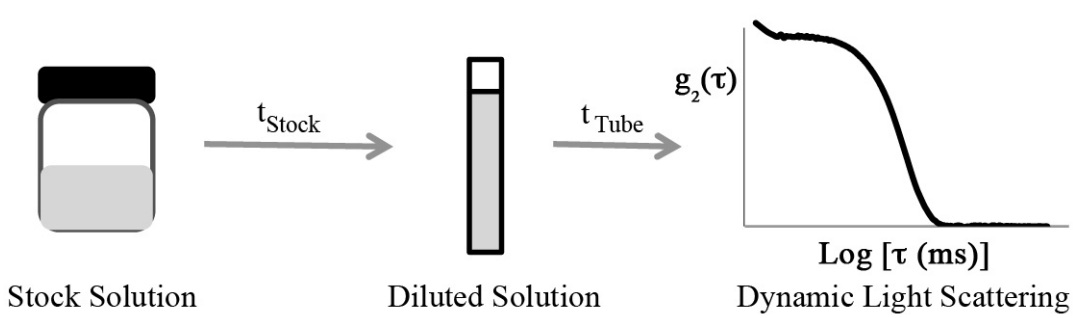


**Figure 2.9 An illustration of the variables used in light scattering.**

The two $t_{stock}$ values chosen for this experiment were 5 hours and 214 hours. The $t_{tube}$ values were 1, 4, 7, 20, and 216 hours. It was concluded that the $R_h$ of the aggregate was kinetically dependant in the water control solution.

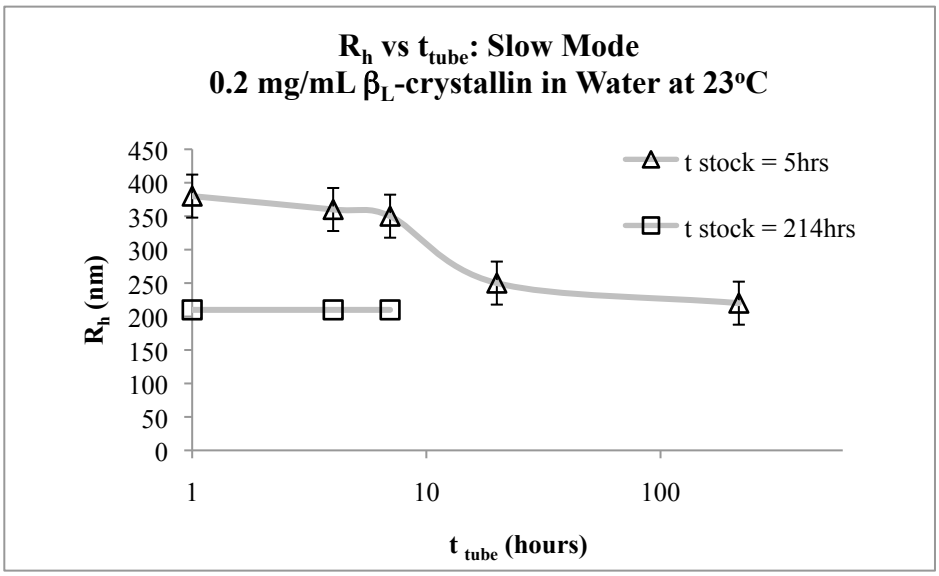


**Figure 2.10 This graph shows the kinetic dependence of the hydrodynamic radius of the slow mode of 0.2 mg/mL $\beta_L$-crystallin in water at 23°C.**

An equilibrium aggregate structure was reached when the 2.0 mg/mL $\beta_L$-crystallin in water sample was refrigerated at 3°C for three days ($t_{stock}$ = 72 hours) and then diluted to 0.2 mg/mL ($t_{tube}$=1 hour) and analyzed. The final conclusion was that $t_{total} \geq 73$ hours resulted in equilibrium $R_h$ values. The equilibrium $R_h$ values were 2.0 nm and 250 nm.

The normalized intensity correlation function of $\beta_L$-crystallin differs from $\alpha$-crystallin's in the shape of the curve, as can be seen in the figure below. $\beta_L$-crystallin's normalized intensity correlation function takes longer to decay to zero than $\alpha$-crystallin's did. The

change in shape is indicative of a multi-modal probability distribution function, and therefore multiple size-scales being present in solution.

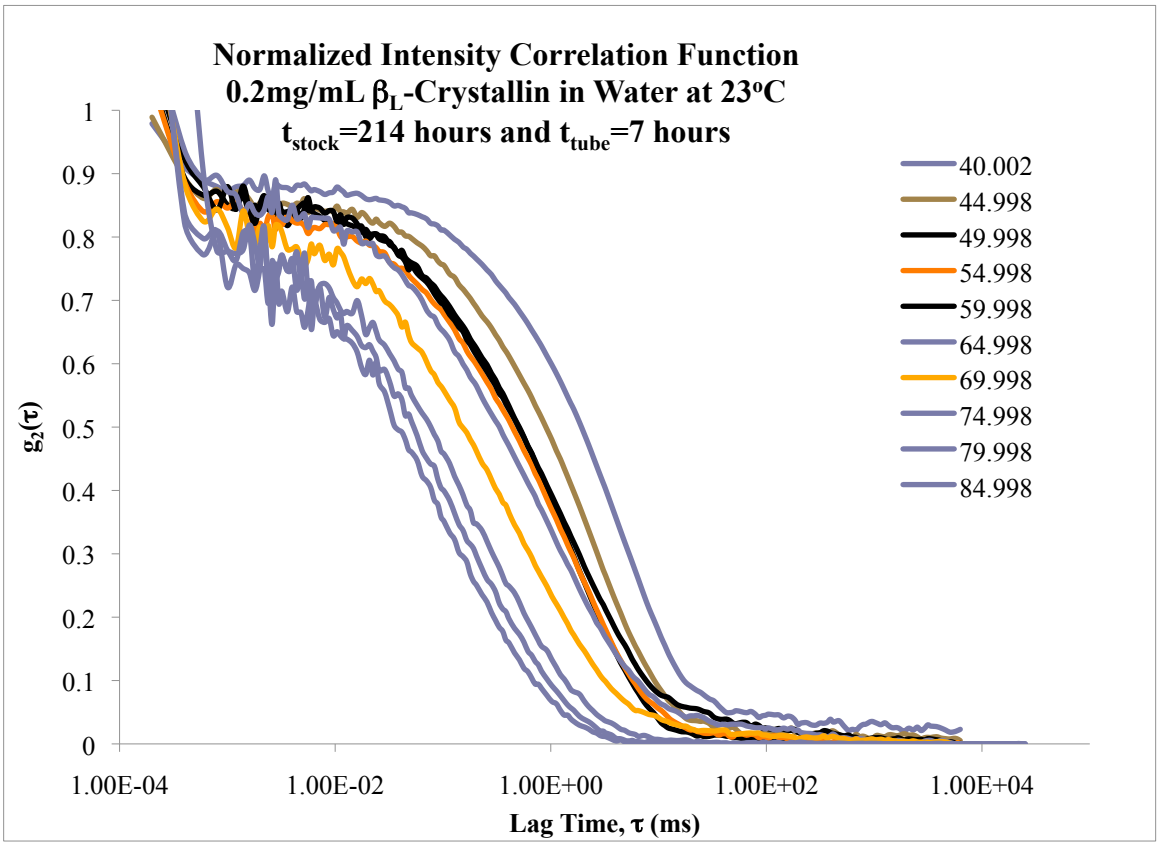


**Figure 2.11 The normalized intensity function of one of three DLS runs of 0.2 mg/mL $\beta_L$-crystallin in water at 23°C with $t_{stock}$=214 hours and $t_{tube}$=7 hours.**

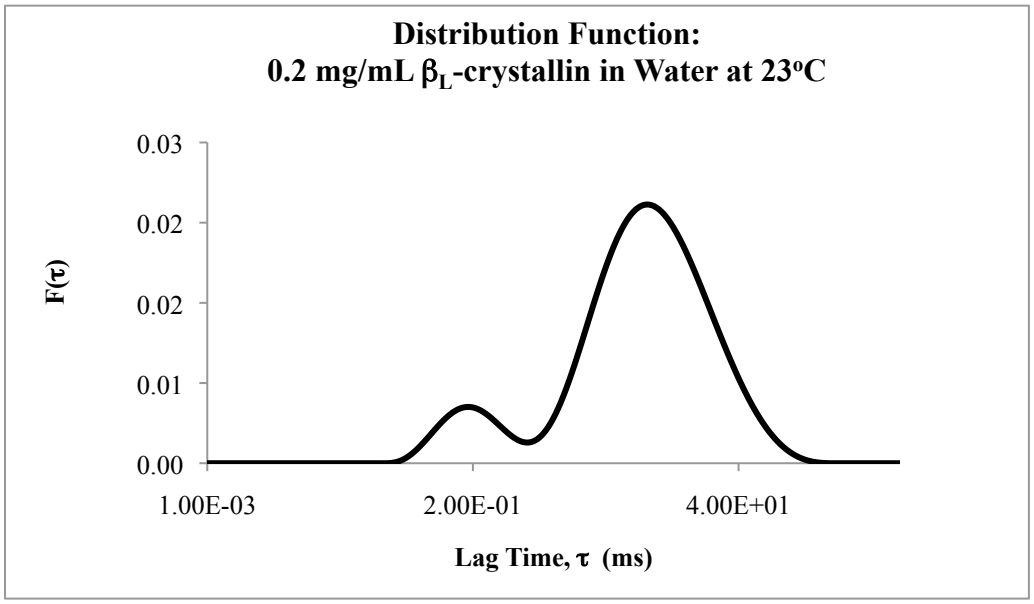


**Figure 2.12 A probability distribution function graph of 0.2 mg/mL $\beta_L$-crystallin in water at 23°C. The two peaks represent two size-scales being present in the solution, 2.0 nm and 250 nm.**

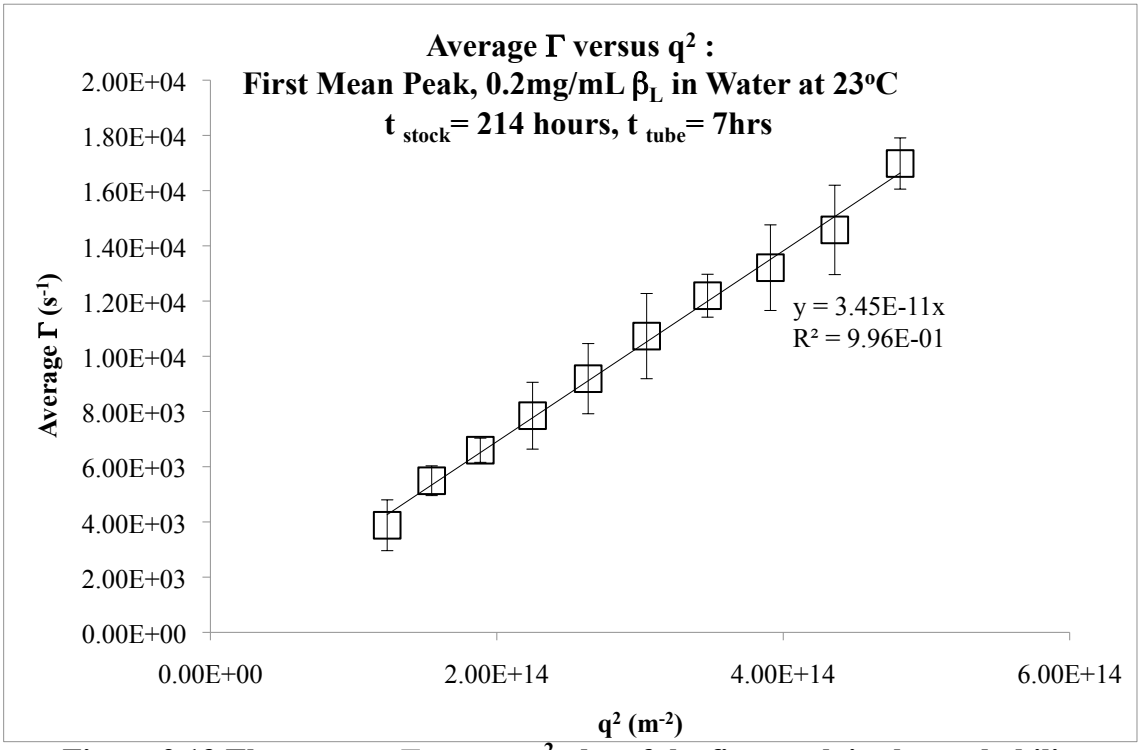


**Figure 2.13 The average Γ versus $q^2$ plot of the first peak in the probability distribution functions collected of 0.2 mg/mL $\beta_L$-crystallin in water at 23°C with $t_{stock}$=214 hours and $t_{tube}$=7 hours.**

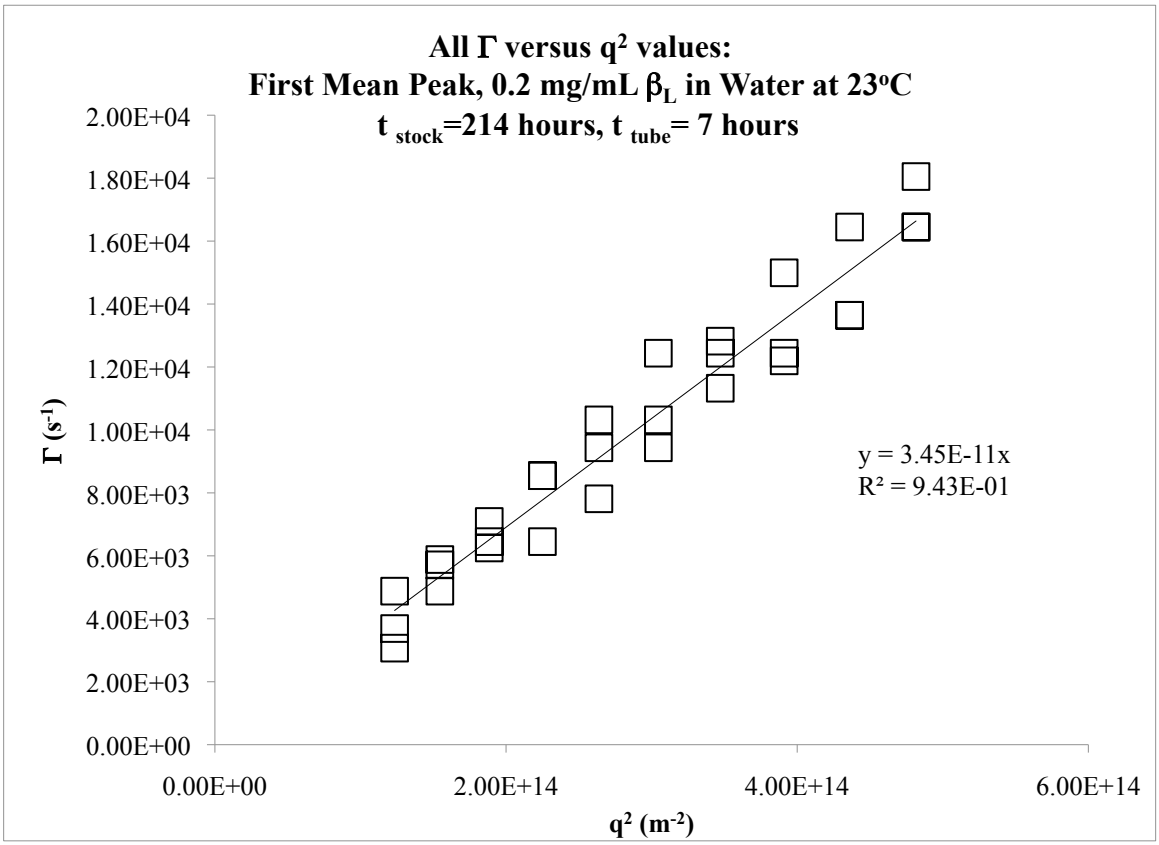


**Figure 2.14 All of the data collected for the Γ versus $q^2$ plot of the first peak in the probability distribution functions of 0.2 mg/mL $\beta_L$-crystallin in water at 23°C with $t_{stock}$=214 hours and $t_{tube}$=7 hours.**

A comparison of the average data points and all of the data points for the Γ versus $q^2$ plot of the first peak in the probability distribution function of 0.2 mg/mL $\beta_L$-crystallin in water at 23°C with $t_{stock}$=214 hours and $t_{tube}$=7 hours reveal no significant deviations in the data collected. The comparison of these two plots confirms the validity of the hydrodynamic radius value reported for the first mean peak. These graphs were created for $t_{total}$ time tested.

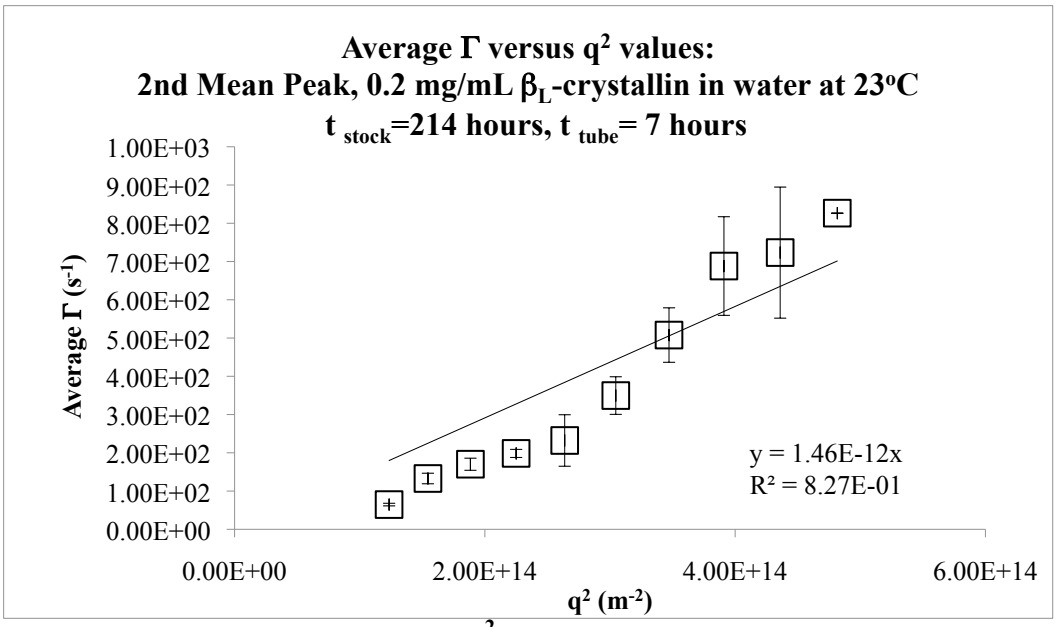


**Figure 2.15 The average Γ versus $q^2$ plot of the second mean peak in the probability distribution functions collected of 0.2 mg/mL $\beta_L$-crystallin in water at 23°C with $t_{stock}$=214 hours and $t_{tube}$=7 hours.**

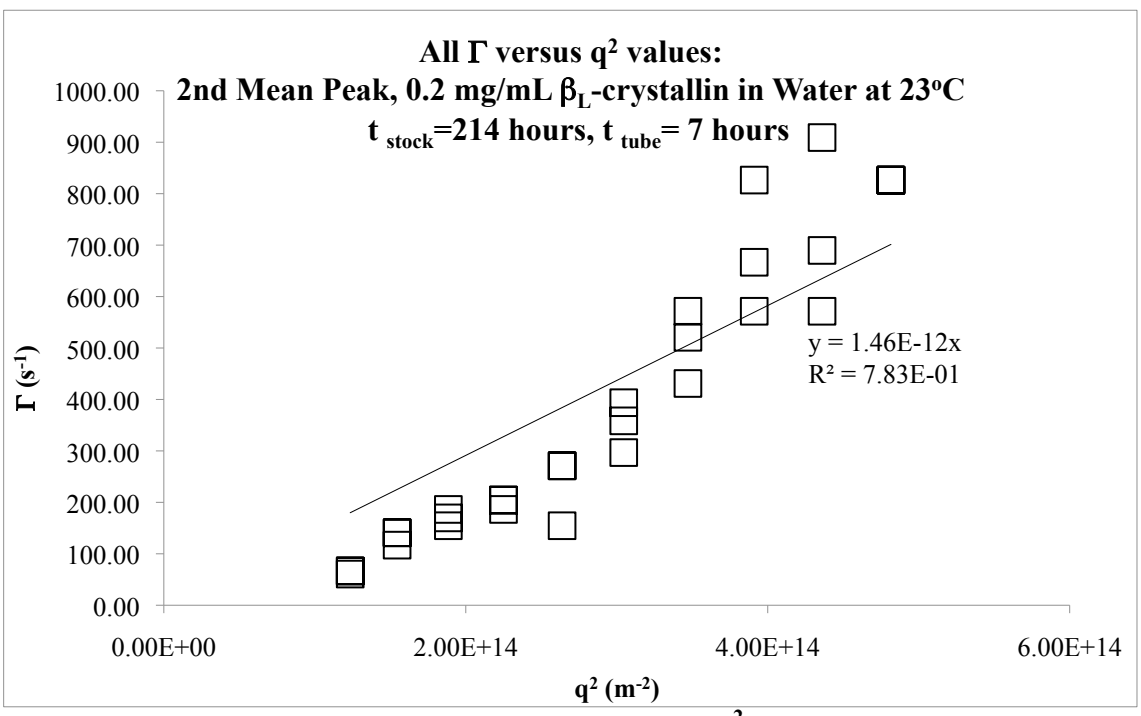


**Figure 2.16 All of the data collected for the Γ versus $q^2$ plot of the second peak in the probability distribution functions of 0.2 mg/mL $\beta_L$-crystallin in water at 23°C with $t_{stock}$=214 hours and $t_{tube}$=7 hours.**

The second mean peak of 0.2 mg/mL $\beta_L$-crystallin in water at 23°C with $t_{stock}$=214 hours and $t_{tube}$=7 hours has a lower $R^2$ value than for the first mean peak. The lower $R^2$ value could either mean that the aggregate structure is changing on the time-scale of the experiment or that there is a distribution of aggregate size-scales present in the solution. In either case the reported hydrodynamic value is less accurate than for the first mean peak.

If the data from the second mean peak is split into the low angle and the high angle data, it appears that at high angles there is a deviation from a linear $q^2$ relationship. If this deviation were more severe, then the hydrodynamic value would not be accurate. However, in this case, the linear $q^2$ relationship is valid and the reported hydrodynamic radius gives an excellent indication of the aggregate size-scale.

$\beta_L$-crystallin's equilibrium values of 2.0 nm and 250 nm potentially correspond to a single subunit and an oligomeric structure. Assuming packing consistent with the dimmers and trimers, there could be as many as one million subunits in the oligomer.

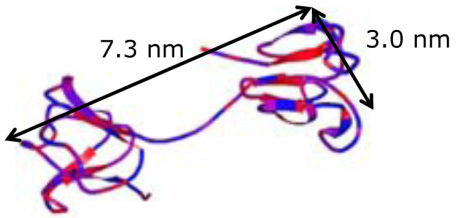


**Figure 2.17 An illustration of the dimensions of a subunit of $\beta_L$-crystallin.**

Once the kinetics of the aggregate structure formed by $\beta_L$-crystallin was systematically characterized, the internal packing of the aggregate was analyzed using SLS data collected simultaneously with the DLS data. By partitioning the relative scattered intensity due to each size-scale present in solution, the fractal dimension, $d_f$, of the aggregate was determined.

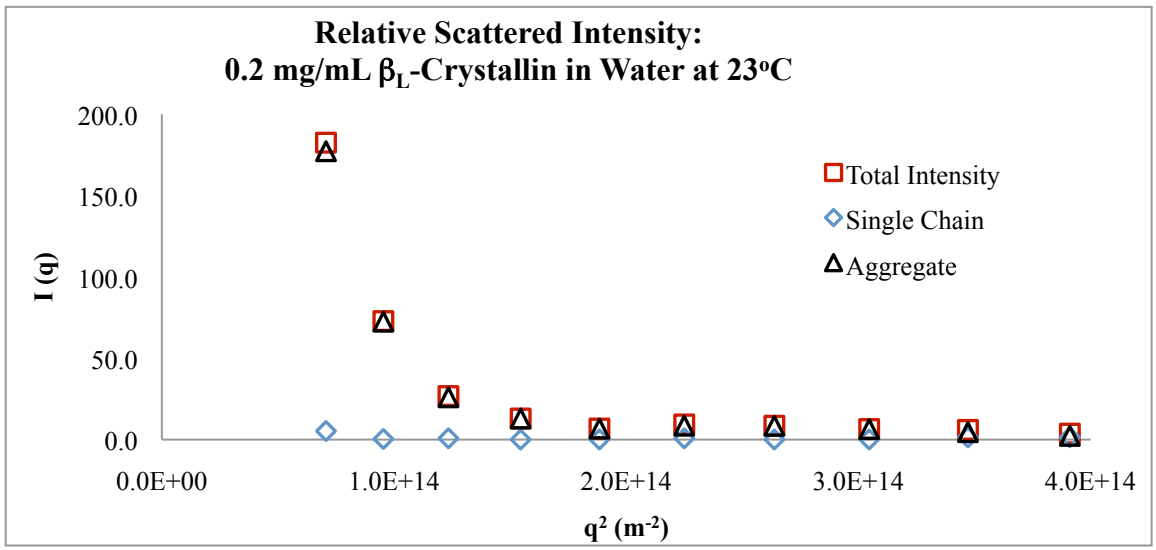


**Figure 2.18 The relative scattered intensity of 0.2 mg/mL $\beta_L$-crystallin in water at 23°C due to the first mean peak, second mean peak and the total intensity.**

Fractals are irregularly shaped objects that must be defined by the fractal dimension. An important property of fractals is self-similarity, which is defined as the substructure representing the form of the superstructure. The fractal dimension gives an indication of how completely a fractal fills the available space.[43] The $d_f$ was determined to be 4.4 for the aggregate formed by $\beta_L$-crystallin in water. This indicated a polydisperse, loosely packed branched structure.[44]

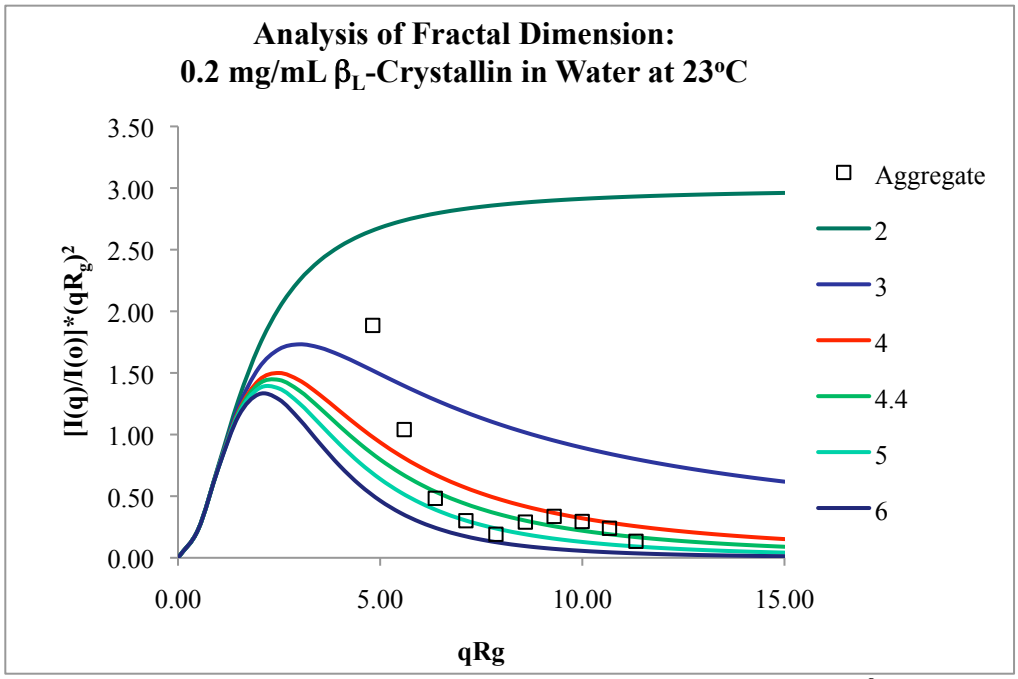


**Figure 2.19 A Kratky plot of 0.2 mg/mL $\beta_L$-crystallin in water at 23°C. The closest fit is a fractal dimension of 4.4.**

### 2.3.2 Interaction Between Proteins

To study the interactions between α-crystallin and $\beta_L$-crystallin, the proteins were added in a 3:1 ratio in order to mimic the relative weight percent ratios that are present in a healthy lens.[8] The sample concentration was 0.2 mg/mL of $\beta_L$-crystallin and 0.6 mg/mL of α-crystallin in water at 23°C. When DLS was used, only one mode appeared in the probability distribution function. This mode was representative of a homogeneously dispersed solution with only one $R_h$ present, 10.0 nm.

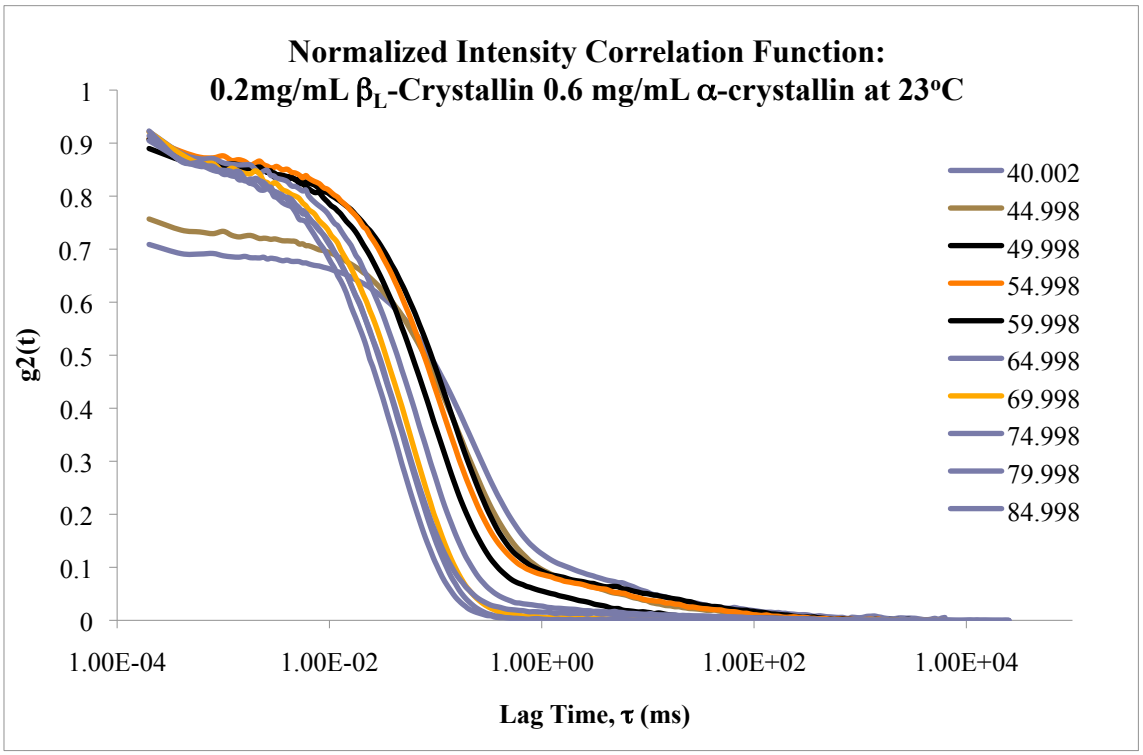


**Figure 2.20 This is a normalized intensity correlation function from one of three runs performed 0.2 mg/mL $\beta_L$-crystallin, 0.6 mg/mL α-crystallin in water at 23°C.**

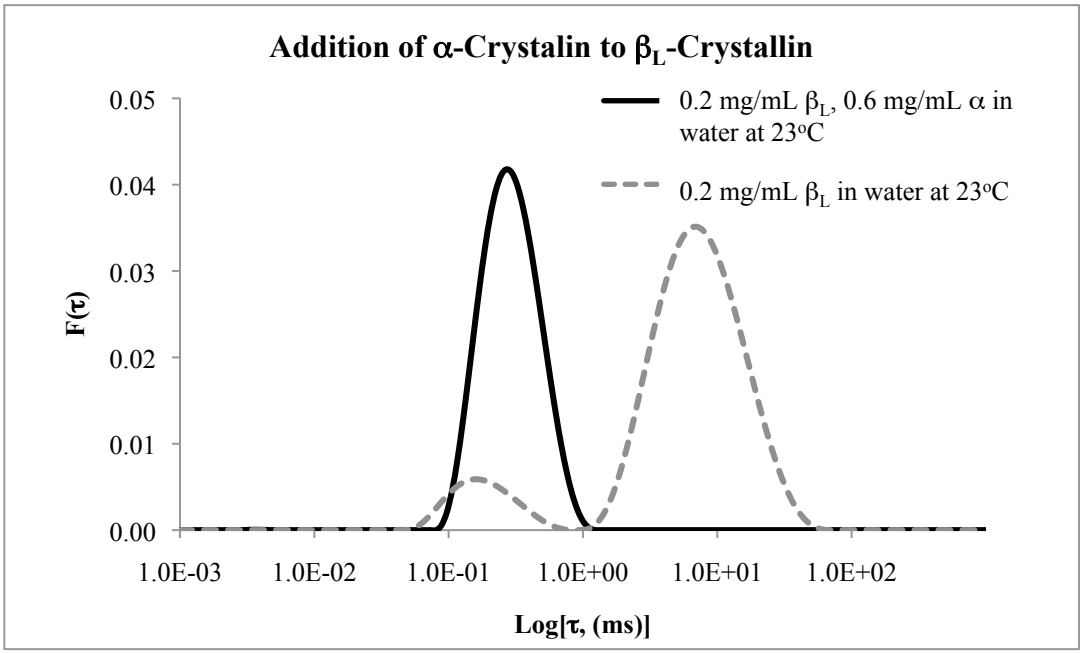


**Figure 2.21 A graph comparing 0.2 mg/mL $\beta_L$-crystallin and 0.2 mg/mL $\beta_L$-crystallin, 0.6 mg/mL α-crystallin in water at 23°C.**

A comparison of the average Γ versus $q^2$ plot and all of the Γ versus $q^2$ values indicates that the hydrodynamic values reported is accurate. Both graphs have very high $R^2$ values and there are no significant deviations from the trendline.

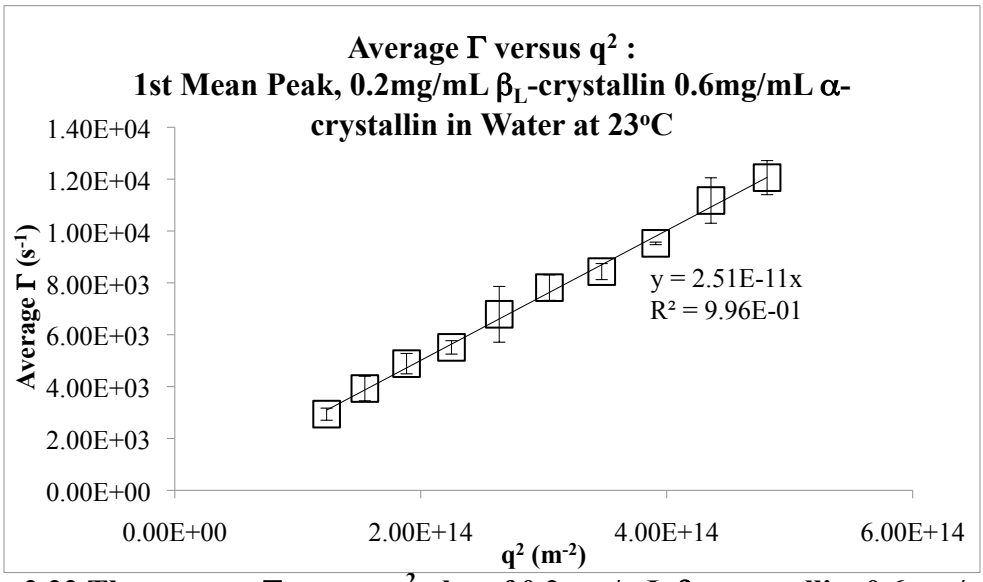


**Figure 2.22 The average Γ versus $q^2$ plot of 0.2 mg/mL $\beta_L$-crystallin, 0.6 mg/mL α-crystallin in water at 23°C.**

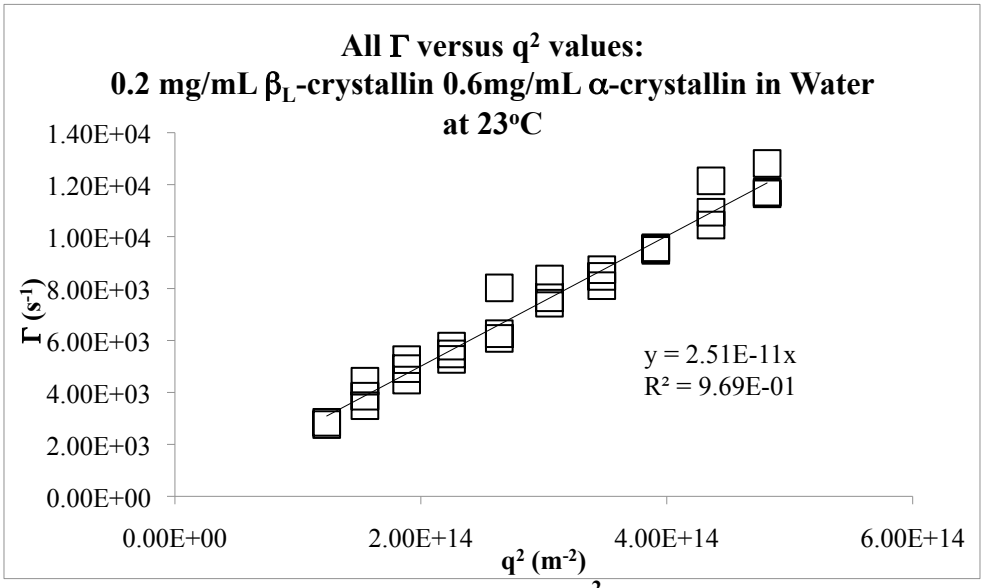


**Figure 2.23 A compilation of all of the Γ versus $q^2$ data collected for 0.2 mg/mL $\beta_L$-crystallin, 0.6 mg/mL α-crystallin in water at 23°C.**

Although it is established that α-crystallin is a chaperone, or more specifically a heat shock protein, this experiment served to uniquely demonstrate it as one.[10, 29, 34] The role of a heat shock protein is to prevent the formation of nonfunctional oligomeric structures, thereby suppressing aggregation.[35-38] Protein-protein interactions are dominated by intermolecular hydrogen bonds and electrostatic interactions.[45, 46] Therefore it is logical to infer that heat shock proteins interact with other proteins via these interactions.

### 2.3.3 Determination of Role of Electrostatics Using Salt

In an attempt to control the aggregation state of $\beta_L$-crystallin, sodium chloride was added to the system to mimic the electrostatic effect of α-crystallin. The biochemistry of a tear indicated that 120-165 mg/dl of $Na^+$ ions and 118-135 mg/dl of $Cl^-$ ions are naturally present in the environment of the crystallins. $Na^+$ and $Cl^-$ are the ions with the highest concentration in tears.[47] These facts led to the conclusion that sodium chloride was the ideal additive for understanding the role of electrostatics in the aggregation of the $\beta_L$-crystallin.

A sample of 0.2 mg/mL $\beta_L$-crystallin with 0.15M NaCl in water at 23$^o$C was prepared. There were no significant deviations in the normalized intensity correlation functions, other than what was expected, with respect to angle changes and time evolution.

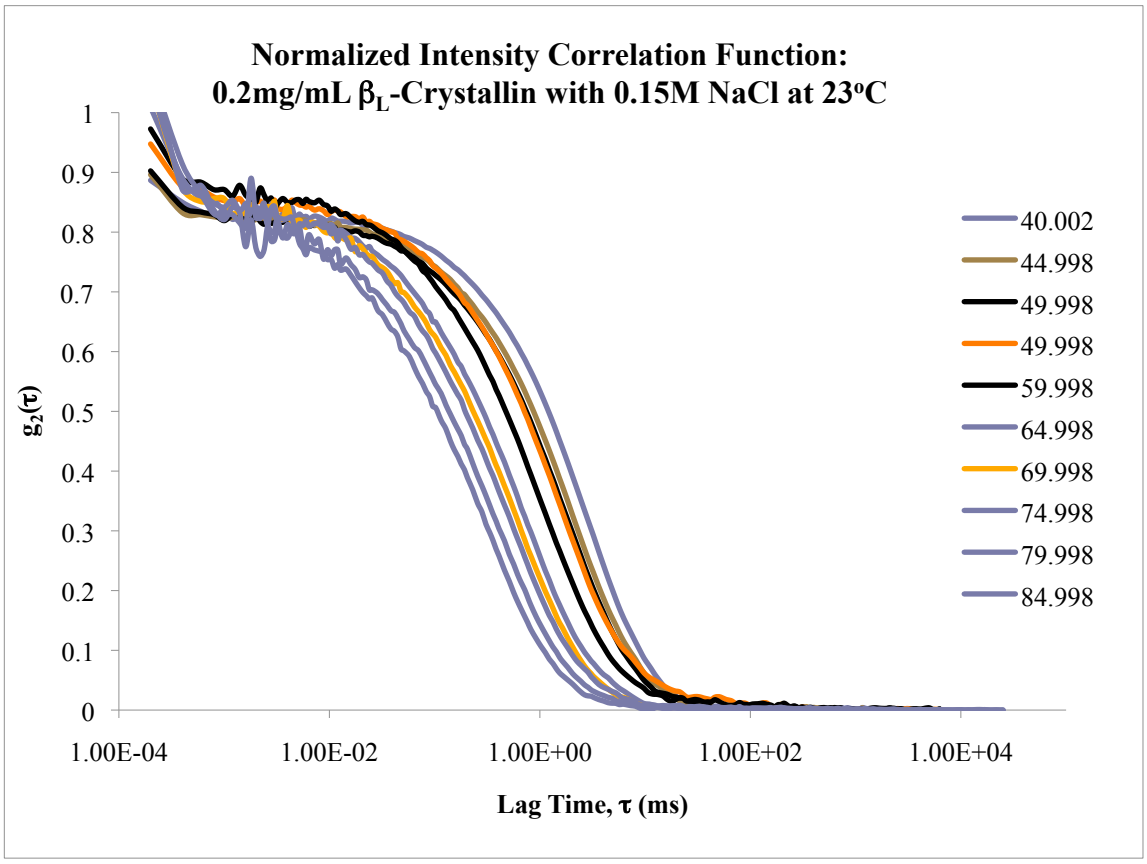


**Figure 2.24 The normalized intensity correlation function from one of the DLS runs performed on 0.2 mg/mL $\beta_L$-crystallin with 0.15M NaCl in water at 23°C**

DLS revealed two modes to be present in the probability distribution function with the addition of salt. There were also two modes present with no added salt in 0.2 mg/mL $\beta_L$-crystallin in water at 23°C.

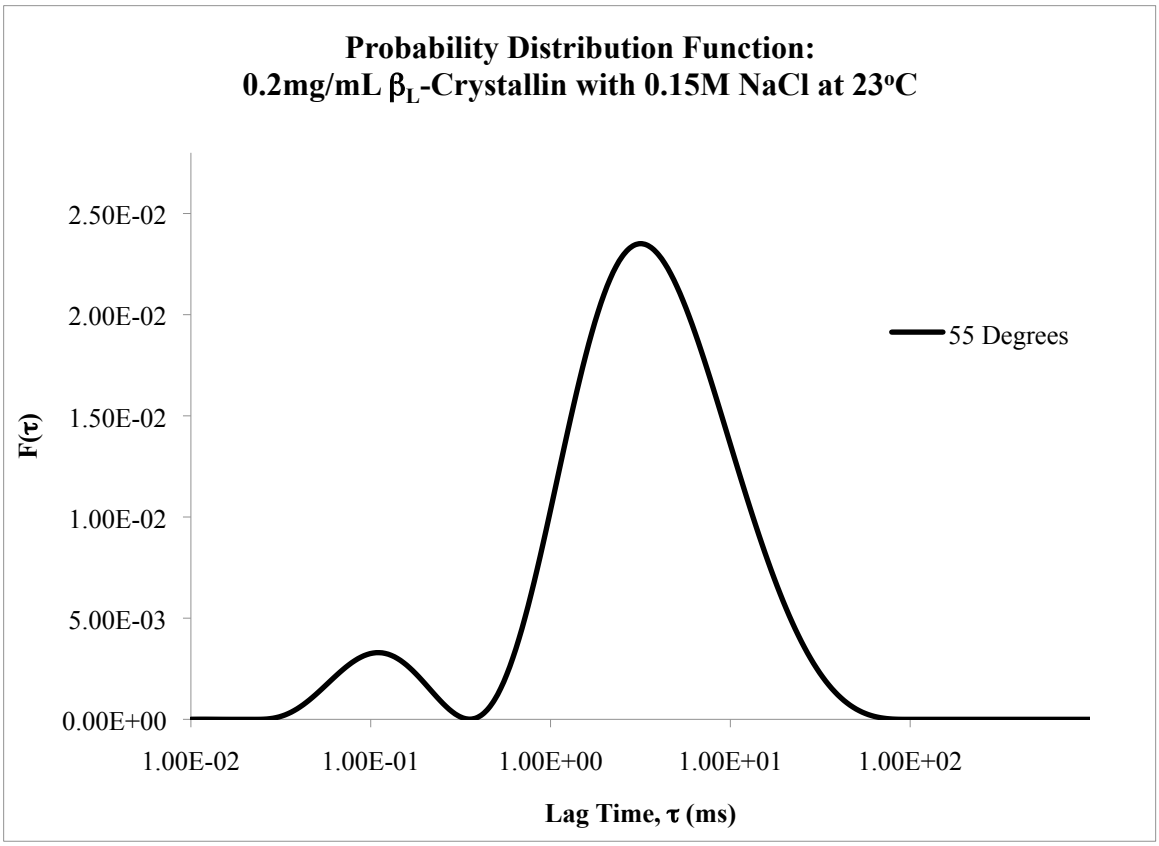


**Figure 2.25 A typical normalized intensity correlation function of 0.2 mg/mL $\beta_L$-crystallin with 0.15M NaCl in water at 23°C.**

The interesting point to note is that the addition of salt the reduced the aggregate $R_h$ from 250 nm to 120 nm. The addition of 0.15M NaCl successfully reduced the aggregate size and confirmed that electrostatics played a significant role in the aggregation of $\beta_L$-crystallin. It is important to note that charge-neutral interactions are still likely to be occurring in the system.

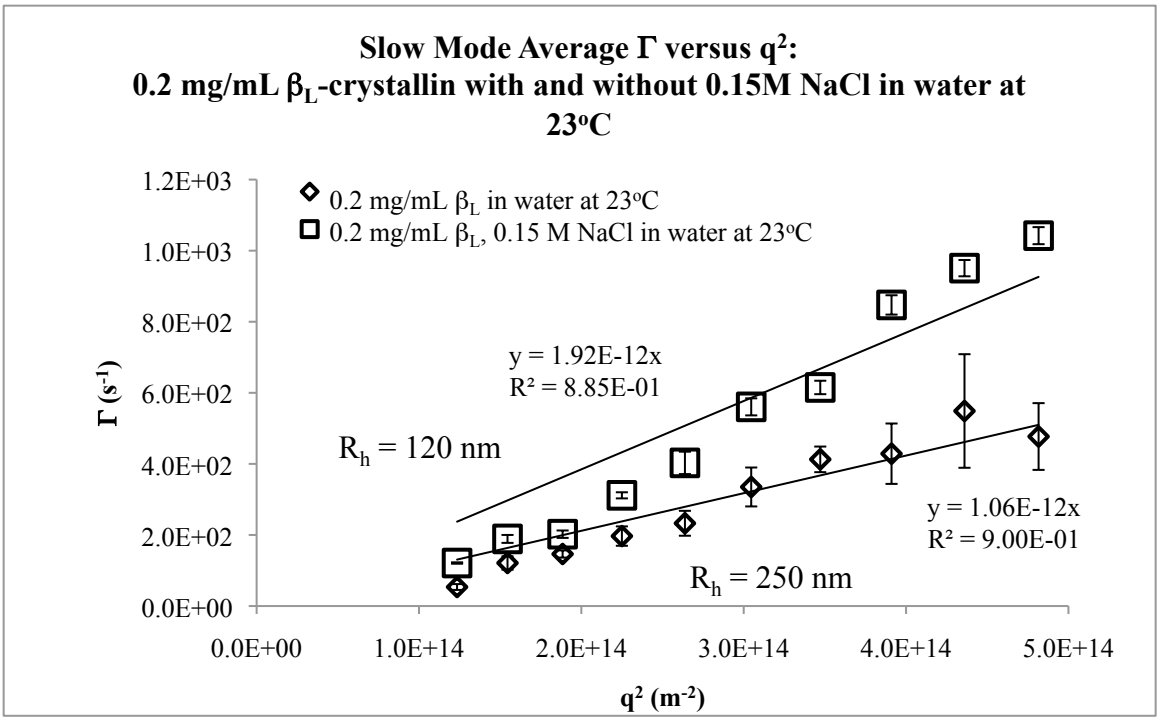


**Figure 2.26 A plot of the slow mode of 0.2 mg/mL $\beta_L$-crystallin in water at 23°C with and without 0.15 M NaCl.**

The validity of the 120 nm hydrodynamic radius is confirmed by comparing the average Γ versus $q^2$ to all of the data points collected. As can be seen in the two figures below, the $R^2$ values are close to one and the data is therefore very reliable.

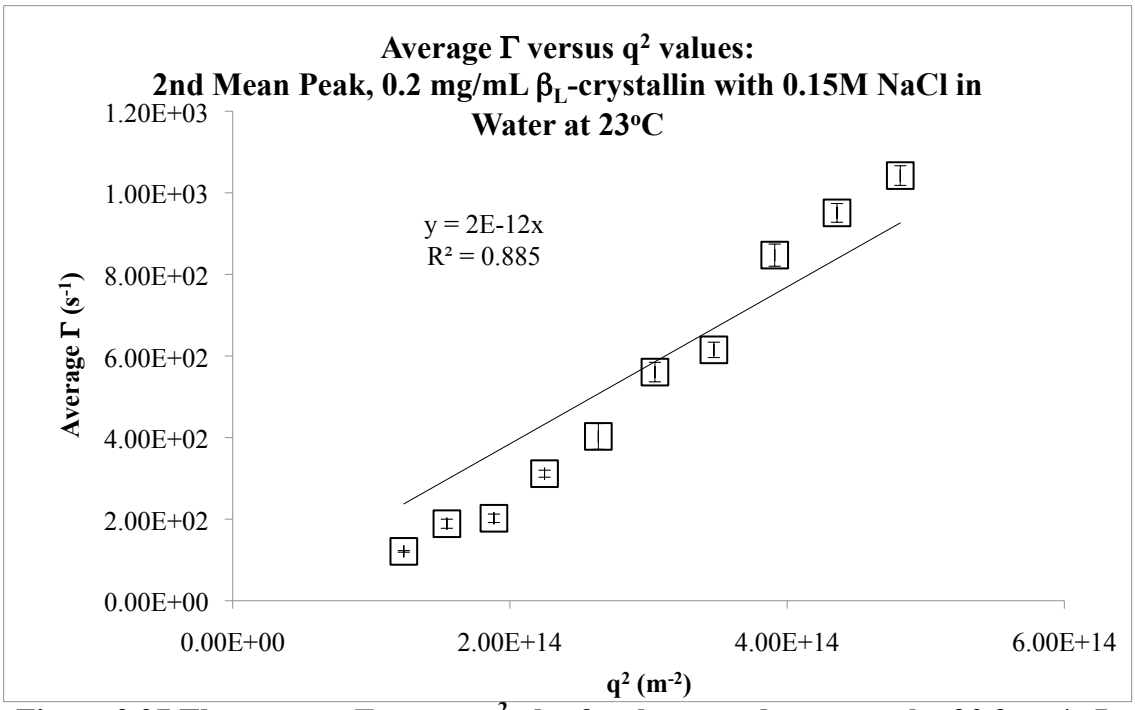


**Figure 2.27 The average Γ versus $q^2$ plot for the second mean peak of 0.2 mg/mL $\beta_L$-crystallin, 0.15 M NaCl in water at 23°C.**

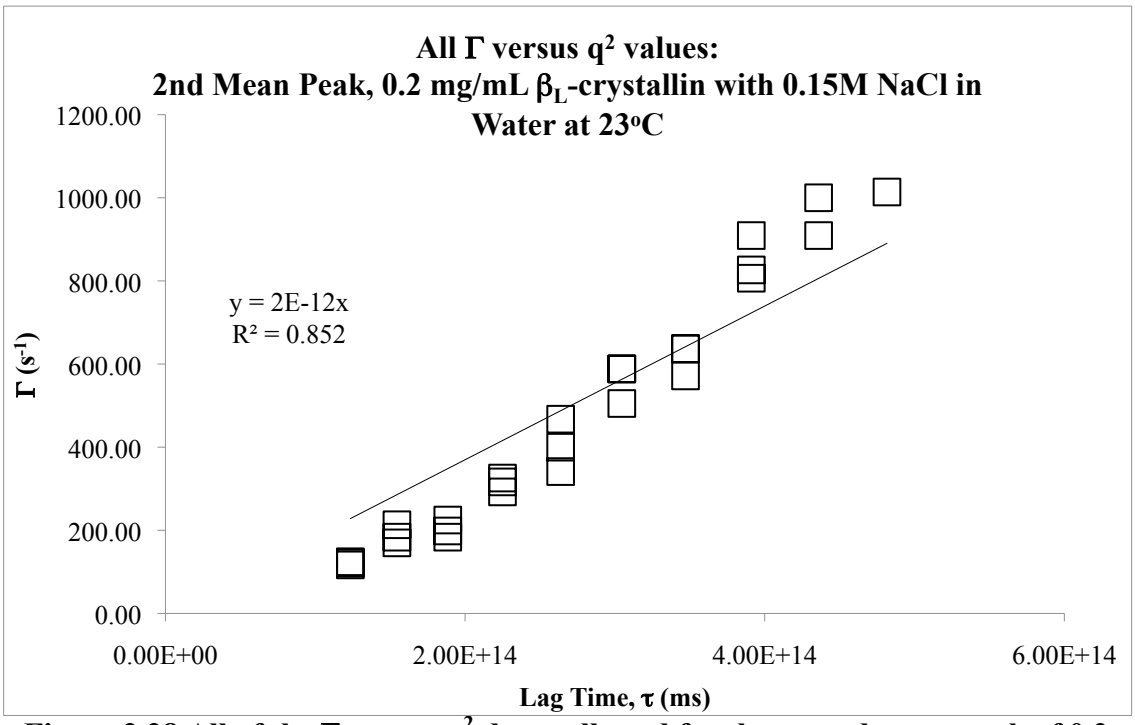


**Figure 2.28 All of the Γ versus $q^2$ data collected for the second mean peak of 0.2 mg/mL $\beta_L$-crystallin, 0.15 M NaCl in water at 23°C.**

The first mean peak present in the probability distribution function of 0.2 mg/mL $\beta_L$-crystallin, 0.15 M NaCl in water at 23°C represented a hydrodynamic radius of 5 nm. The accuracy of 5 nm is evaluated by comparing the average Γ versus $q^2$ data to all of the data points collected.

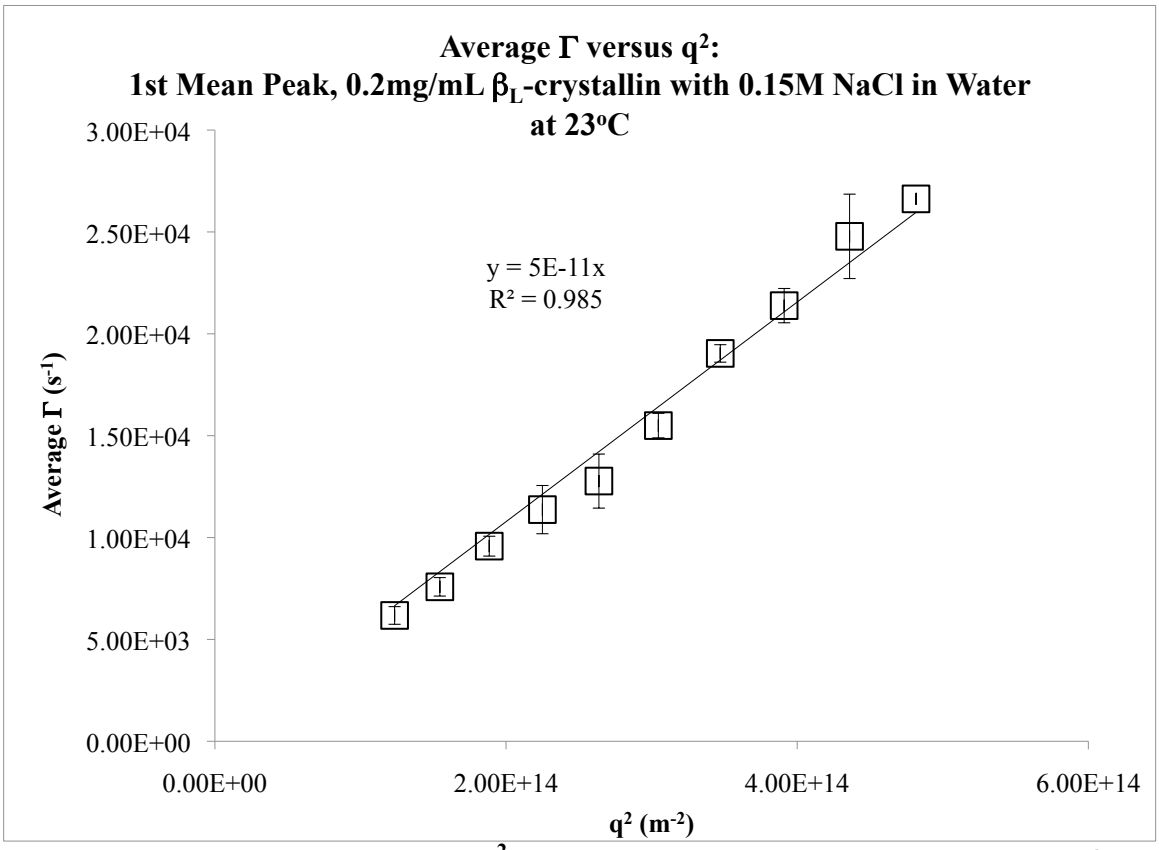


**Figure 2.29 The average Γ versus $q^2$ plot for the first mean peak of 0.2 mg/mL $\beta_L$-crystallin, 0.15 M NaCl in water at 23°C.**

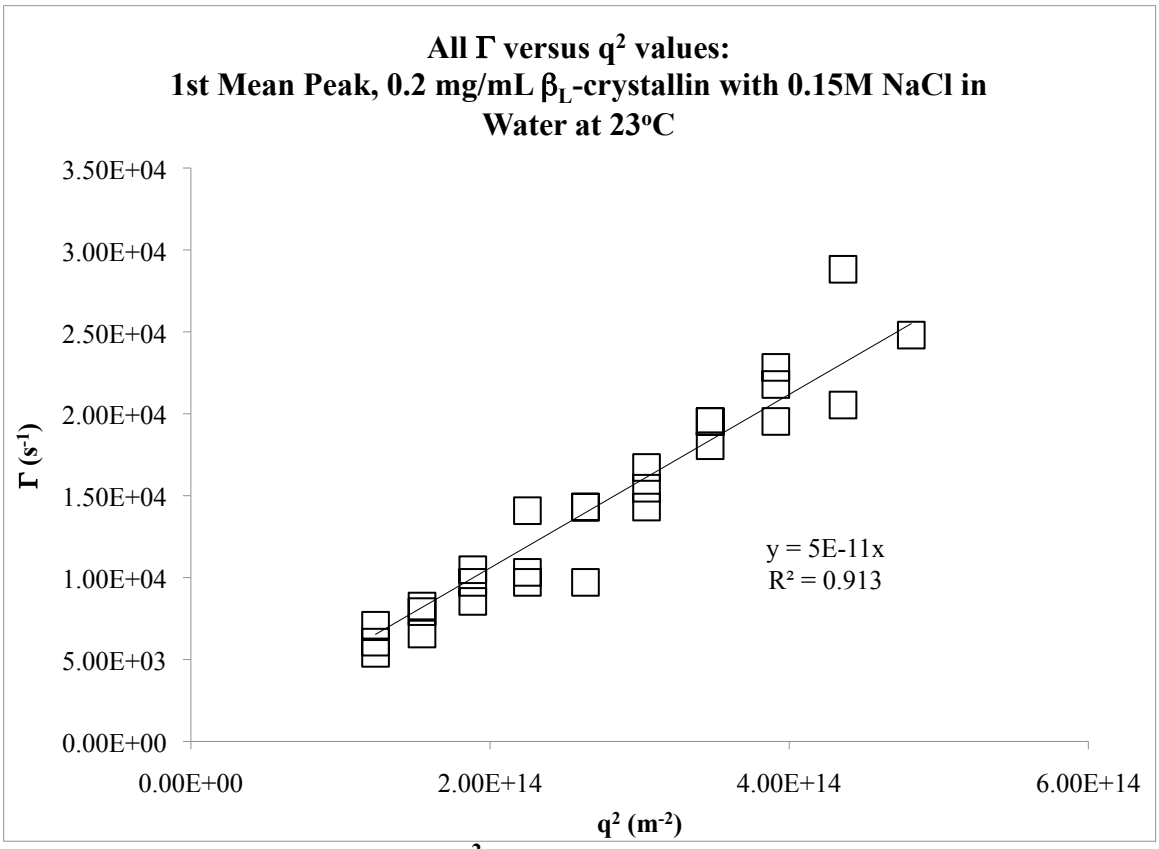


**Figure 2.30 All of the Γ versus $q^2$ data collected for the second mean peak of 0.2 mg/mL $\beta_L$-crystallin, 0.15 M NaCl in water at 23°C.**

The $R^2$ values of both of the previous figures are close to one. The hydrodynamic radius of the first mean peak is confirmed to be 5 nm for 0.2 mg/mL $\beta_L$-crystallin, 0.15 M NaCl in water at 23°C.

## 2.4 Analysis in Biological Conditions

### 2.4.1 Evaluation of Equilibrium $R_h$ Values

The next step in this project was to perform the previous experiments again, but in conditions similar to the lens. A 20mM $Na_2HPO_4$, 20mM $NaH_2PO_4$, 100mM NaCl, 3mM $NaN_3$, 1mM EDTA, phosphate buffered saline (PBS) with a pH of 6.9 served to mimic

the pH and the ionic conductivity, 190 mM, of the lens.[41] The kinetics of α-crystallin and $\beta_L$-crystallin were investigated in PBS at 35°C.

The normalized intensity correlation functions of 0.2 mg/mL α-crystallin in PBS at 35°C were indicative of a single size-scale. The curves were smooth and reproducible irrelevant to the time between data collection at the different angles over three runs.

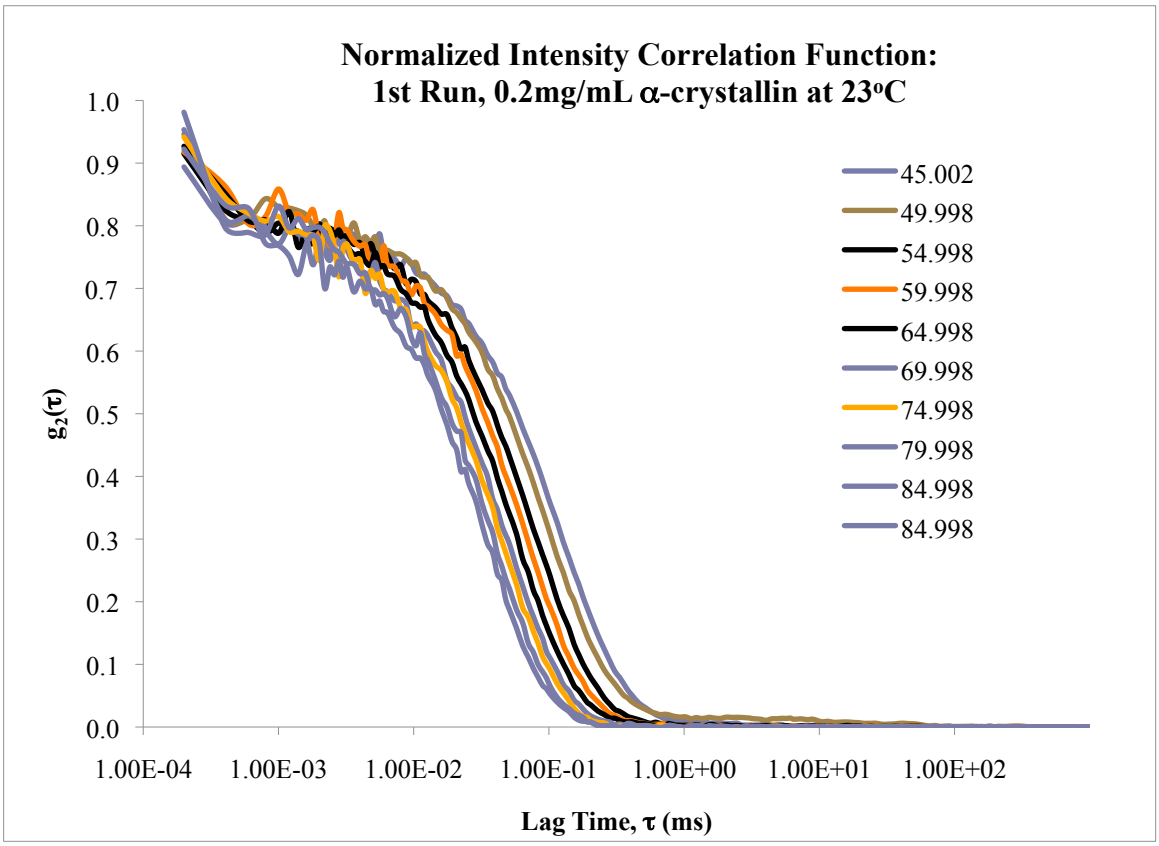


**Figure 2.31 A normalized intensity correlation function of 0.2 mg/mL α-crystallin in PBS at 35°C. This data is from run one of three runs done on a sample that had a $t_{total}$ time of one month.**

0.2 mg/mL α-crystallin in PBS at 35°C demonstrated only one mode in the probability distribution function corresponding to a size-scale of 10.0 nm. The value of 10 nm was comparable to the established hydrodynamic radius in the water solution. This indicates that biological conditions did not have a significant effect on α-crystallin at this concentration.

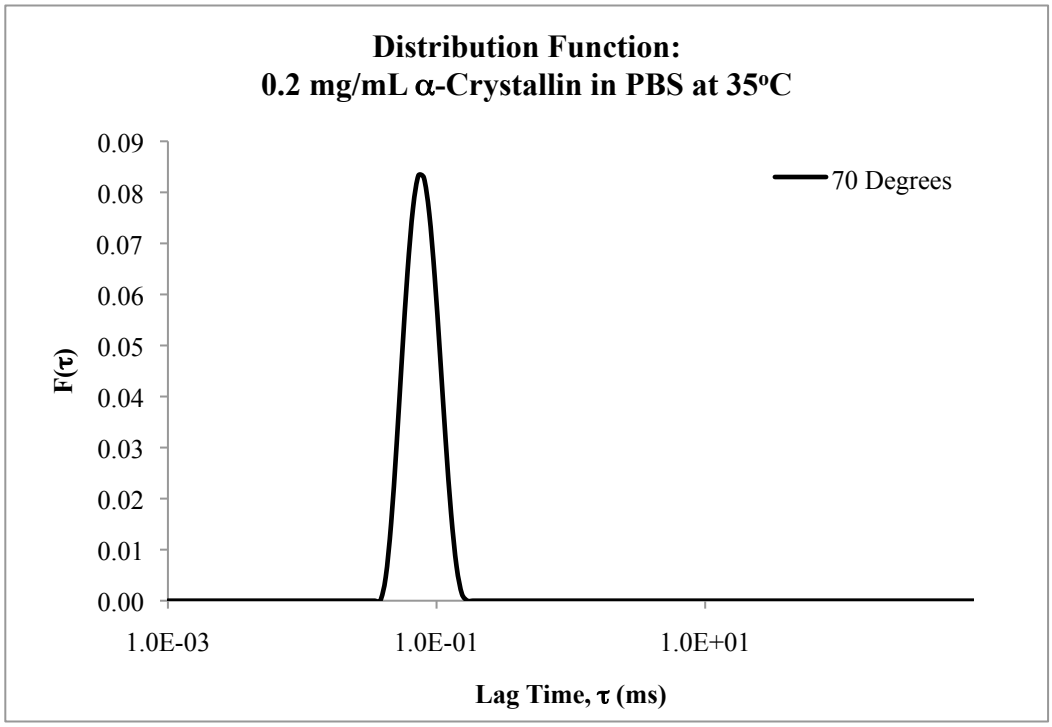


**Figure 2.32 A probability distribution function of 0.2 mg/mL α-crystallin in PBS at 35°C.**

In order to verify the accuracy of the conclusions, the data from all three runs at each time the data was collected, was graphed in two ways. The data from all three runs per $t_{total}$ value was graphed on one Γ versus $q^2$ plot and the second graph used average Γ from all three runs. By comparing the distribution of data with these two methods any kinetic evolution on the time-scale of the three runs would be visible. (Kinetic changes on a

greater time-scale are analyzed through the $t_{total}$ variable.) It was clear that no shift occurred in the data over time. This method also draws attention to erroneous data points that could be skewing the final conclusions.

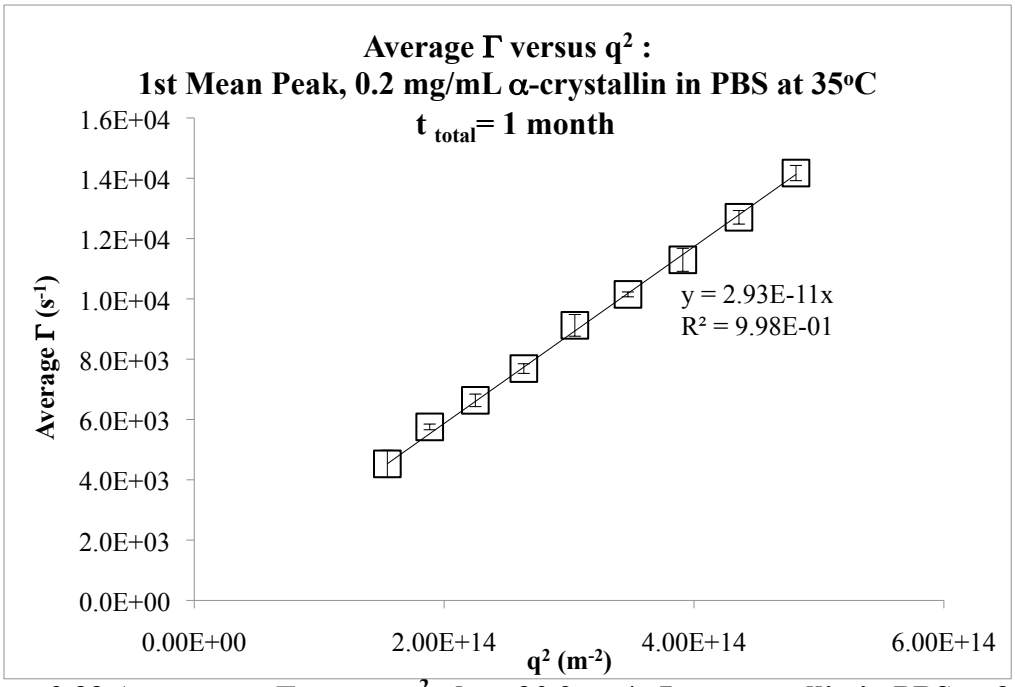


**Figure 2.33 An average Γ versus $q^2$ plot of 0.2 mg/mL α-crystallin in PBS at 35°C with a $t_{total}$ time of one month.**

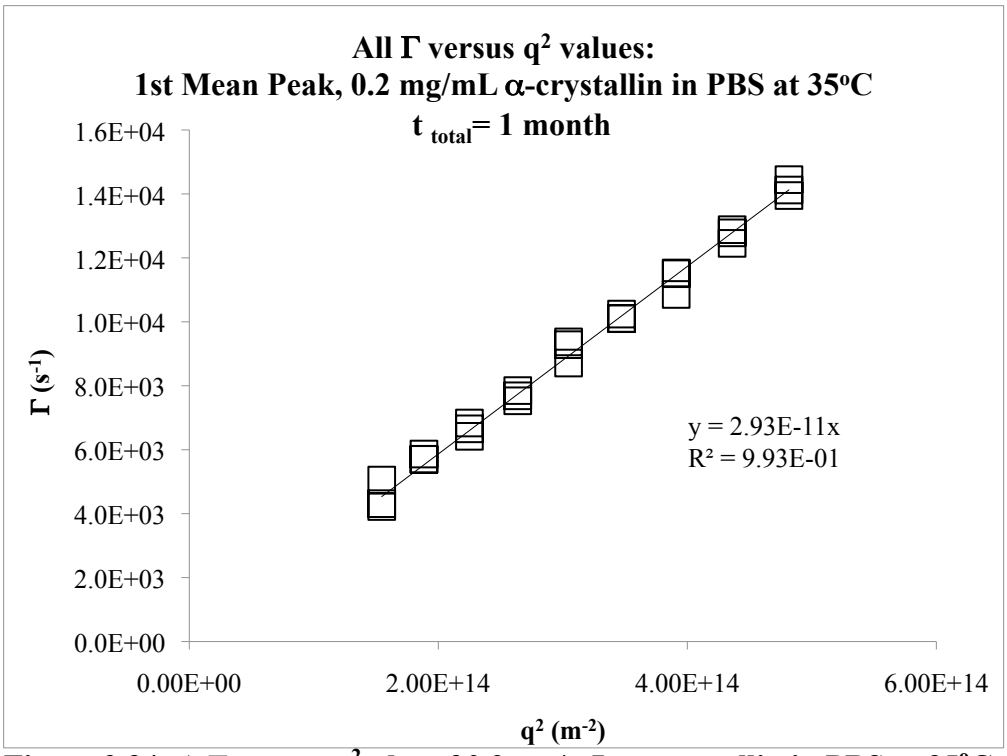


**Figure 2.34: A Γ versus $q^2$ plot of 0.2 mg/mL α-crystallin in PBS at 35°C.**

It is clear by comparing the two methods, illustrated in the previous two plots, that the data collected is reliable. The close clustering of data points in the second graph reveals that the data is accurate and reproducible. The graph with the average values has low error bars and an excellent fit, which also confirms the reliability of the data.

It was also important to establish that the complication of biological conditions did not have any effect on the hydrodynamic radius [10] over a time-scale longer than the 30 minutes it took to collect data from three runs. In order to verify that the $R_h$ was not changing the $t_{total}$ variable was utilized. The $R_h$ value of 10 nm was established to be independent of time.

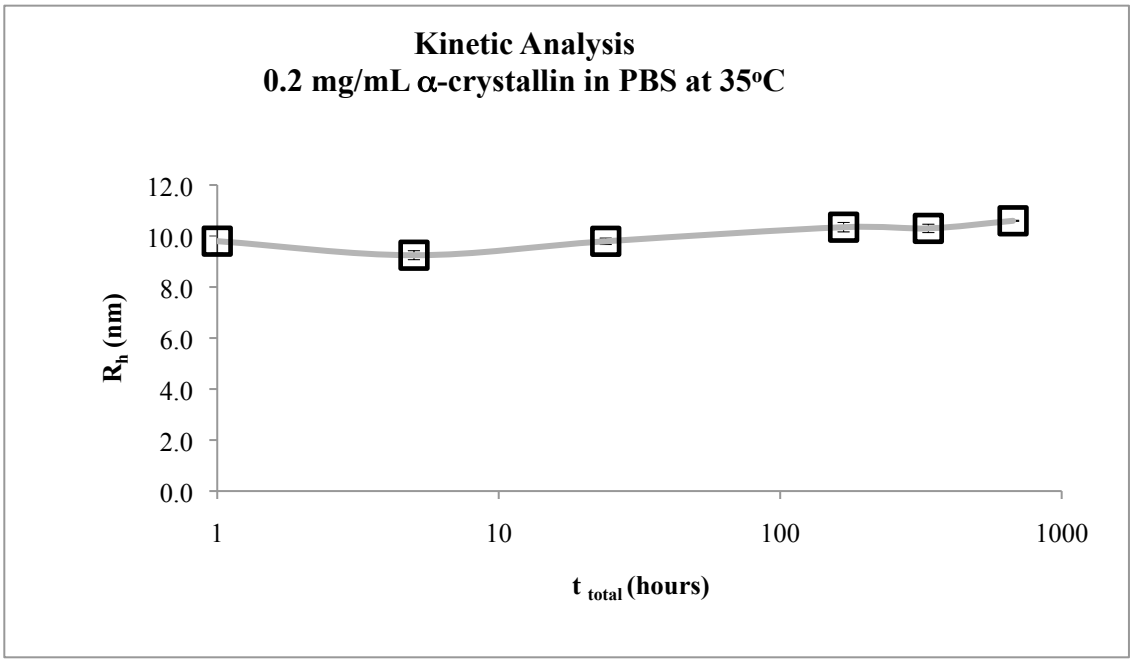


**Figure 2.35: The $R_h$ of 0.2 mg/mL α-crystallin in PBS at 35°C is demonstrated have an equilibrium value of 10.0 nm, independent of the time-scale of these experiments.**

In contrast to α-crystallin's single mode, 0.2 mg/mL $\beta_L$-crystallin in PBS at 35°C exhibited a normalized intensity function indicative of multiple size-scales.

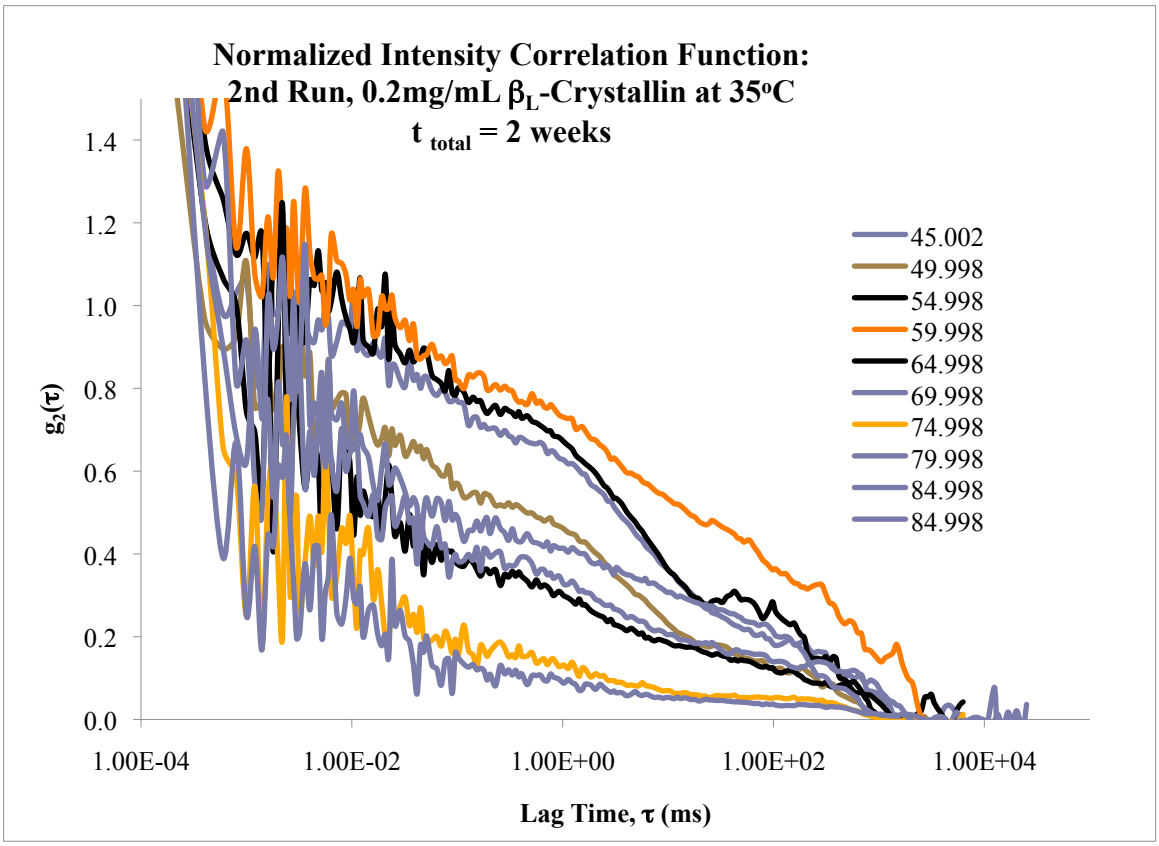


**Figure 2.36 The normalized intensity correlation function of 0.2 mg/mL $\beta_L$-crystallin in PBS at 35°C with a $t_{total}$ value of 2 weeks.**

The probability distribution function revealed multi-modal properties at all $t_{total}$ values. Only two of the peaks were within the reliable range of DLS analysis. Therefore only the first two peaks could be evaluated.

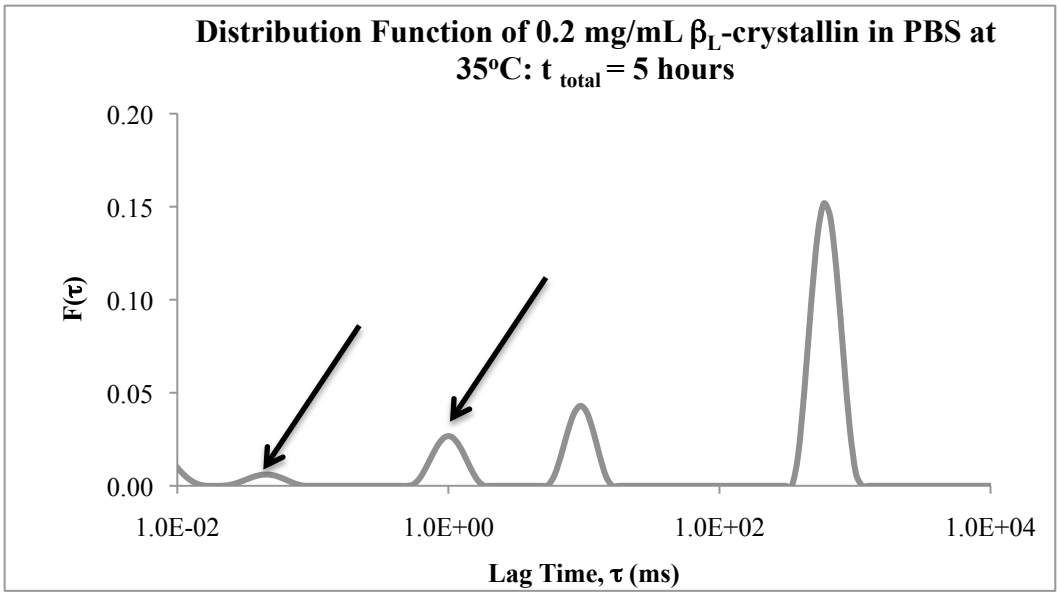


**Figure 2.37 A probability distribution function of 0.2 mg/mL $\beta_L$-crystallin in PBS at 35°C. The two peaks within the reportable range of DLS are highlighted with an arrow.**

Based on the relative weights of the peaks in the probability distribution function of 0.2 mg/mL $\beta_L$-crystallin in PBS at 35°C, the aggregates were more prevalent in the solution than the isolated $\beta_L$-crystallin. The integral of each peak divided by the integral of the curve provided the relative weight of the peak. The relative weight of the peak directly relates to the amount of polymers of that size-scale present in solution.

The $\Gamma$ versus $q^2$ data for the first and second peaks in the probability distribution functions of 0.2 mg/mL $\beta_L$-crystallin in PBS at 35°C were plotted and so were the average $\Gamma$ values for the three runs at each q value. The data collected from the first peak, which corresponds to the smaller size-scale, is below.

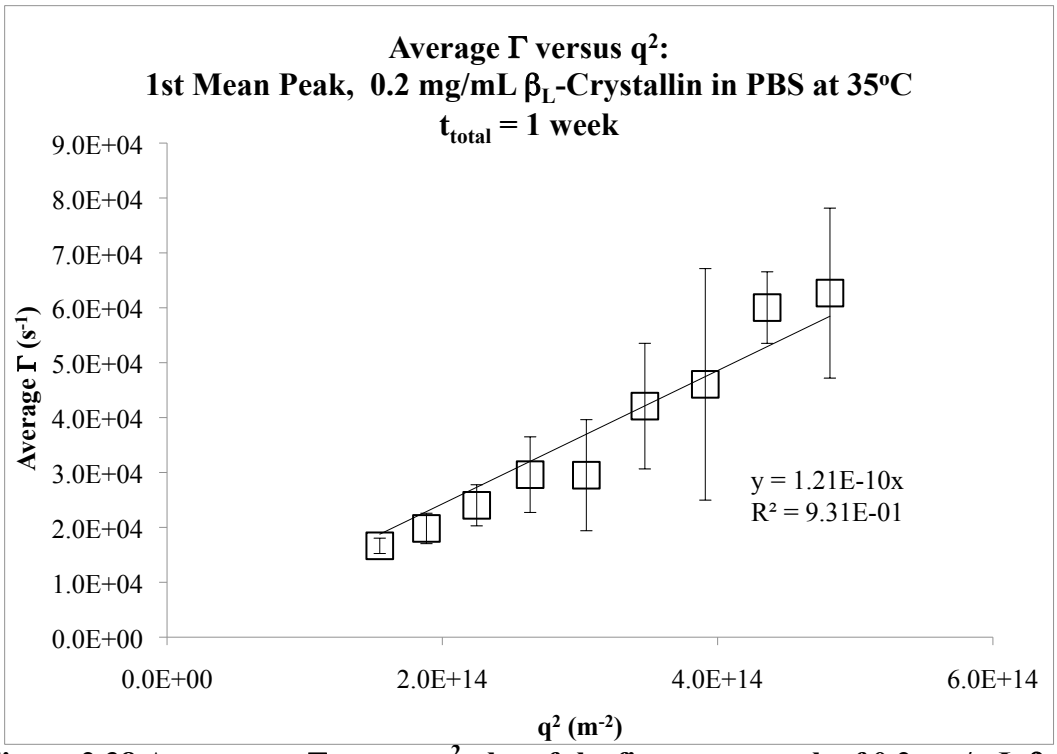


**Figure 2.38 An average Γ versus $q^2$ plot of the first mean peak of 0.2 mg/mL $\beta_L$-crystallin in PBS at 35°C.**

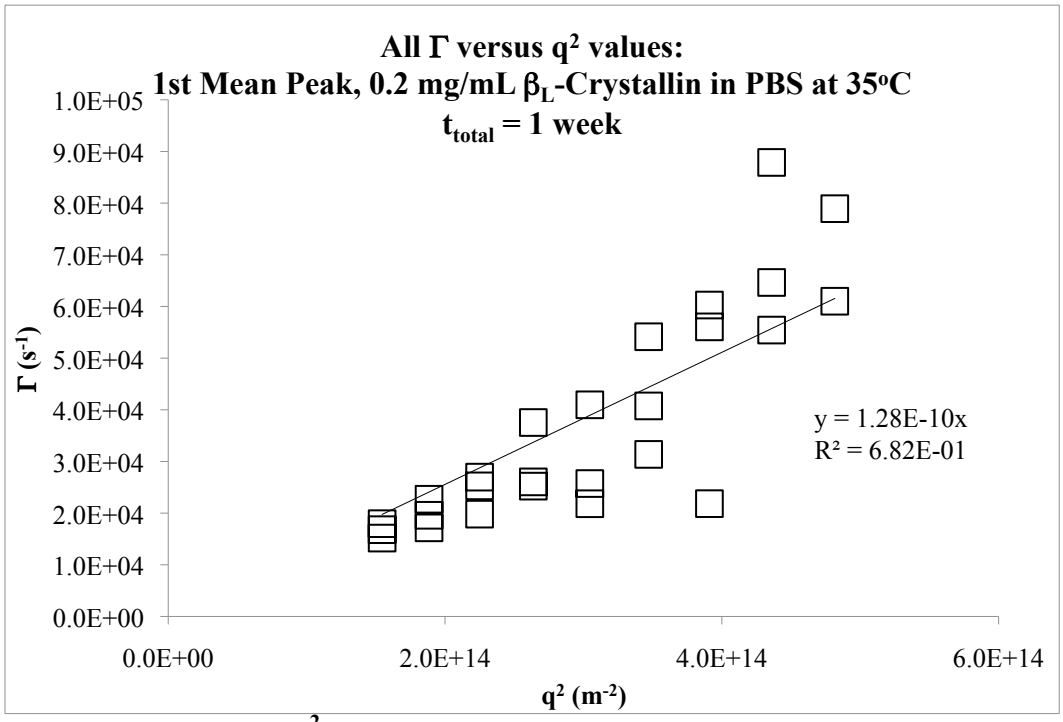


**Figure 2.39 A Γ versus $q^2$ plot of all of the data collected on the first mean peak of 0.2 mg/mL $\beta_L$-crystallin in PBS at 35°C.**

The error bars on the average Γ versus $q^2$ plot of the first mean peak are larger than those associated with the smallest size-scale that appeared in the water solvent system of $\beta_L$-crystallin. The two fundamental differences between these two systems are the solvent and temperature. The plot of all of the data confirms that there is a subtle variance in the data collected. Based on the data distribution in these two plots it appears the change in conditions increased the instability of the $\beta_L$-crystallin fast mode. The average and all Γ versus $q^2$ graphs of the second mean peak demonstrate an even greater aggregate instability.

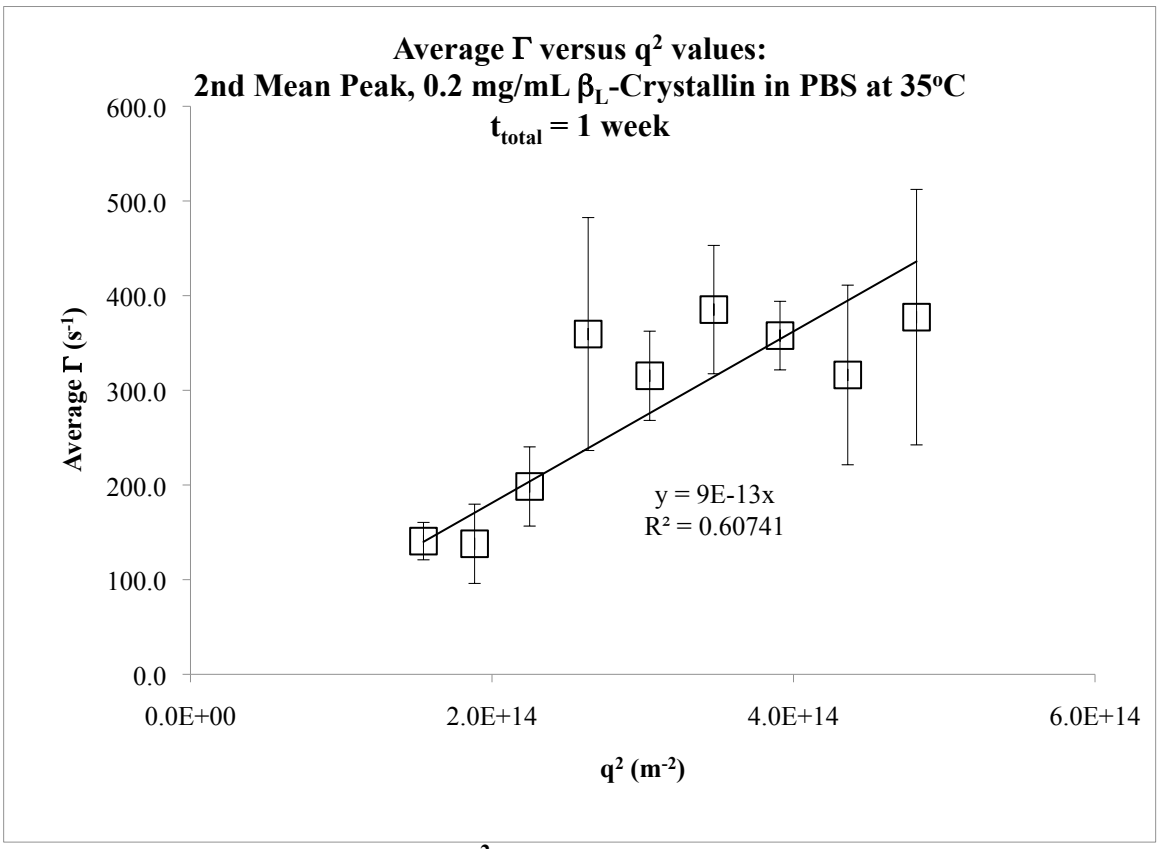


**Figure 2.40 An average Γ versus $q^2$ plot of the second mean peak of 0.2 mg/mL $\beta_L$-crystallin in PBS at 35°C.**

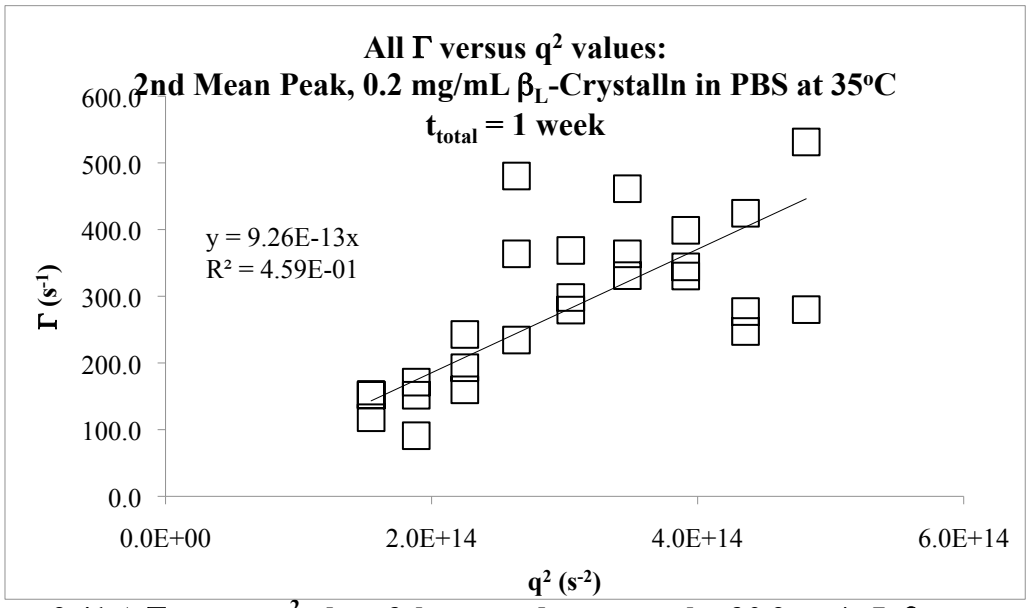


**Figure 2.41 A Γ versus $q^2$ plot of the second mean peak of 0.2 mg/mL $\beta_L$-crystallin in PBS at 35°C.**

When the $R_h$ values of 0.2 mg/mL $\beta_L$-crystallin in PBS at 35°C were plotted against $t_{total}$, the fast mode was established to be independent of time. The individual $\beta_L$-crystallin was demonstrated to have an average $R_h$ of 3.0 nm.

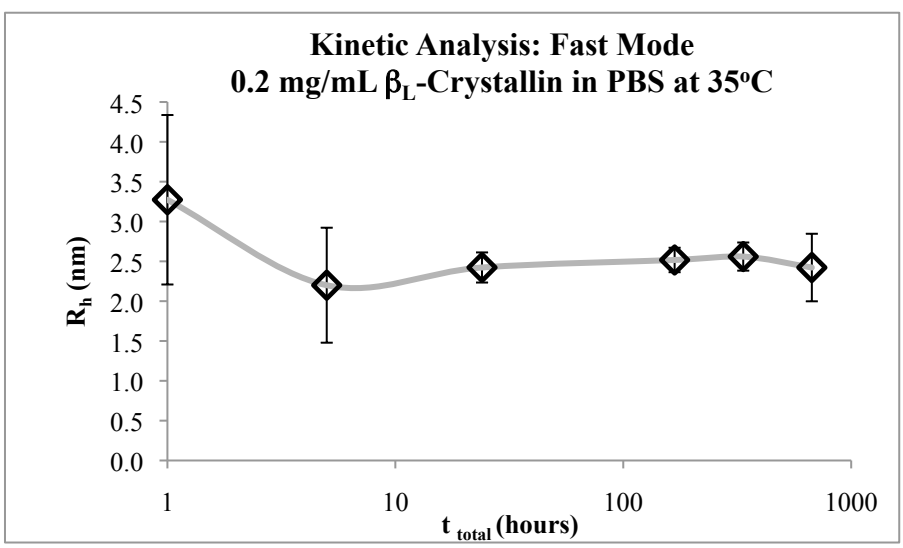


**Figure 2.42 A plot that established the kinetic independence of the fast mode of 0.2 mg/mL $\beta_L$-crystallin in PBS at 35°C.**

Analysis of the second peak revealed a high error associated with the $R_h$ values due to the fact that the size-scales were at the limit of the range of DLS. The approximate average $R_h$ of the aggregate was 300 nm.

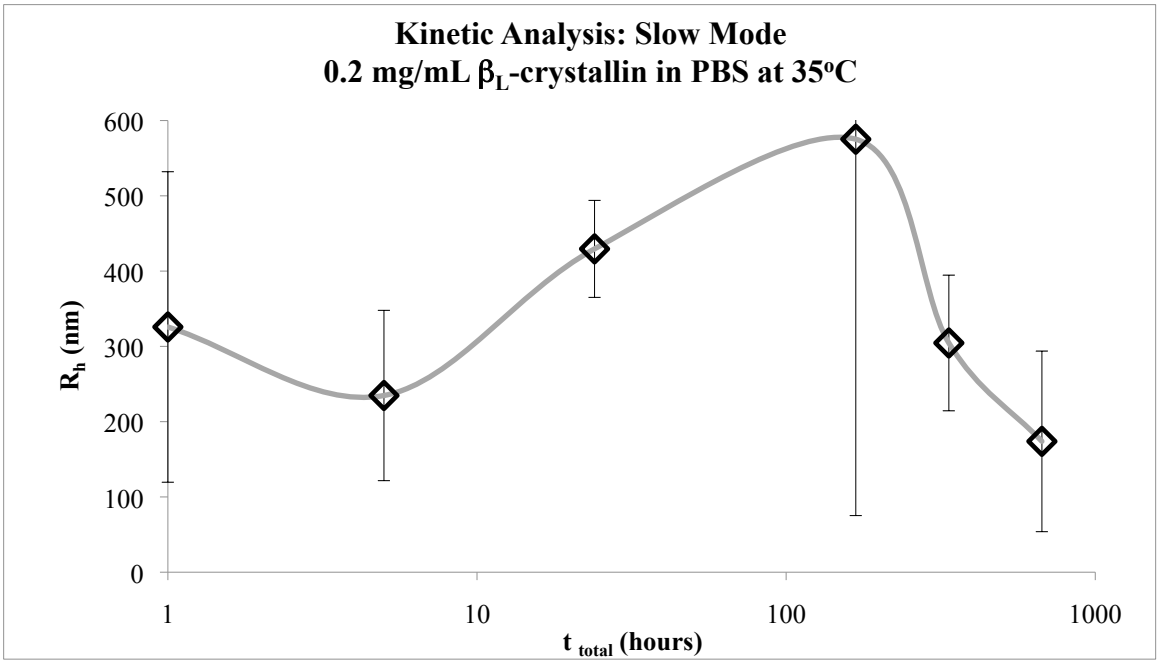


**Figure 2.43 A graph of the slow mode of 0.2 mg/mL $\beta_L$-crystallin in PBS at 35°C.**

The other peaks visible in the probability distribution functions were beyond the range of DLS analysis. The final conclusion from the kinetic analysis was that both α-crystallin and $\beta_L$-crystallin were kinetically independent on the time-scale that data was collected.

In order to understand more about the internal packing of the aggregate structure formed by $\beta_L$-crystallin in PBS, the SLS data, which was collected simultaneously with the DLS data, was analyzed. The first step in this analysis was to partition the scattered intensity

according to the different size-scales present in solution. This was essentially done by taking the integral of the individual mean peaks and dividing it by the probability distribution function integral. The mathematical details are reviewed in the static light scattering theory section.

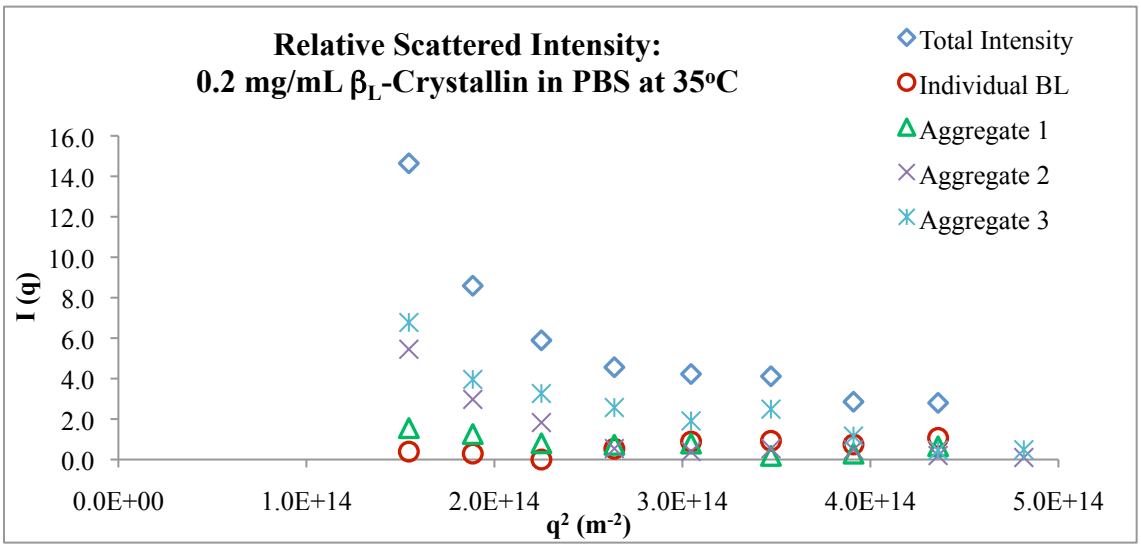


**Figure 2.44 The relative scattered intensity of 0.2 mg/mL $\beta_L$-crystallin in PBS at 35oC determined using static light scattering data.**

The aggregate referred to as "aggregate 1" in the relative scattered intensity plot is the second mean peak analyzed in the previous section. The size-scale of this peak was previously asserted to be 300 nm, which is at the edge of the range of DLS. Because this aggregate is at the upper limit of DLS, it was the only aggregate on which a fractal dimension analysis could be performed. The $d_f$ of the 300 nm aggregate was determined to be 4.4 when $\beta_L$-crystallin was in PBS. This suggested a loose structure. These results were comparable to the aggregate in water at 23$^o$C.

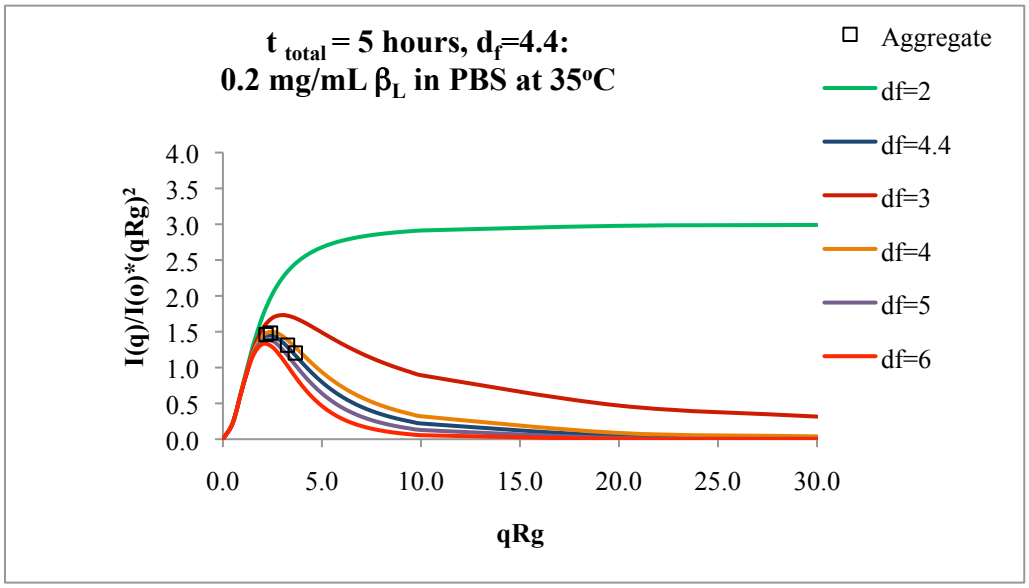


**Figure 2.45 A Kratky plot of 0.2 mg/mL $\beta_L$-crystallin in phosphate buffered saline (PBS) at 35°C and $t_{total}$ = 5 hours. A fractal dimension of 4.4 was the most accurate fit. This $d_f$ value was verified at other $t_{total}$ values as well.**

### 2.4.2 Interaction Between Proteins

When α-crystallin was added to $\beta_L$-crystallin, unlike in the water solution, all of the aggregates did not disappear. The normalized intensity correlation functions were considerably smoother than those produced by 0.2 mg/mL $\beta_L$-crystallin in PBS at 35°C. A smooth drop from 1.0 to 0.0 on the vertical axis on the normalized intensity correlation function is indicative of a predominance of smaller size-scales.

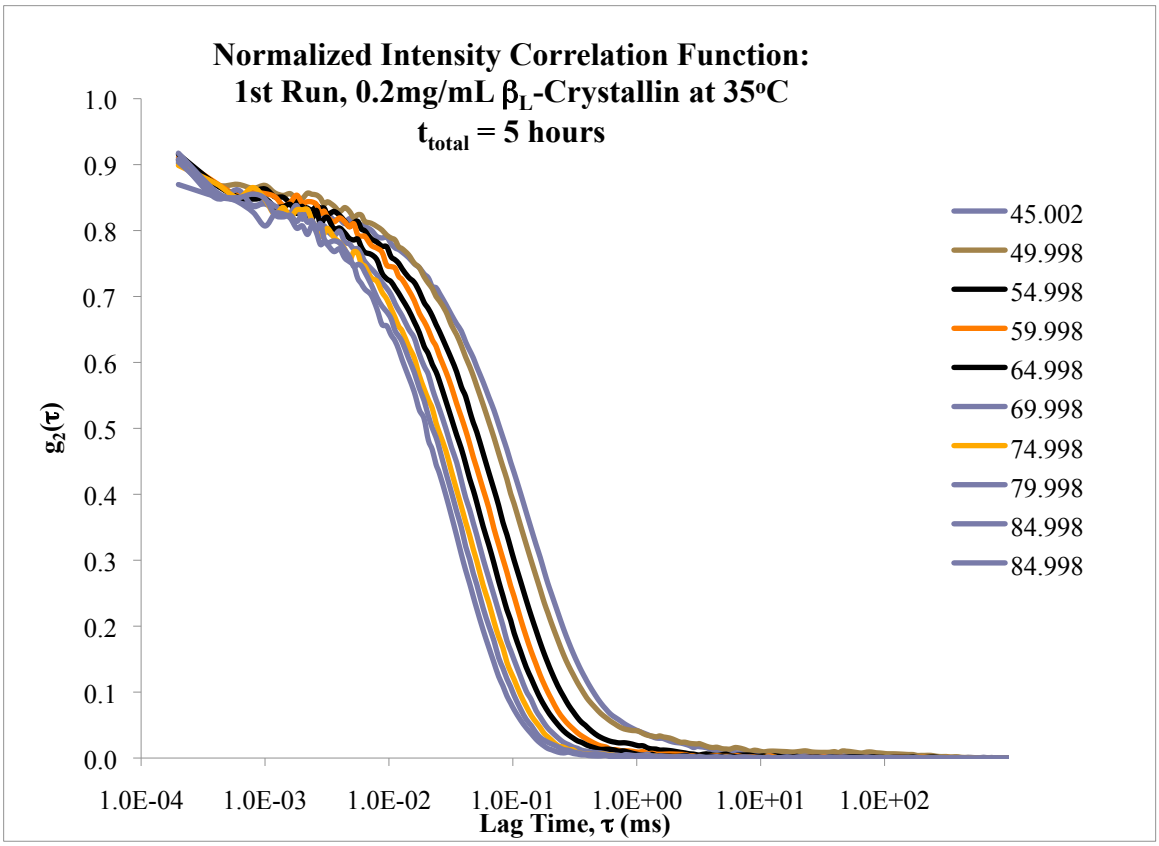


**Figure 2.46 The normalized intensity correlation functions of 0.2 mg/mL $\beta_L$-crystallin, 0.6 mg/mL α-crystallin in PBS at 35°C.**

The relative amount of aggregate was reduced upon the addition of 0.6 mg/mL $\beta_L$-crystallin to 0.2 mg/mL α-crystallin in PBS at 35°C. This effect was visible by comparing the probability distribution functions of 0.2 mg/mL $\beta_L$-crystallin in PBS at 35°C and 0.2 mg/mL $\beta_L$-crystallin, 0.6 mg/mL α-crystallin in PBS at 35°C. The addition of α-crystallin reduced the prevalence of aggregates.

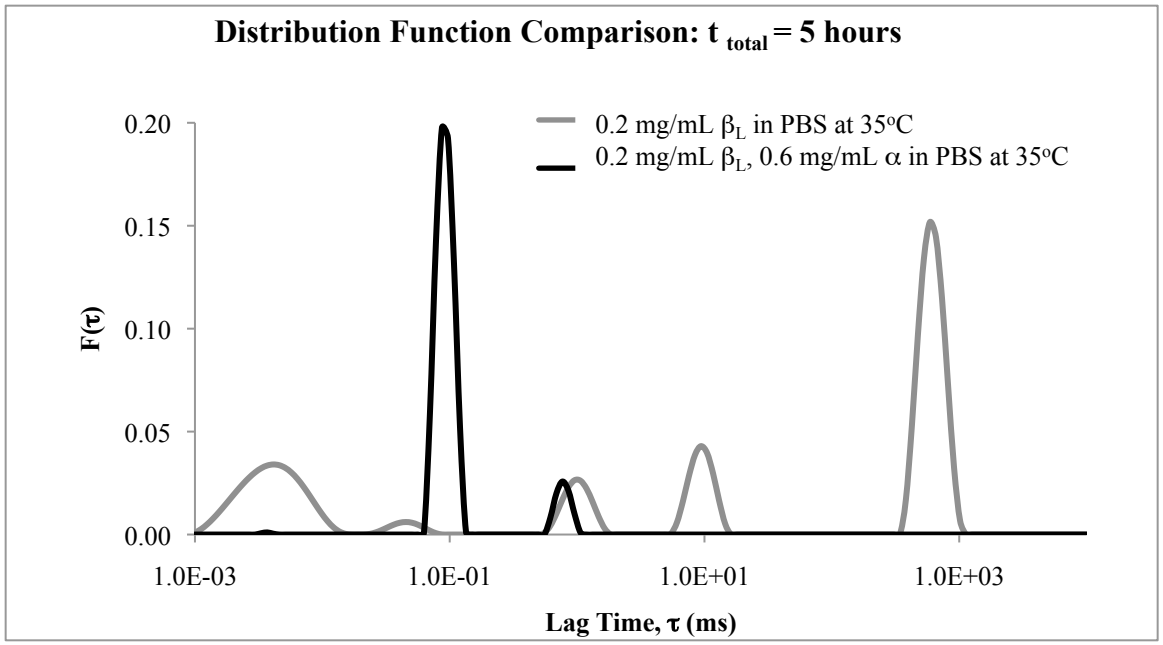


**Figure 2.47 A comparison of the probability distribution functions of 0.2 mg/mL $\beta_L$-crystallin in PBS at 35°C and 0.2 mg/mL $\beta_L$-crystallin, 0.6 mg/mL $\alpha$-crystallin in PBS at 35°C. The addition of $\alpha$-crystallin reduces the prevalence of aggregates.**

A comparison of the average $\Gamma$ versus $q^2$ plot and all of the $\Gamma$ versus $q^2$ data of the first and second peak indicated the stability of the size-scales corresponding to the first and second mean peak. The first mean peak was associated with low error in the average $\Gamma$ versus $q^2$ plot. The low error verifies the accuracy of the size-scale of 10.5 nm. The plot of all of the $\Gamma$ versus $q^2$ data on the first peak confirms this conclusion due to its minor distribution.

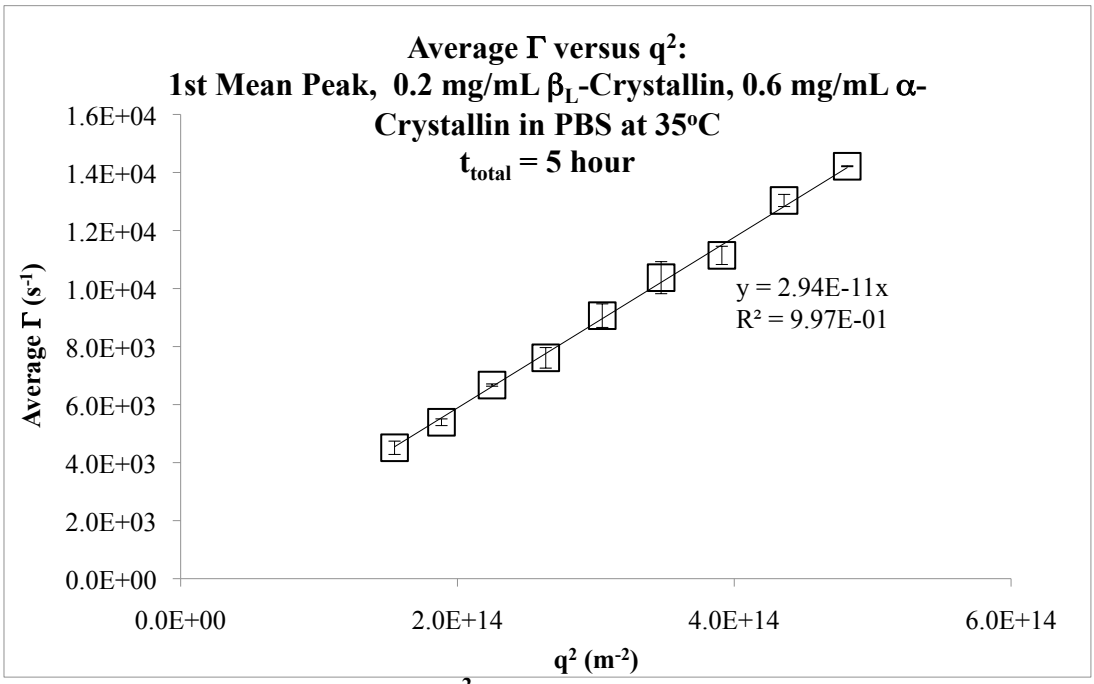


**Figure 2.48 The average Γ versus $q^2$ plot of 0.2 mg/mL $\beta_L$-crystallin, 0.6 mg/mL α-crystallin in PBS at 35°C.**

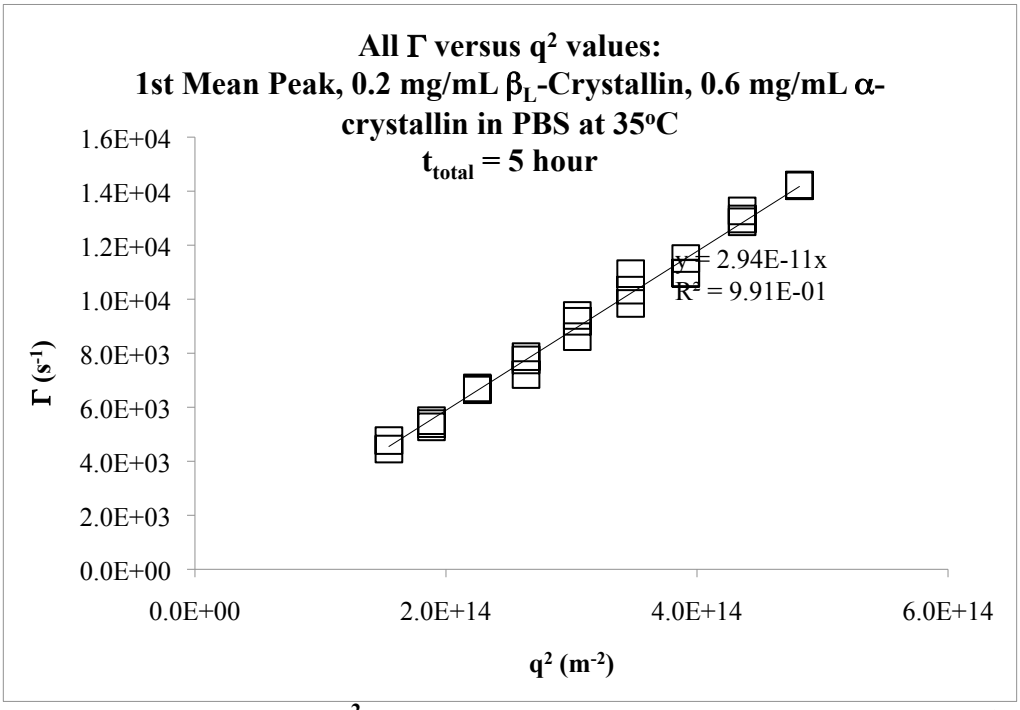


**Figure 2.49 The Γ versus $q^2$ plot of all of the data collected on 0.2 mg/mL $\beta_L$-crystallin, 0.6 mg/mL α-crystallin in PBS at 35°C.**

The kinetic stability of the fast mode of 0.2 mg/mL $\beta_L$-crystallin, 0.6 mg/mL $\alpha$-crystallin in PBS at 35°C was evaluated by plotting the $R_h$ versus $t_{total}$. The $R_h$ was determined to be independent of the time-scale on which data was collected.

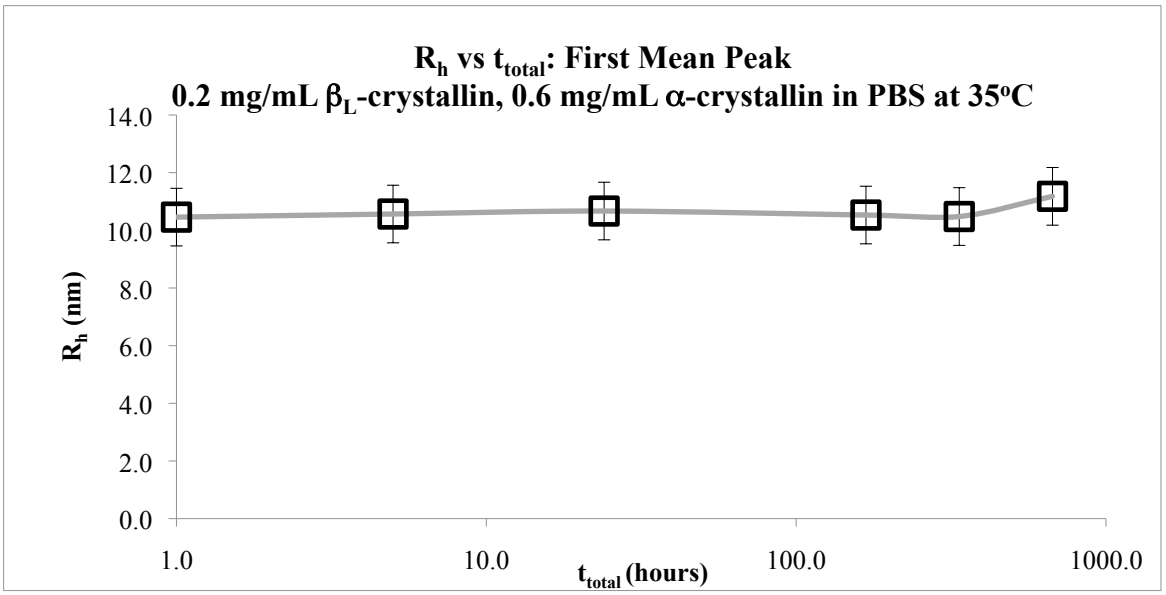


**Figure 2.50 A graph of $R_h$ versus $t_{total}$ of 0.2 mg/mL $\beta_L$-crystallin, 0.6 mg/mL $\alpha$-crystallin in PBS at 35°C.**

The hydrodynamic radius of the fast mode of 0.2 mg/mL $\beta_L$-crystallin, 0.6 mg/mL $\alpha$-crystallin in PBS at 35°C was found to be comparable in size to the size-scale of 0.2 mg/mL $\alpha$-crystallin in PBS at 35°C. $\alpha$-crystallin was previously demonstrated to have a significant effect on the second mean peak, but based on this data it also appears to influence the first mean peak of $\beta_L$-crystallin. If the $\alpha$-crystallin did not have a significant effect on the $\beta_L$-crystallin structure then there would be a peak corresponding to 3 nm as well as 10.5 nm.

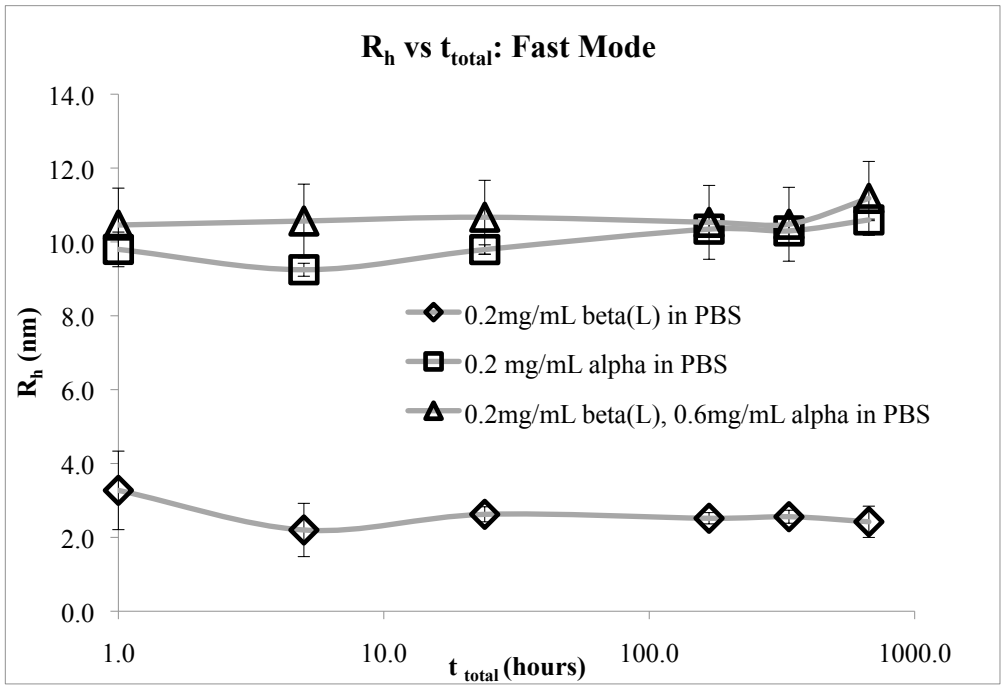


**Figure 2.51 A comparison of the fast modes of 0.2 mg/mL $\beta_L$-crystallin in PBS at 35°C, 0.2 mg/mL $\alpha$-crystallin in PBS at 35°C, and 0.2 mg/mL $\beta_L$-crystallin, 0.6 mg/mL $\alpha$-crystallin in PBS at 35°C.**

A comparison of the average $\Gamma$ versus $q^2$ plot and all of the $\Gamma$ versus $q^2$ data of the second peak revealed low $R^2$ values of 0.546 and 0.327, respectively. The low, dissimilar $R^2$ values indicate instability in the aggregate size. Because there is a reasonable degree of error associated with the second peak, the size of 140 nm is only a guide for visualization of the aggregate. An interesting point to note about the error bars in the average plot is that the degree of error is low for the low angles and high for the high angles. One possible explanation for this is that the aggregate is not following a linear $q^2$ relationship, which would invalidate the use of the Stokes-Einstein equation. However, looking at the distribution of data points in the plot of all of the data indicates that at higher angles there is not a clear trend, therefore the Stokes-Einstein equation is valid in this case.

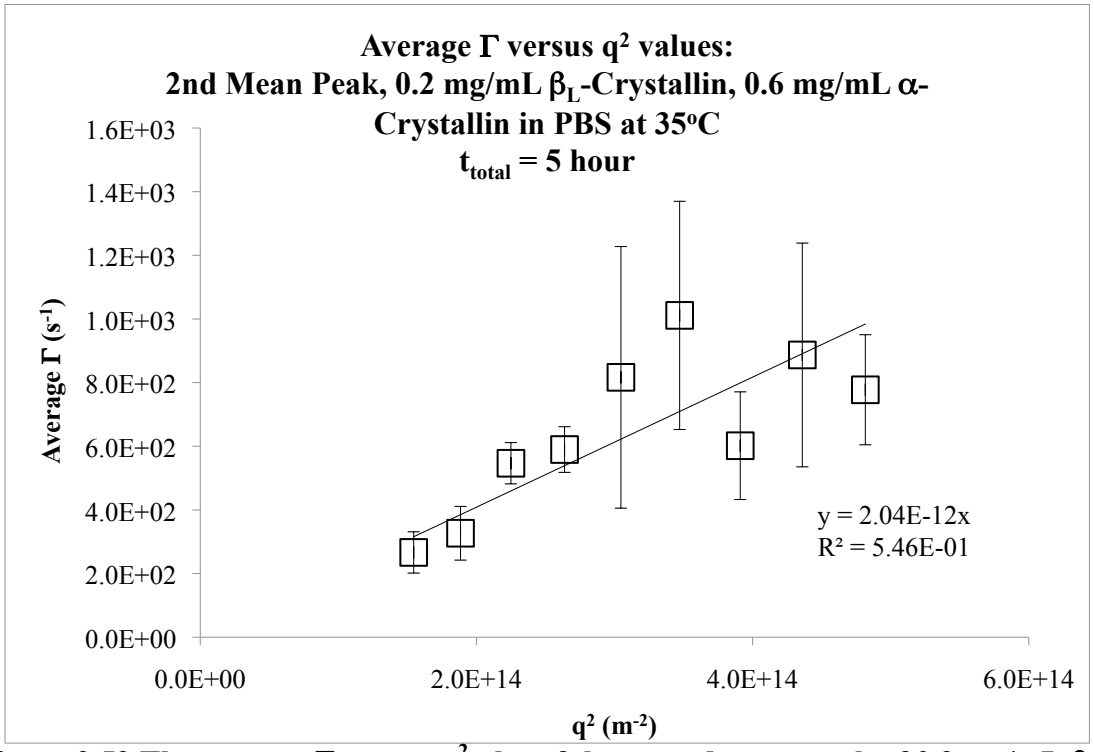


**Figure 2.52 The average Γ versus $q^2$ plot of the second mean peak of 0.2 mg/mL $\beta_L$-crystallin, 0.6 mg/mL α-crystallin in PBS at 35°C.**

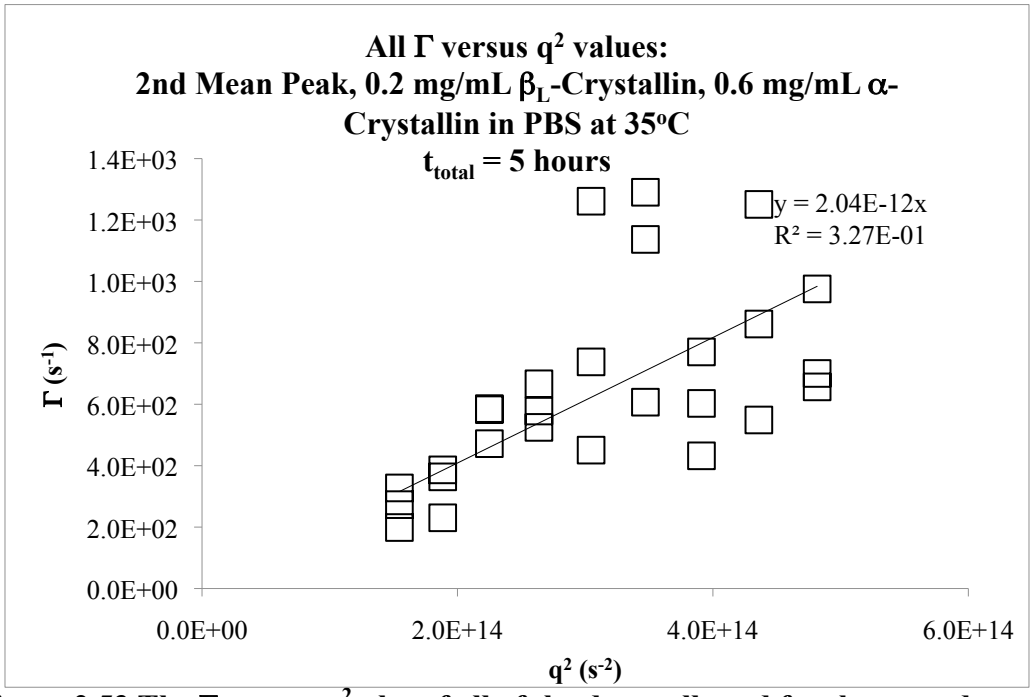


**Figure 2.53 The Γ versus $q^2$ plot of all of the data collected for the second mean peak on 0.2 mg/mL $\beta_L$-crystallin, 0.6 mg/mL α-crystallin in PBS at 35°C.**

## 2.5 Transmission Electron Microscopy

The crystallins were studied using a 200kV transmission electron microscope (TEM). The sample preparation for TEM involved applying a drop of solution onto a 400 mesh copper grid with perforated carbon film on it. The solution was then blotted carefully to thin out the solution layer. The sample was then cooled with liquid nitrogen.

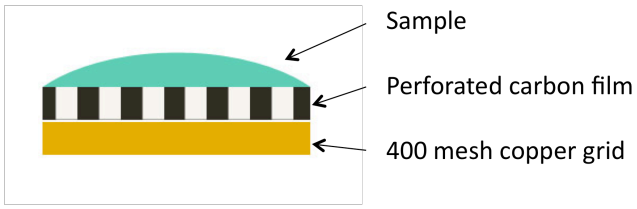


**Figure 2.54 An illustration of the sample preparation for TEM.**

Due to the nature of sample preparation, fast mode hydrodynamic radii are reliable, however the aggregate size is not.

TEM analysis of $\beta_L$-crystallin in water did not reveal any firm conclusions about size-scales. However, dark aggregate clumps were recognizeable on the grids.

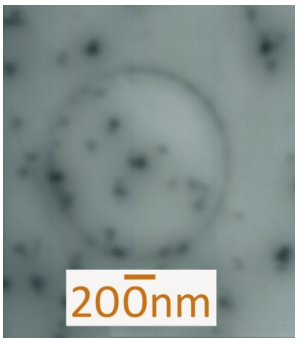


**Figure 2.55 TEM image of 0.2 mg/mL $\beta_L$-crystallin in water.**

When 0.2 mg/mL $\beta_L$-crystallin, 0.6 mg/mL $\alpha$-crystallin in water was analyzed with TEM the dark spots were no longer visible. The sample became a clear film that folded on itself.

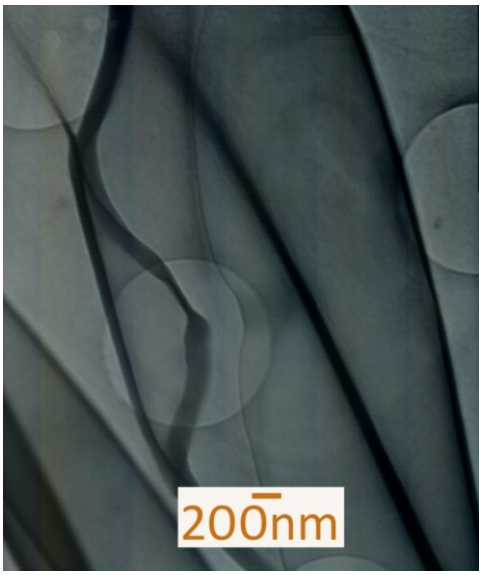


**Figure 2.56 A TEM image of 0.2 mg/mL $\beta_L$-crystallin, 0.6 mg/mL $\alpha$-crystallin in water.**

These samples were also studied at physiological conditions, using the PBS buffer described earlier. In PBS $\alpha$-crystallin was successfully imaged and showed an $R_h$ on the order that was confirmed with light scattering measurements.

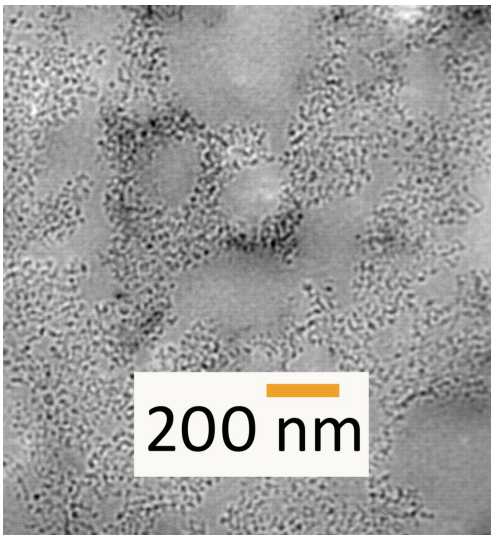


**Figure 2.57 TEM image of 0.2 mg/mL α-crystallin in PBS.**

The combination of 0.2 mg/mL $\beta_L$-crystallin and 0.6 mg/mL α-crystallin again resulted in a sheet. One difference was that with the PBS solvent clumping was visible in the sheet-like formation.

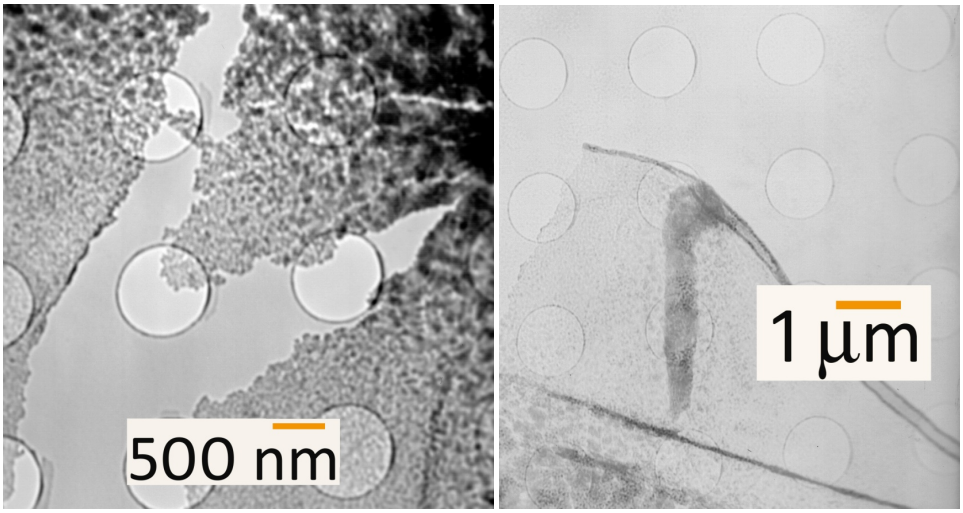


**Figure 2.58 TEM images of 0.2 mg/mL $\beta_L$-crystallin, 0.6 mg/mL α-crystallin in PBS.**

The images produced by TEM support the general conclusions drawn from the DLS data collected at the different conditions.

## 2.6 PH Study

In the next series of experiments the pH of the system was varied. In order to maintain stable pH, phosphate buffered saline (PBS) was used as the solvent for all of the pH study experiments. At all pH values, the probability distribution function of 0.2 mg/mL $\beta_L$-crystallin in PBS at 23$^o$C exhibited multiple modes.

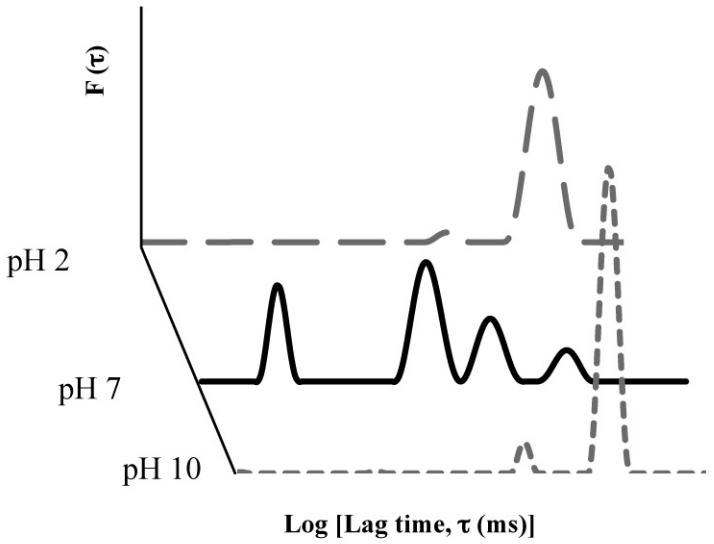


**Figure 2.59 A graph illustrating the probability distribution functions of 0.2 mg/mL $\beta_L$-crystallin in PBS at 23$^o$C at three different pH values.**

The probability distribution functions at all pH values other than physiological pH demonstrated two (and occasionally three) peaks. The third peak did not appear consistently enough to be analyzed. The peaks represented large aggregates. The aggregate $R_h$ values were beyond the range of what DLS can analyze. At a pH of seven, four size-scales were present in solution. The general trend was that at any pH other than physiological pH the individual $\beta_L$-crystallin molecule was not prevalent in solution, only aggregates were common.

The effect of pH on the aggregation of $\beta_L$-crystallin was also studied at 35°C. 0.2 mg/mL $\beta_L$-crystallin in PBS at 35°C was studied at a pH of 2, 4, 6, 6.9, 7, 8 and 10 using DLS. The probability distribution functions of the samples with pH values below physiological pH exhibited predominantly two aggregate size-scales in solution.

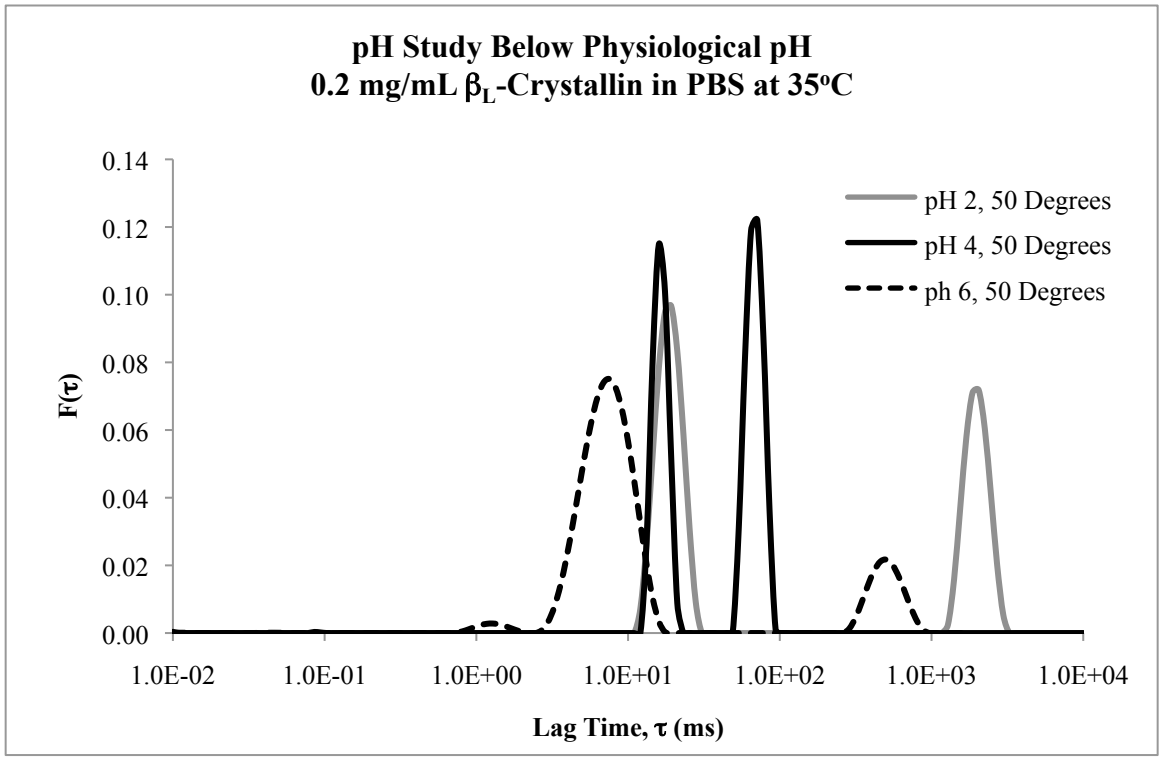


**Figure 2.60 A pH study below physiological pH of 0.2 mg/mL $\beta_L$-crystallin in PBS at 35°C.**

A third peak appeared sporadically and could not be analyzed. The same trend was seen for samples above physiological pH. The aggregates were too large to be accurately analyzed with DLS, therefore no $R_h$ can be reported.

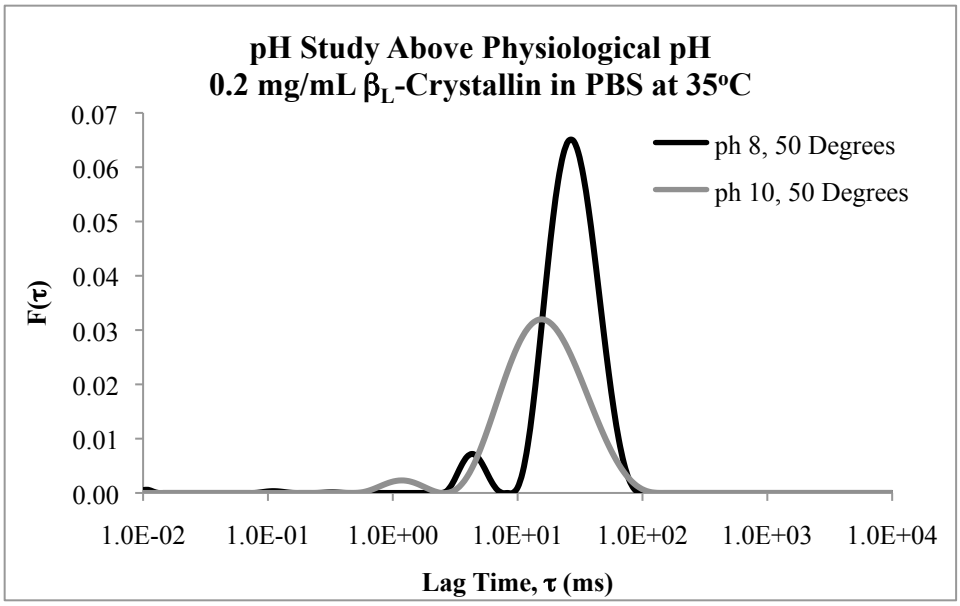


**Figure 2.61 A pH study above physiological pH of 0.2 mg/mL $\beta_L$-crystallin in PBS at 35°C.**

At physiological pH evidence of four size-scales was exhibited. A consistent fast mode was exhibited at physiological pH.

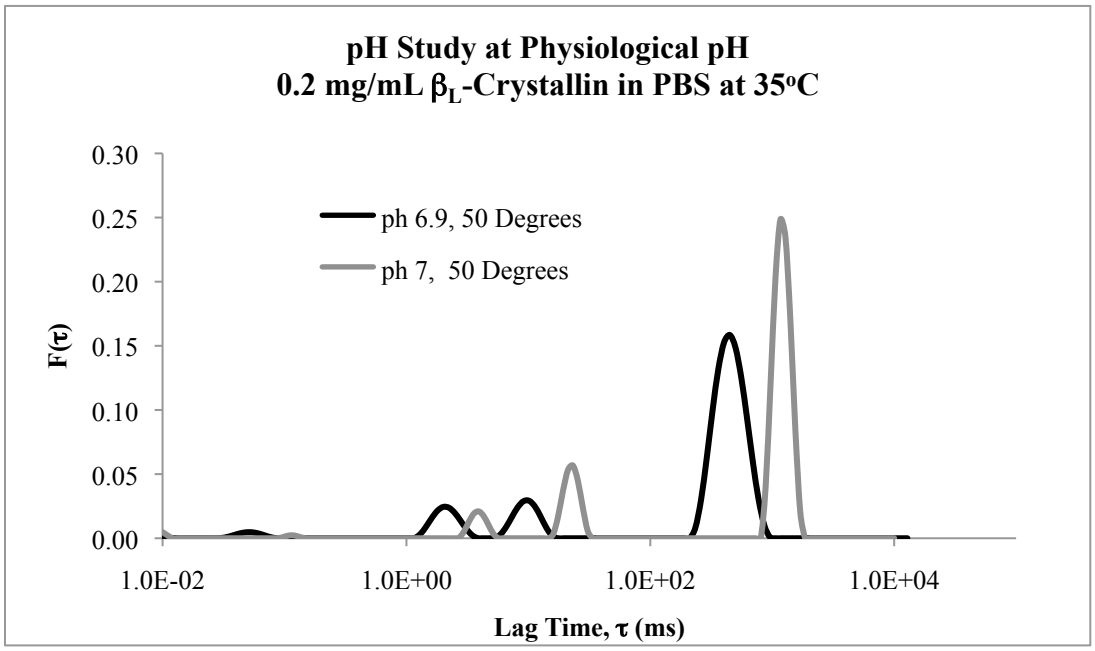


**Figure 2.62 A pH study at physiological pH of 0.2 mg/mL $\beta_L$-crystallin in PBS at 35°C.**

The pH study results at 23°C and 35°C were comparable. The changes in pH in this set of experiments affected the ionization of $\beta_L$-crystallin. Depending upon the pKas of the functional groups on $\beta_L$-crystallin, at lower pHs charge-neutral interactions will dominate and at higher pHs electrostatics will be the significant force.[48] One possible conclusion that can be drawn from these experiments is that at a neutral pH a balance between charge-neutral and electrostatic interactions results in a minimization of aggregation

## 2.7 Charge Model

To further understand the role of electrostatics a charge model was developed. The structure of $\beta_L$-crystallin can be loosely described as a barbell with one of the bulbs having a net negative charge and the other bulb having a net positive charge.[33] The linker is negative.

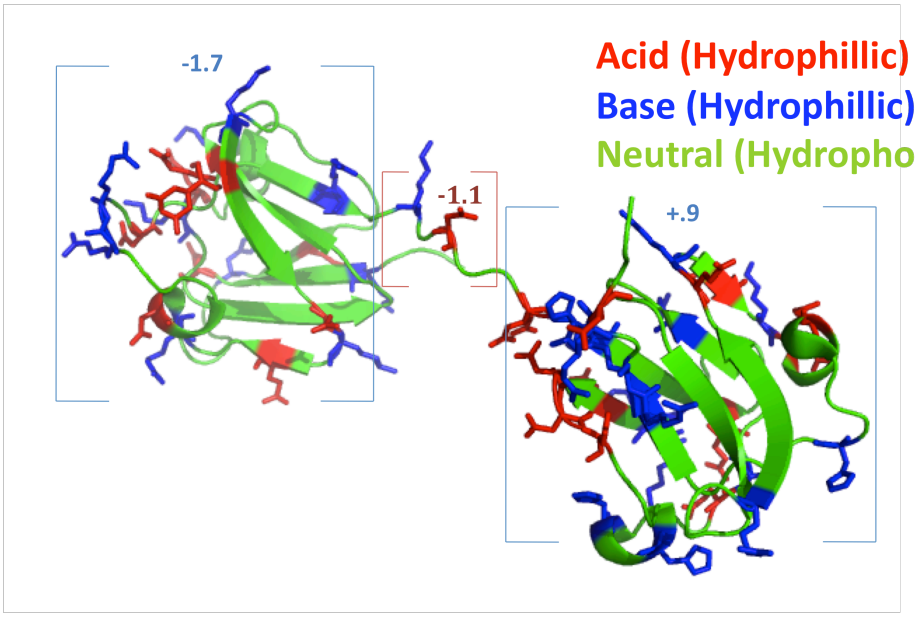


**Figure 2.63 An illustration of the theoretical structure of βb2-crystallin determined using x-ray diffraction.[33]**

Using this model, in collaboration with Jyoti Mahalik, preliminary analyses demonstrated that $\beta_L$-crystallin was more likely to aggregate when strong electrostatic forces were present than when weak electrostatic forces were present.

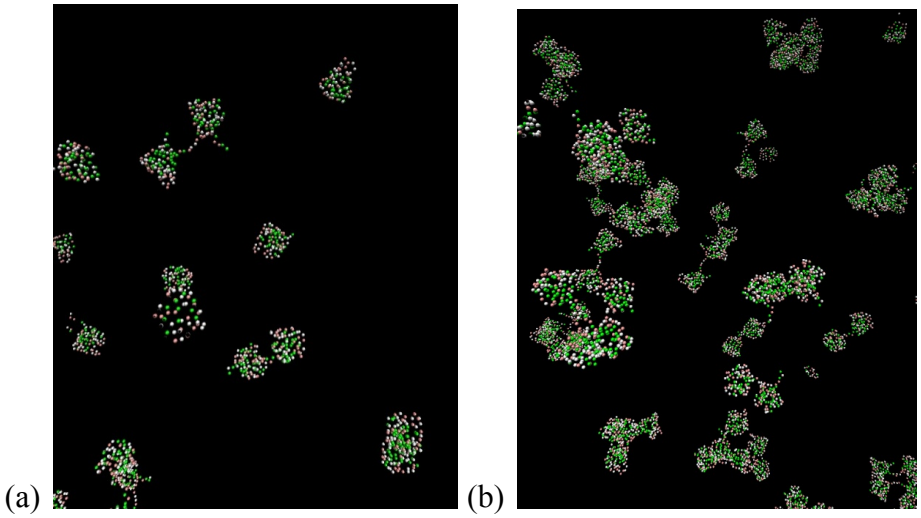


**Figure 2.64 These images are still shots taken from a simulation that Jyoti Mahalik made of $\beta_L$-crystallin using the charge distribution model. Image (a) has weak electrostatic interactions and image (b) has strong electrostatic interactions.**

## 2.8 Future Work

### 2.8.1 Depletion Forces

Another potential method of manipulating aggregation is through additives. The range and strength of the attraction between colloids can be varied by the addition of a polymer. A polymer with a radius of gyration $R_g$ is generally excluded from an area around a colloid defined also by a radius of $R_g$. If two colloids become close enough their depletion zones will overlap and the free volume of the polymer increases. This phenomenon results in depletion forces, which cause aggregation.[49-52] The magnitude of the depletion force is dependent upon the osmotic pressure of the additive.[53]

Organic solutes found in human tears were the initial inspiration for additives. Some of the organic solutes had structures similar to surfactants.[47] A surfactant offered the ability to choose the molecular weight and charge, making it an ideal experimental variable. However preliminary experiments with sodium dodecyl sulfate, an anionic surfactant, and cetyl trimethylammonium bromide, a cationic surfactant, did not have any effect on the aggregate structure.

Another additive that was investigated was polyethylene glycol (PEG). PEG was selected due to its refractive index of 1.45, which is similar to the lens' refractive index of 1.35.[47] The preliminary experiments did not illustrate a clear trend, therefore more investigation is recommended.

### 2.8.2 Reproduction of Results With Human Crystallins

Current work is now underway by Benjamin Mohr to reproduce the results discussed above using human crystallins. The crystallins are synthesized using recombinant DNA technology.

# CHAPTER 3

# LOWER CRITICAL SOLUTION BEHAVIOR OF PROTEIN COPOLYMERS

## 3.1 Introduction

The goal of this project was to study the self-assembly of smart biomaterials for use in drug delivery. The two proteins used for this research were α-helical cartilage oligomeric matrix protein coiled-coil (COMPcc) and β-spiral elastin. COMPcc self-assembles into a homopentamer of parallel α-helical coiled-coils producing a hydrophobic pore that can bind to small molecules, such as vitamin D.[54] Elastin self-assembles into a helical β-spiral.[12] β-spiral elastin exhibits lower critical solution temperature (LCST) behavior.[55] Through recombinant DNA technology these two proteins were combined to make three block copolymers; EC, CE and ECE, where E and C represent β-spiral elastin and COMPcc, respectively.[56, 57] EC and CE were delineated by a difference in end-groups.

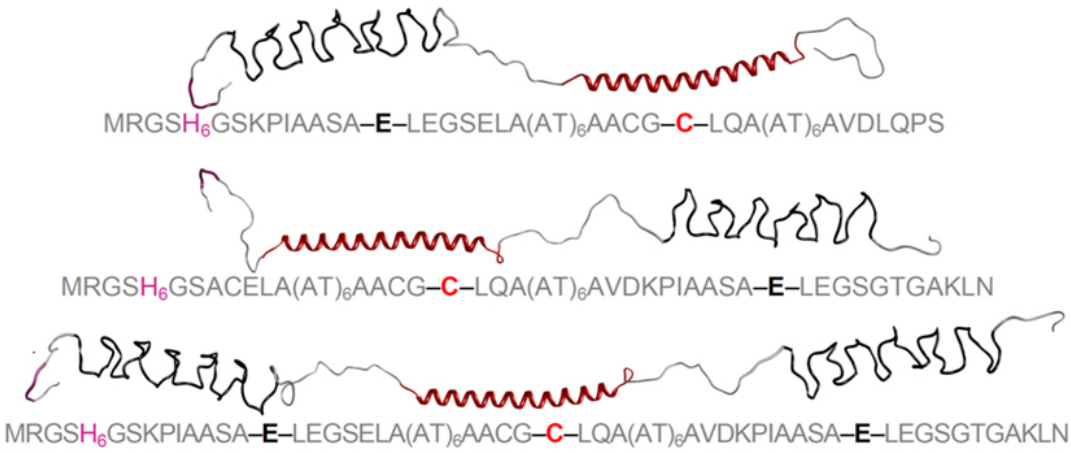


**Figure 3.1 The illustration above depicts the amino acid sequence and corresponding structure of EC, CE and ECE from top to bottom. The molecular weight of EC, CE and ECE is 22,731 Da, 22911 Da and 35,188 Da, respectively.**

### 3.2 Lower Critical Solution Behavior Theory

In this project the block lengths are rearranged in an effort to control the copolymer morphology. The premise for this research comes from the fact that it is well established in literature that manipulating the block lengths of the polymer components can change copolymer morphologies. For example, a diblock of polystyrene-polyacrylic acid displays various micellar-like aggregate structures in 25 wt% water depending upon the block lengths.[58]

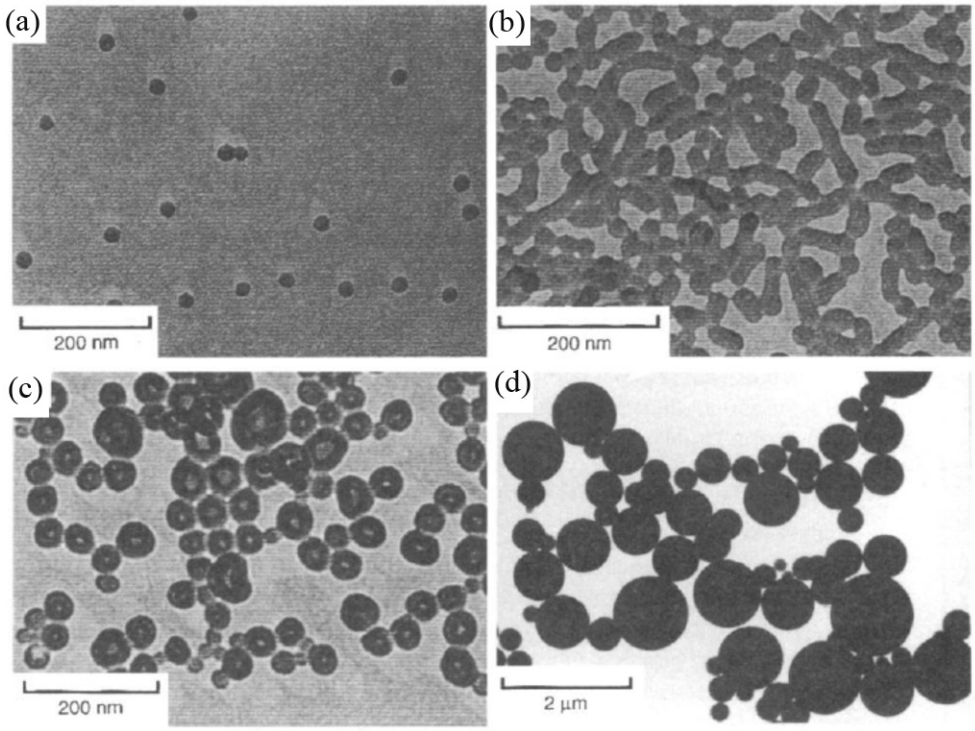


**Figure 3.2 Multiple morphologies of the crew-cut aggregates from block copolymers of (a) 200-b-21, (b) 200-b-15, (c) 200-b-8 and (d) 200-b-4.[58]**

In order to predict the morphology of the copolymer solvent systems, it must be determined if they follow lower critical solution behavior or upper critical solultion behavior. In the case of our system, lower solution critical behavior is obeyed.

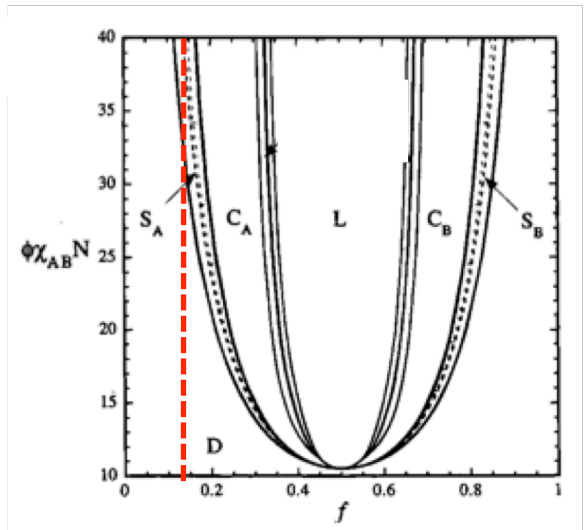


**Figure 3.3 A graph showing the LCST behavior of a diblock copolymer in a neutral good solvent with an N equal to 200.[59]**

Lower critical solution behavior (LCST) is represented by a u-shaped curve that delineates various morphologies based on a graph of $\chi N$ versus polymer fraction, where $\chi$ is the interaction parameter and N is the number of repeat units. Any data points outside of the u-shape represent a disordered system.

With this project, it is best to keep in mind that the E segment is completely hydrophobic, whereas the C segment is both hydrophobic and hydrophilic, with hydrophilicity dominating. This was determined by doing a charge distribution analysis. Based on this model, it is possible that the copolymers could form micelles because micelle formation

requires an attractive force between the amphiphiles, leading to aggregation and a repulsive force that presents unlimited growth.[60]

### 3.3 Materials and Methods

#### 3.3.1 Sample Preparation

The COMPcc insert was PCR assembled by using the following primers:

**1**: 5'-GGGGCCGGATCCGGGGCCGAGCTCGCTGCTACTGCGACCGCCACTGCTA CGGCAACG-3'

**2**: 5'-TGCAGTTCACGCAGCATCTGCGGCGCCAGGTCACCGCATGCCGCCGT CGCCGTTGCCGTAGCAGTG-3'

**3**: 5'-GATGCTGCGTGAACTGCAGGAAACCAACGCGGCGCTGCAGGAC GTTCGTGAACTGCTGCGTCAGCAG-3'

**4**: 5'-GACGCGTCAGATTCCATAACGGTGTTTTTCAGGAAGGTGATTTCTTT AACCTGCTGACGCAGCAGTTC-3'

**5**: 5'-GTTATGGAATCTGACGCGTCTGGTCTGCAGGCTGCCACTGCAACGG CTACTGCAACCGCGACGGCTA-3'

**6**: 5'-GGCCCCAAGCTTCGCACCGGTACCGGCTCCGTCGACCGCCGTAG CCGTCGCGGTTGC-3'

**7**: 5'-GGGGCCGGATCCGG-3'

**8**: 5'-GGCCCCAAGCTTCGC-3'

The elastin inserts were amplified using the following primers:

BamHI:*5'-ggaggccGGATCCaagccgattgcggctagcgcggtgccgg-3'*

SacI:*5'*-gccccc*GAGCTC*cgatccctcgagcggcaccccgac-3'

SalI:*5'-ggaggccGTCGACaagccgattgcggctagcgcggtgccgg*-3'

HindIIII: *5'*-ggcccc*AAGCTT*cgcaccggtacccgatccctcgagcggcaccccgac-*3'*

The next step was cloning EC, CE and ECE. A modular approach was used to construct all three genes in which the COMPcc DNA bearing the linker regions and appropriate restriction sites were PCR assembled digested with SalI and SacI and gel purified. The resulting 278 bp fragment was ligated into pQE30 yielding pQE30/C.

The 450 bp elastin gene was PCR amplified from the pUC19RGDELF (gift from D. Tirrell) and was cloned into pQE30/C between the restriction sites BamHI and SacI to generate pQE30/EC, or SalI and HindIII yielding pQE30/CE, or all 4 sites to yield pQE30/ECE. The clones were verified by DNA sequencing.

The plasmids bearing the polymers were transformed into zymo competent cells. Protein expression was carried out with a 1:100 dilution of starter culture into LB (1 L) bearing ampicillin (200 mg mL-1) and incubated at 37 °C and 250 rpm until the OD600 reached 2.0. A media shift was performed by pelleting the cells via centrifugation at 6000 rpm, 4 °C for 15 minutes and resuspending the cells in fresh LB containing ampicillin (200 µg mL-1) and isopropyl b-D-1 thiogalactopyranoside (IPTG, 100 µg mL-1). Protein induction took place for 13 hours at 30 °C, 250 rpm.

Cells were harvested via centrifugation at 8000 rpm, 4 °C for 20 min. Pellets were

collected and stored in the -80 °C until purtification. Cell pellets (1 L) were suspended in lysis buffer (50 mL, 115 mM monobasic sodium phosphate, 8 M urea, 10 mM Tris-HCl, pH 8.0) and incubated at -80°C for 4 hours. The lysate was thawed at 4 °C and homogenized with a French press (40K-cell; ThermoScientific) at 23 600 psi. The lysate was centrifuged at 20 000 rpm for 40 minutes at 4 °C.

The crude extract was allowed to bind on a rotating mixer to Ni-NTA agarose beads (2.5 mL, Qiagen) for 2 hours. The protein-bead mixtures were packed into columns (2 mL) and eluted with a decreasing step-wise pH gradient of lysis buffer, pH 8.0 – 3.25. Alternatively, the harvested cells were resuspended in lysis buffer (50 mL, 50 mM Na2HPO4, 20 mM imidazole, 6 M urea, pH 8.0) and stored at -80 °C for > 4 hours. The resuspended cells were then thawed at 4 °C and mechanically lysed in a French press (40K-cell, Thermo Scientific) at 23600 psi. The whole cell lysate was then centrifuged at 20,000 rpm for 40 min at 4 °C. The supernatant was applied to a HiTrap IMAC FF column (1 mL, GE Life Sciences), which was previously charged with NiCl2 (2 mL, 0.5 M) and subsequently equilibrated with lysis buffer using an ÄKTA purifier system (GE Life Sciences). The protein was eluted with a linear imidazole gradient (20 to 500 mM across 10 mL). Fractions containing protein (ca. 5 mL, determined by SDS-PAGE), were pooled and applied to a HiLoad 16/60 Superdex 75 pg gel filtration column (GE Life Sciences), which was pre-equilibrated with lysis buffer. All ÄKTA-based chromatography was performed at 4 °C. The eluted pure fractions were pooled and dialyzed (3500 MWCO) against either deionized water (500:1 dH2O/eluent) or phosphate buffer (10 mM, pH 8.0) over 3 batches of water for 2, 2, and 17 hours.

### 3.3.2 Light Scattering

An ALV instrument with an argon laser ($\lambda$ = 514.5 nm) was used to collect the Dynamic Light Scattering (DLS) data from $35^o$-$65^o$ in $5^o$ increments and from $70^o$-$90^o$ in $10^o$ increments. An ALV5000 correlator was used to analyze the data. The vertical Small Angle Light Scattering (SALS) apparatus consists of a He/Ne laser ($\lambda$ = 633 nm) and a CCD camera as the detector. The DLS experiments were performed on each of the three copolymers at a constant concentration of 0.15 mg/mL in water at a pH of 8.

In DLS, histograms of correlation time $\tau$ (reciprocal of decay rates $\Gamma$) for each of the scattering angle were constructed for each sample at a prescribed temperature. From these histograms for various scattering angles, decay rates were plotted against $q^2$, where q is the scattering wave vector. The slope of the linear line relating $\Gamma$ and $q^2$ is the diffusion coefficient, which upon the use of the Stokes-Einstein relation gives the hydrodynamic radius, $R_h$. In applying the Stokes-Einstein relation, the temperature-dependent viscosity of water is used.

## 3.4 Results

### 3.4.1 Analysis of ECE Triblock

ECE was analyzed at $5^oC$, $10^oC$, $15^oC$, $20^oC$, $25^oC$, $27^oC$, $28^oC$, $29^oC$, $30^oC$, $31^oC$, $32^oC$, $33^oC$, $35^oC$, and $40^oC$. The first temperature at which data was collected was $5^oC$ and then the sample was heated in five-degree increments until the normalized intensity

correlation function exhibited a change. Once a change was noted, the temperature was increase in one-degree increments. Data was collected three times for each temperature.

For each sample analyzed, the goal was to determine the transition temperature by looking for changes in the aggregation behavior. The normalized intensity correlation function was regular and smooth above and below the transition temperature, indicating reliable data collection and minimization of dust. An example of a typical normalized intensity correlation function above and below the transition temperature is shown below.

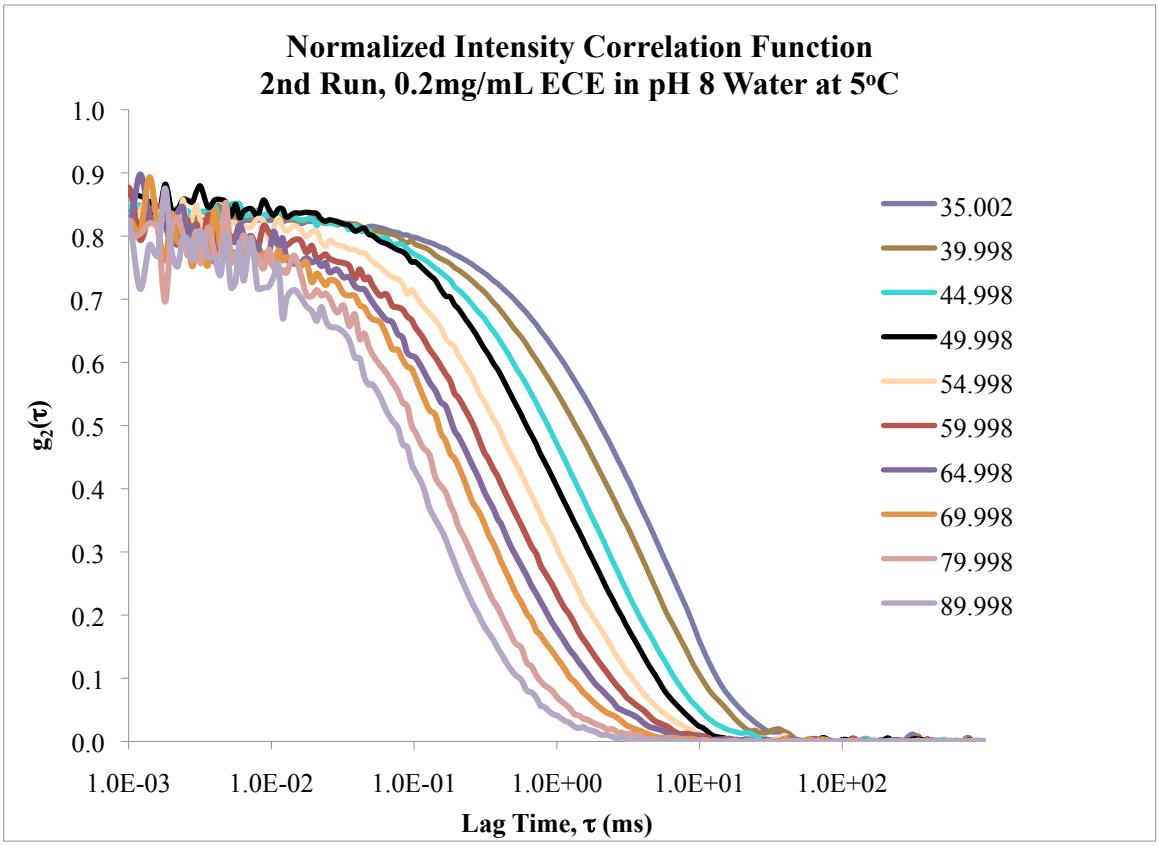


**Figure 3.4 The normalized intensity correlation function of 0.2 mg/mL ECE in pH 8 water at 5°C.**

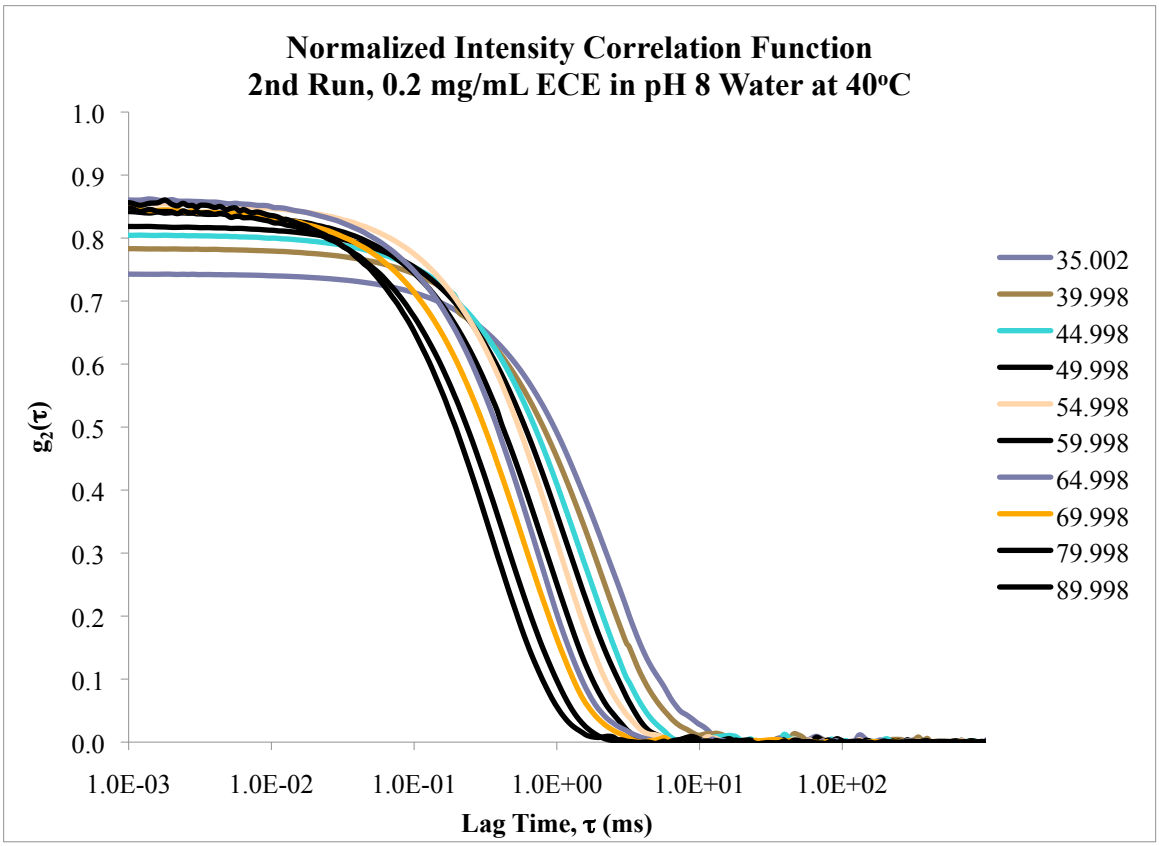


**Figure 3.5 The normalized intensity correlation function of 0.2 mg/mL ECE in pH 8 water at 40°C.**

The only significant difference between the graphs is the smoothness. At higher temperatures the normalized intensity correlation function is smoother. Smoothness of the graph can be controlled by the time allotted for data collection. Increasing the temperature is essentially like speeding up the molecular motion and therefore increasing the data collection time. All of the runs were for 60 seconds regardless of temperature.

The normalized intensity correlation functions were converted into probability distribution functions. A comparison of probability distribution functions below, at and above the transition temperature demonstrated how the peak(s) change with temperature.

Above and at the transition temperature there was only one peak. As the temperature increased the peak narrowed. A narrow peak is indicative of a narrow size distribution.

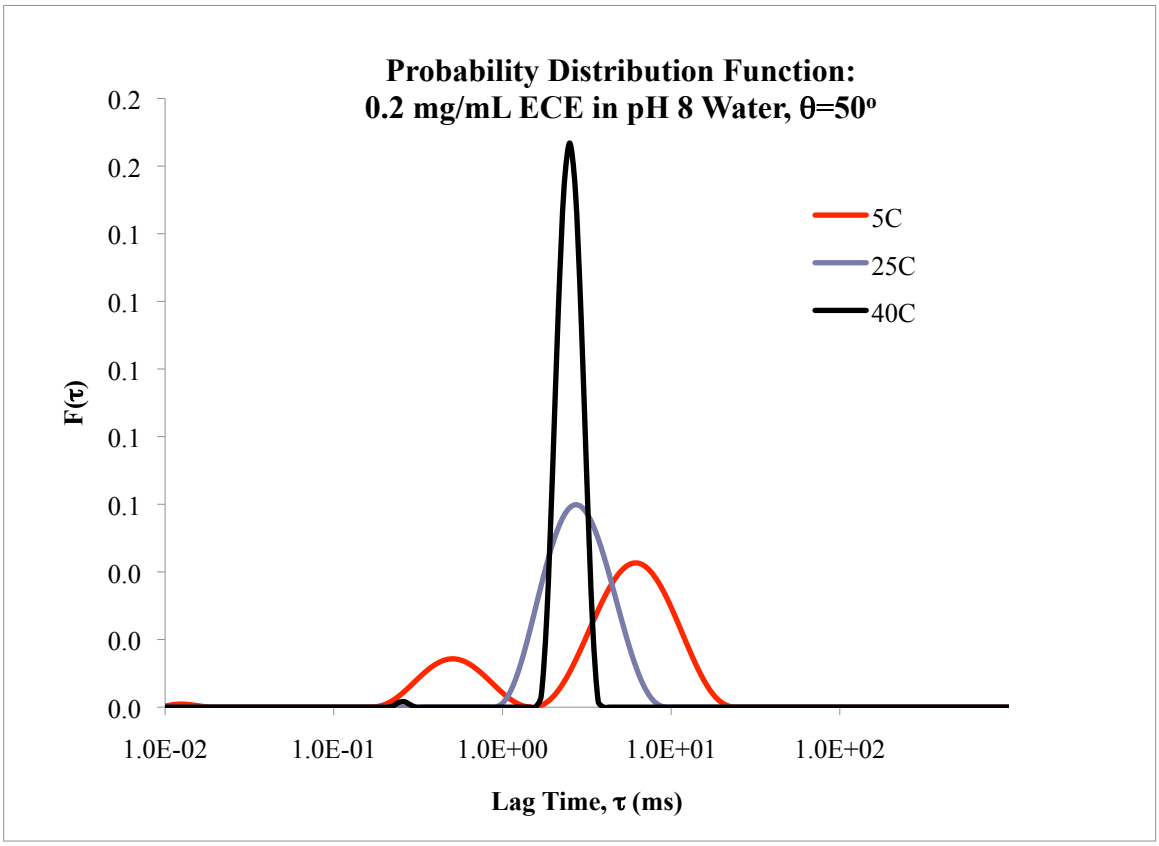


**Figure 3.6 A comparison of the probability distribution functions below, at and above the transition temperature. All data was collected with the goniometer at 50 degrees.**

The two modes below the transition temperature were a fast and a slow mode. The slow mode represented a micelle structure, whereas the fast mode was a single chain. The single chain had a hydrodynamic radius of 18.0 nm at temperatures analyzed below 25°C. The slow mode hydrodynamic radius decreased from 242.0 nm at 5°C to 72.0 nm at 20°C.

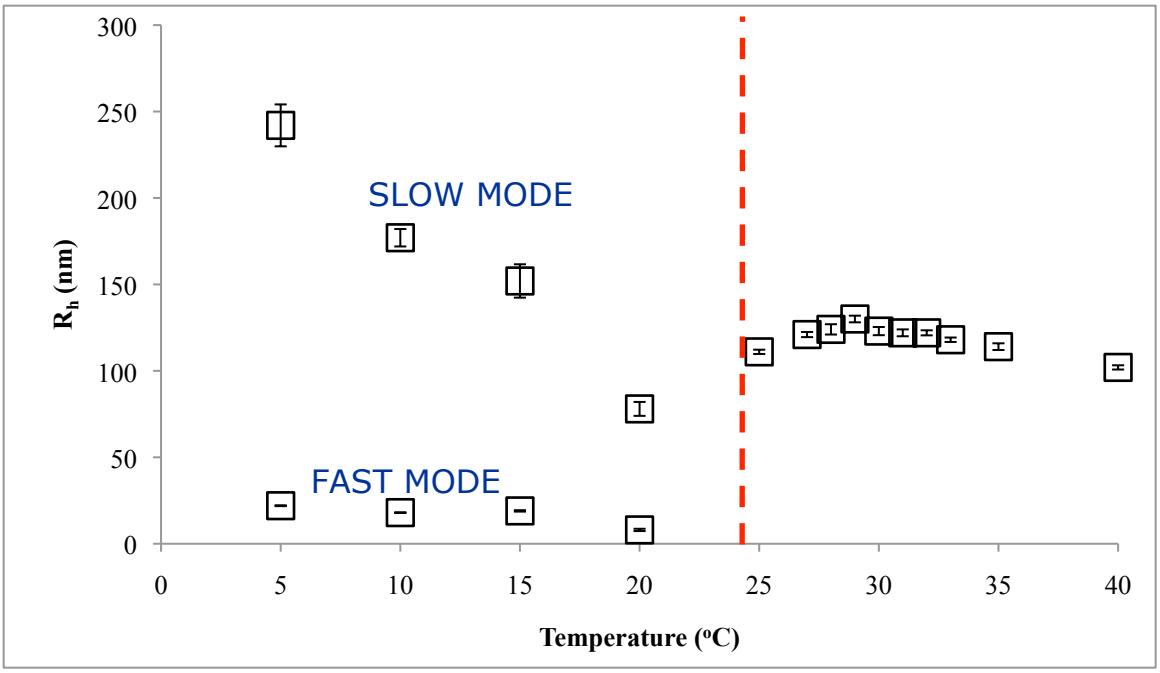


**Figure 3.7 A graph of the hydrodynamic radius, $R_h$, versus the temperature of 0.2 mg/mL ECE at pH 8 deionized water. The transition temperature is marked with a dashed line at 25°C.**

Above the transition temperature of 25°C, one hydrodynamic radius size-scale was preferred, 122.0 nm. The change in hydrodynamic radius of the micelle is likely due to trapped water being expelled from the interior as the temperature is increased, until a critical value is reached where there is no longer any water in the interior.[61]

A comparison of the average data and all of the data collected for Γ versus $q^2$ plots at 5°C, 25°C and 40°C provides insight into the accuracy of the hydrodynamic radius values reported.

At 5°C both a fast and slow mode existed. The fast mode displayed two good fit values corresponding to the two different methods of plotting the Γ versus $q^2$ data. The high fit values indicated that the data was repeatable.

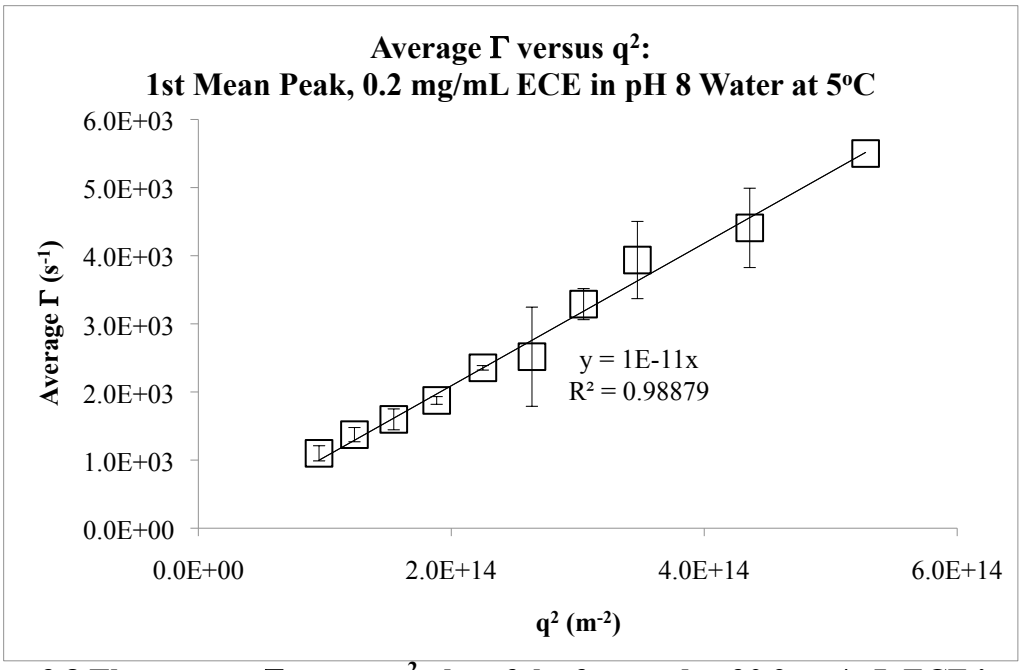


**Figure 3.8 The average Γ versus $q^2$ plot of the fast mode of 0.2 mg/mL ECE in pH 8 water at 5°C.**

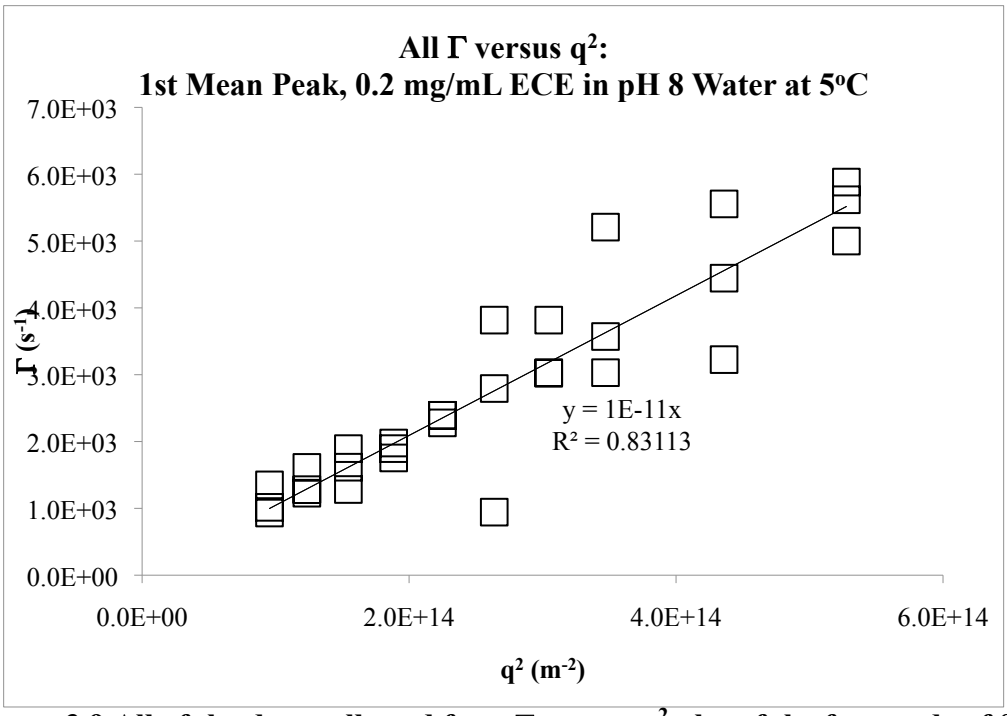


**Figure 3.9 All of the data collected for a Γ versus $q^2$ plot of the fast mode of 0.2 mg/mL ECE in pH 8 water at 5°C.**

The slow mode produced very good fit values in both methods of data analysis, however the fit was noticeably higher in the average method. The discrepancy in fit values is due to the wider distribution at higher angles, which is common for aggregates. Both the fast and the slow modes at 5°C had a relatively good degree of accuracy as evidenced by the high $R^2$ values.

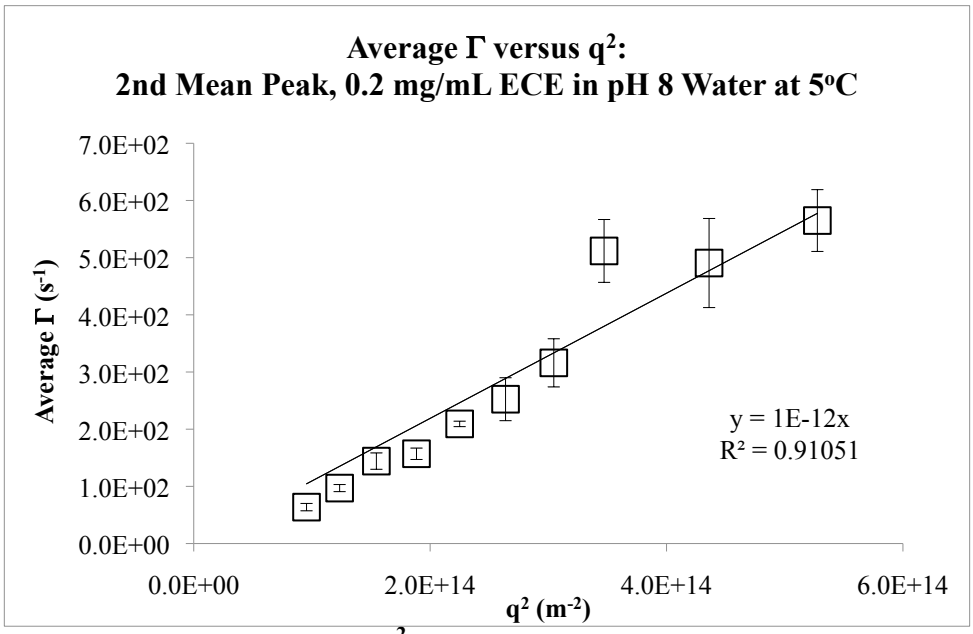


**Figure 3.10 The average Γ versus $q^2$ plot of the slow mode of 0.2 mg/mL ECE in pH 8 water at 5°C.**

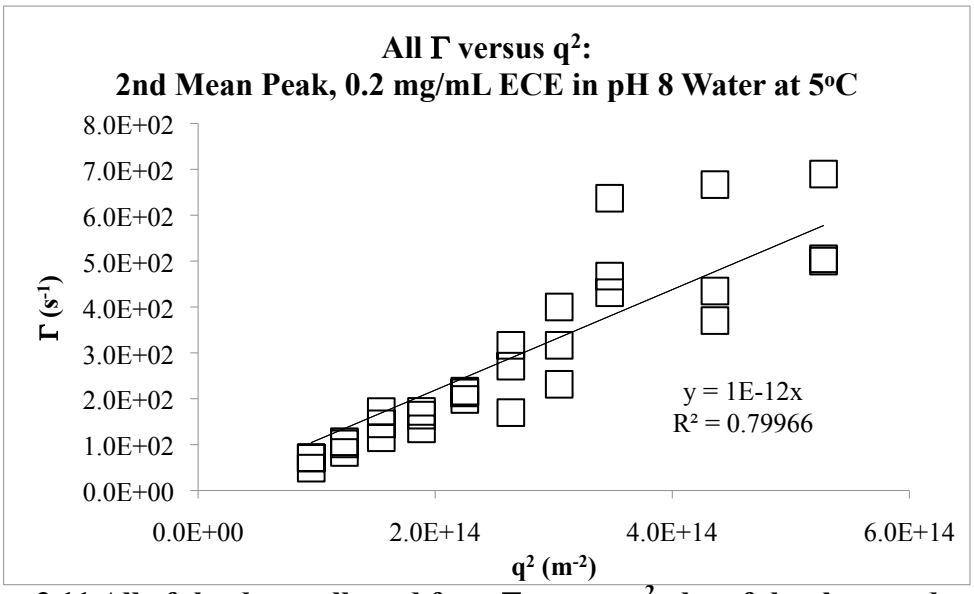


**Figure 3.11 All of the data collected for a Γ versus $q^2$ plot of the slow mode of 0.2 mg/mL ECE in pH 8 water at 5°C.**

At 25°C only one size-scale was present. Both methods of analysis using the Γ versus $q^2$ plot produced high fit values, indicative of reliable data. The fit values were higher than

those at lower temperatures, indicating a smaller size distribution range. The hydrodynamic radius that corresponded to the graphs was 111 nm.

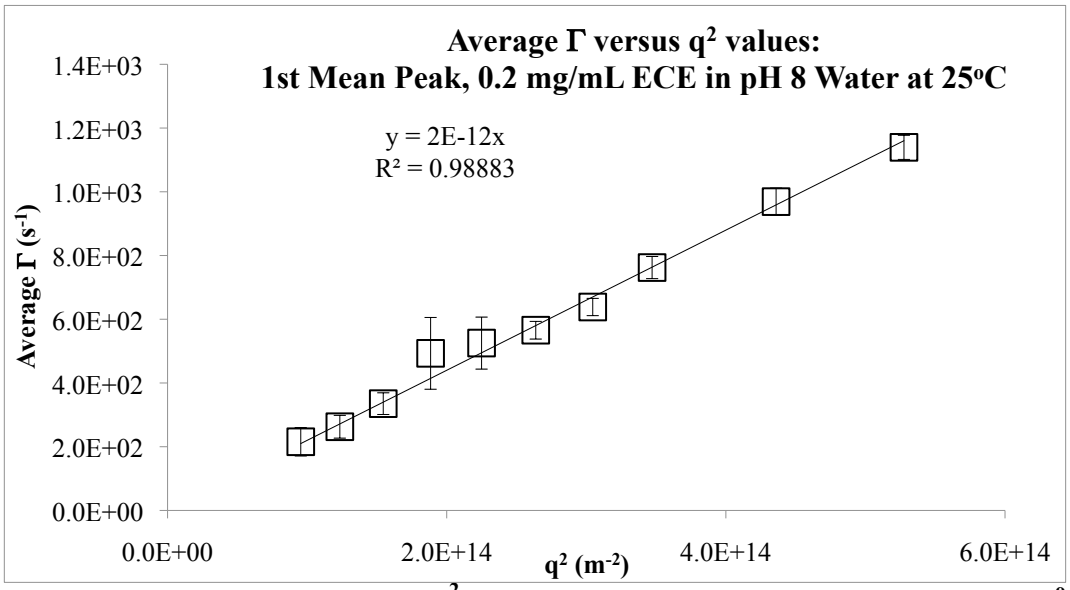


**Figure 3.12 The average Γ versus $q^2$ plot of 0.2 mg/mL ECE in pH 8 water at 25°C.**

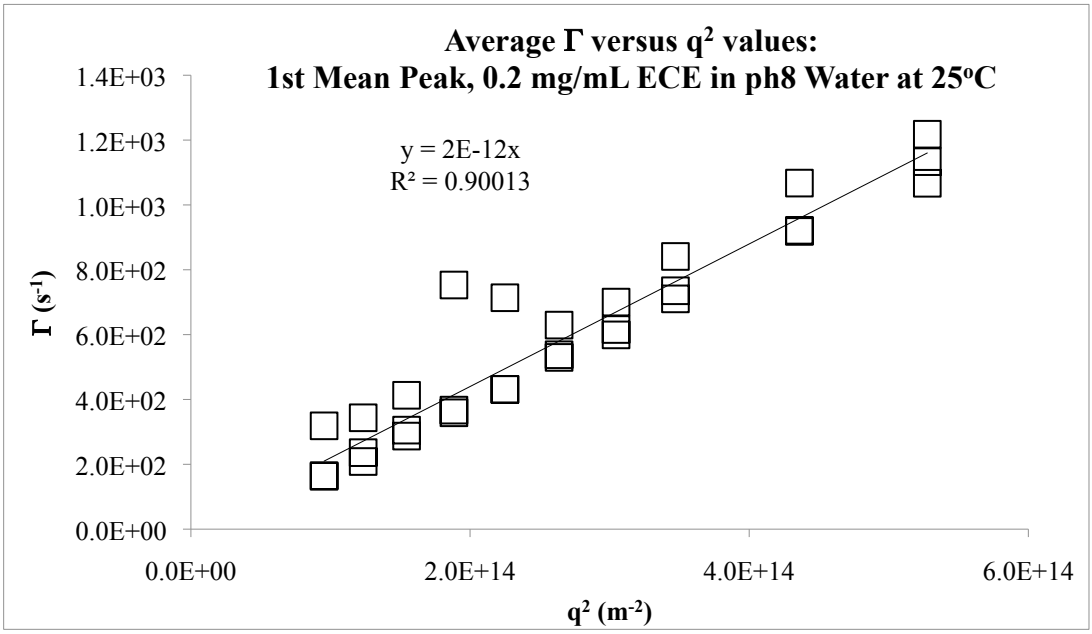


**Figure 3.13 All of the data collected for a Γ versus $q^2$ plot of 0.2 mg/mL ECE in pH8 water at 25°C.**

The Γ versus $q^2$ plots comparing the average and all of the data collected at 40°C reveal very accurate and repeatable data. The hydrodynamic radius of 102 nm is very reliable. It is interesting to note that the $R^2$ value is even higher than at 25°C.

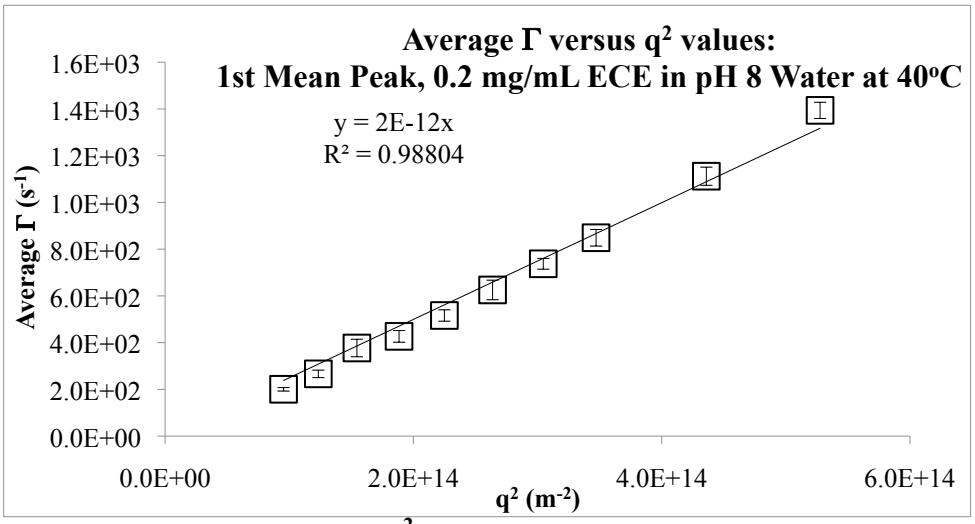


**Figure 3.14 The average Γ versus $q^2$ plot of 0.2 mg/mL ECE in pH 8 water at 40°C.**

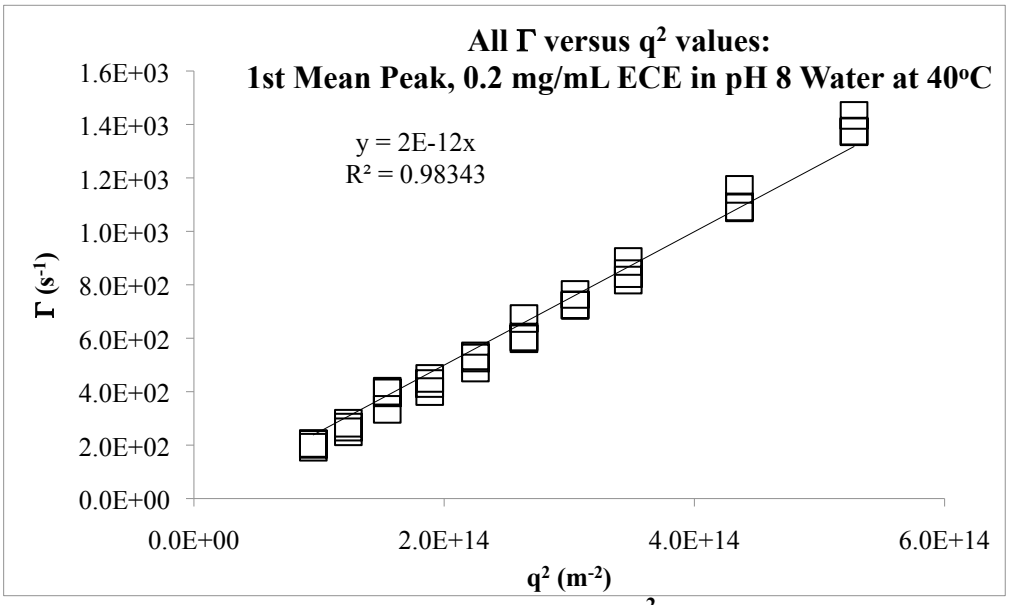


**Figure 3.15 All of the data collected for a Γ versus $q^2$ plot of 0.2 mg/mL ECE in pH 8 water at 40°C.**

The $R^2$ values of the $\Gamma$ versus $q^2$ plots, for both methods, increase at and above the transition temperature. Above the transition temperature a specific size-scale is preferentially selected for by nature.

### 3.4.2 Analysis of EC Diblock

EC exhibited similar behavior to ECE, despite the fact that one was a diblock and the other a triblock. The similarity between the two copolymers was visible in the presence of two size-scales below the transition temperature and one size-scale above. However, the structural difference did have an impact on the behavior of EC. The single size-scale visible above the transition temperature increased in size as time passed. EC exhibited spinodal decomposition.

The normalized intensity correlation function of EC below and above the transition temperature provides insight into the sample. The normalized intensity correlation function at $5^oC$ was very smooth, representative of dust-free samples. There were no irregular shifts in the curve as the experimental capture time passed. This indicated that no kinetic changes were taking place on the time-scale of the experiment. The $35^o$ measurement was made first and the $90^o$ last. If any kinetic changes had taken place the $90^o$ curve would have been significantly different in shape and/or position on the y-scale than the $30^o$ curve.

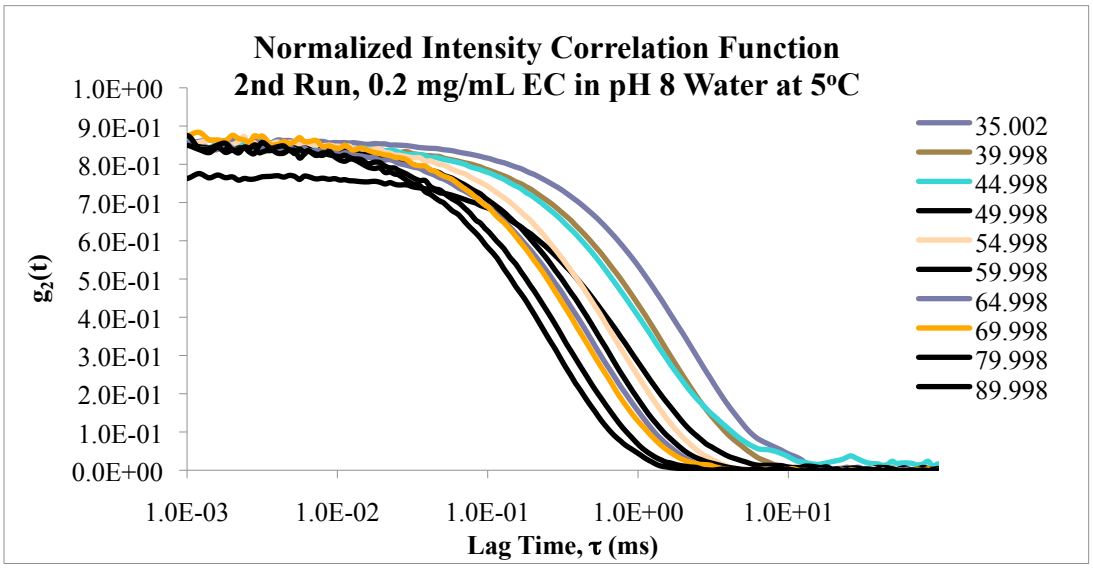


**Figure 3.16 The normalized intensity correlation function of 0.2 mg/mL EC in pH 8 water at 5°C.**

At the transition temperature the normalized intensity correlation function was extremely smooth. Based on the regularity of the curves, there were not any kinetic changes taking place on the time-scale of the experiment at the transition temperature.

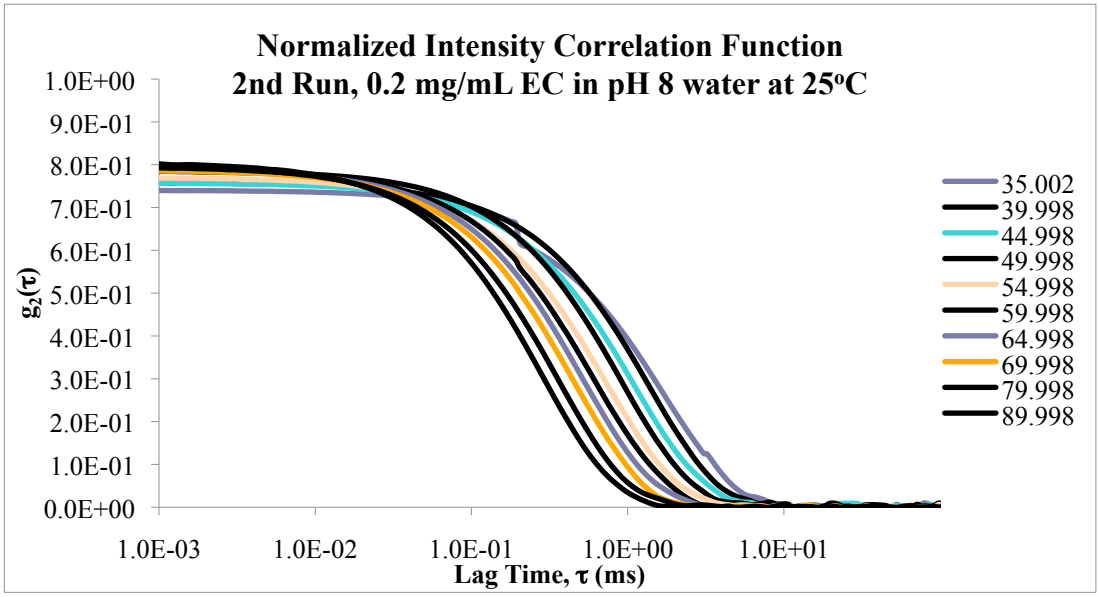


**Figure 3.17 The normalized intensity correlation function of 0.2 mg/mL EC in pH 8 water at 25°C.**

The normalized intensity correlation function above the transition temperature became increasing unstable as temperature and time increased. This instability was visible by the presence of irregular step-function-like dips in the curves. Above the transition temperature the data was difficult to analyze. The normalized intensity correlation function at 30°C had dips and shifts in the y-axis, indicative of kinetic changes in the aggregate on the time-scale of the experiment.

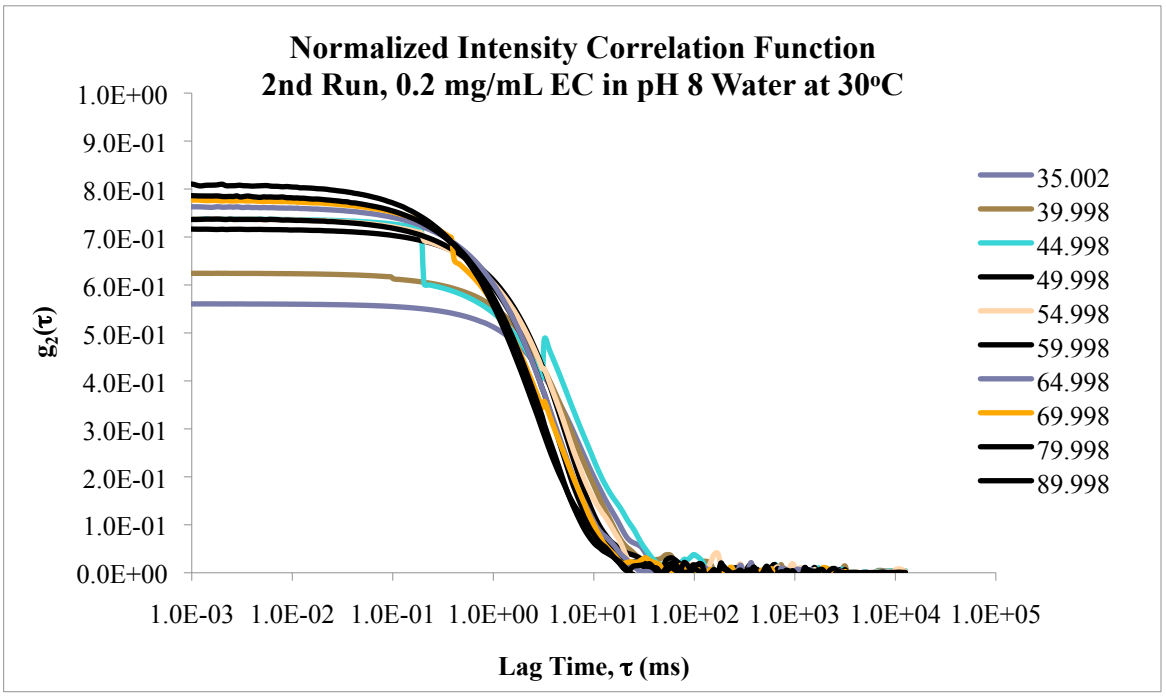


**Figure 3.18 The normalized intensity correlation function of 0.2 mg/mL EC in pH 8 water at 5°C.**

The probability distribution function, derived from the normalized intensity correlation function, shows the change in preference from two size-scales below the transition temperature to one size-scale at the transition temperature.

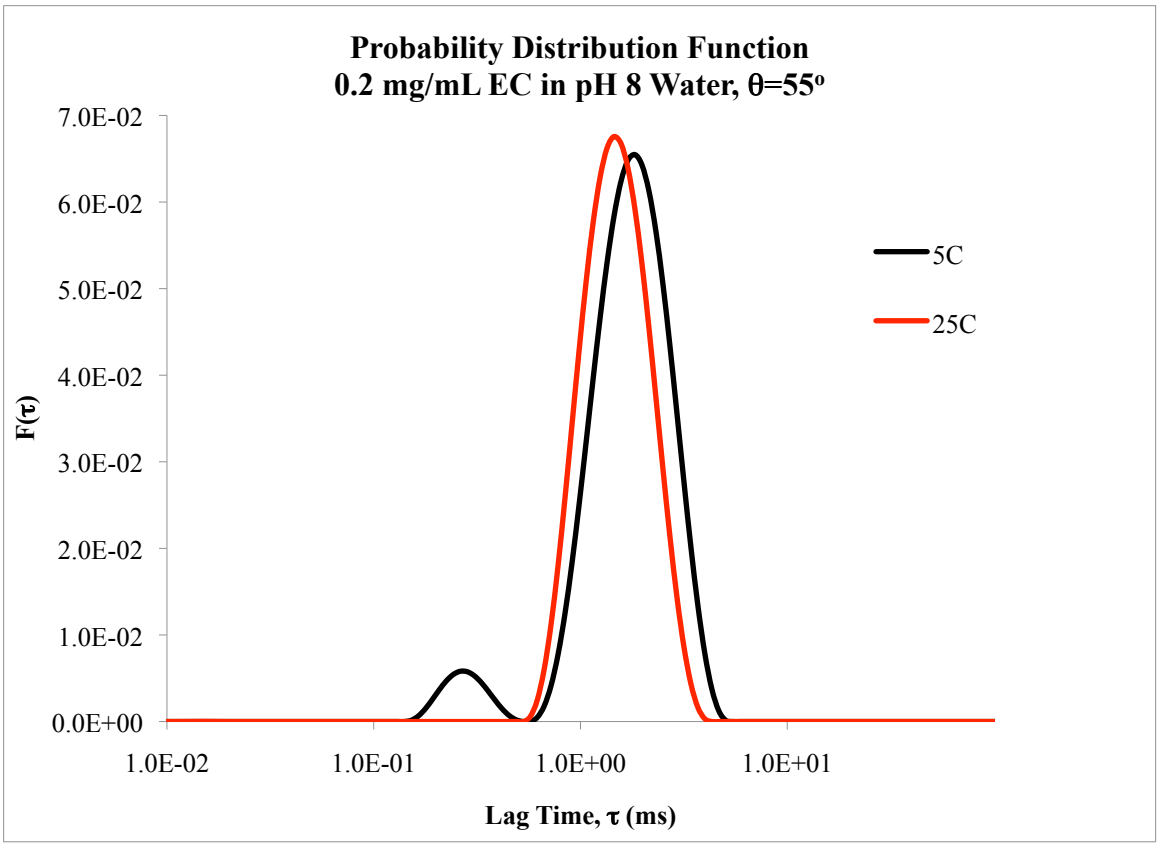


**Figure 3.19 A comparison of the probability distribution functions below and at the transition temperature of 0.2 mg/mL EC in pH 8 water. The measurements were taken with the goniometer set at 55°.**

The Γ versus $q^2$ plot below and at the transition temperature was analyzed in the two different methods described previously. Below the transition temperature the first mean peak had a discrepancy in the $R^2$ values produced by the two different analysis methods. The discrepancy indicated that the size-scale reported, 4 nm, had a high degree of error associated with it.

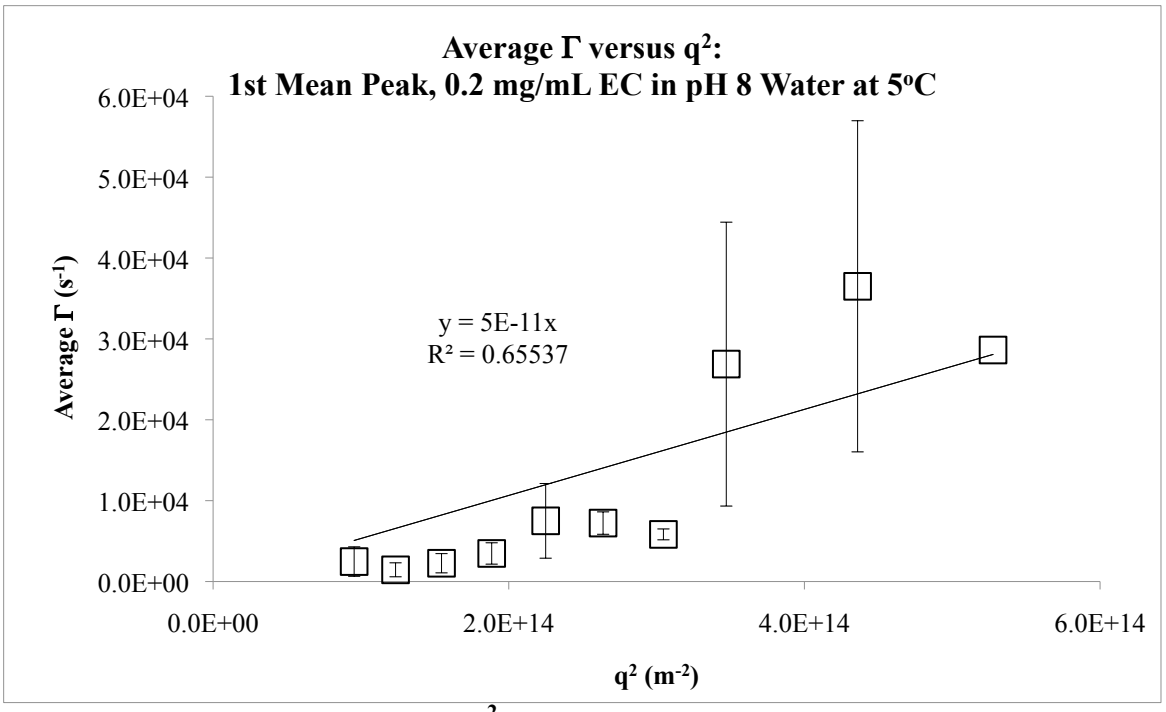


**Figure 3.20 The average Γ versus $q^2$ plot of the first mean peak of 0.2 mg/mL EC in pH 8 water at 5°C.**

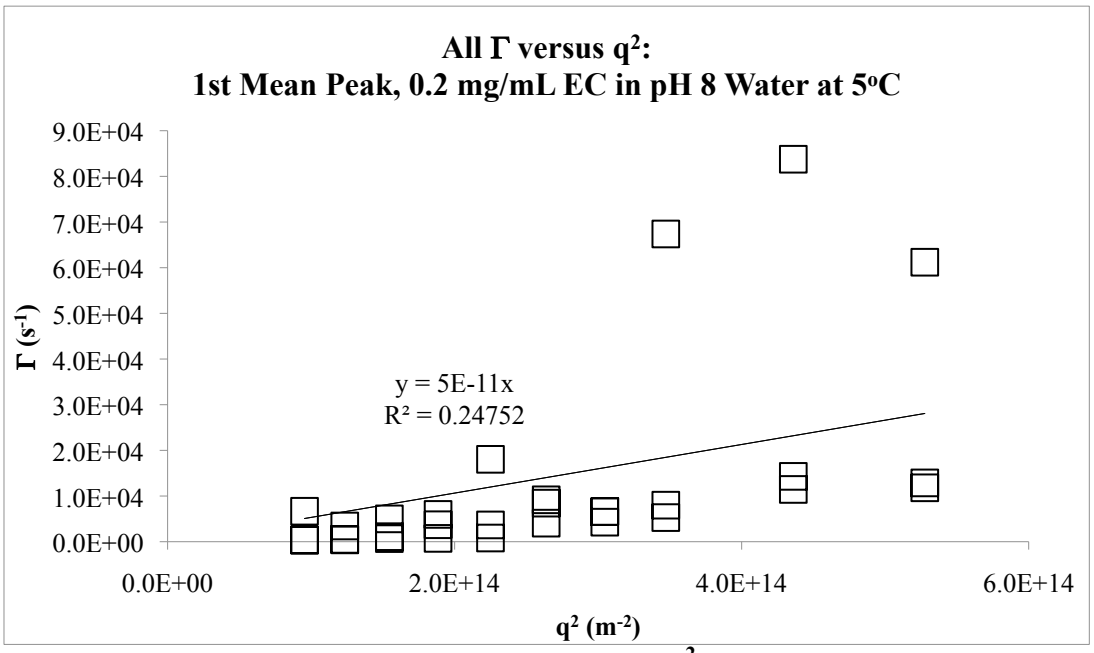


**Figure 3.21 All of the data collected in a Γ versus $q^2$ plot of the first mean peak of 0.2 mg/mL EC in pH 8 water at 5°C.**

The second mean peak was considerably more accurate. The $R^2$ values associated with both methods were above 0.9. The good fit on the aggregate and the poor fit on the smaller size-scale could be attributed to the smaller size-scale supplying the aggregate with more polymer. For this to be a possibility the process would have to be happening on a time and size-scale that would not significantly affect the data collection.

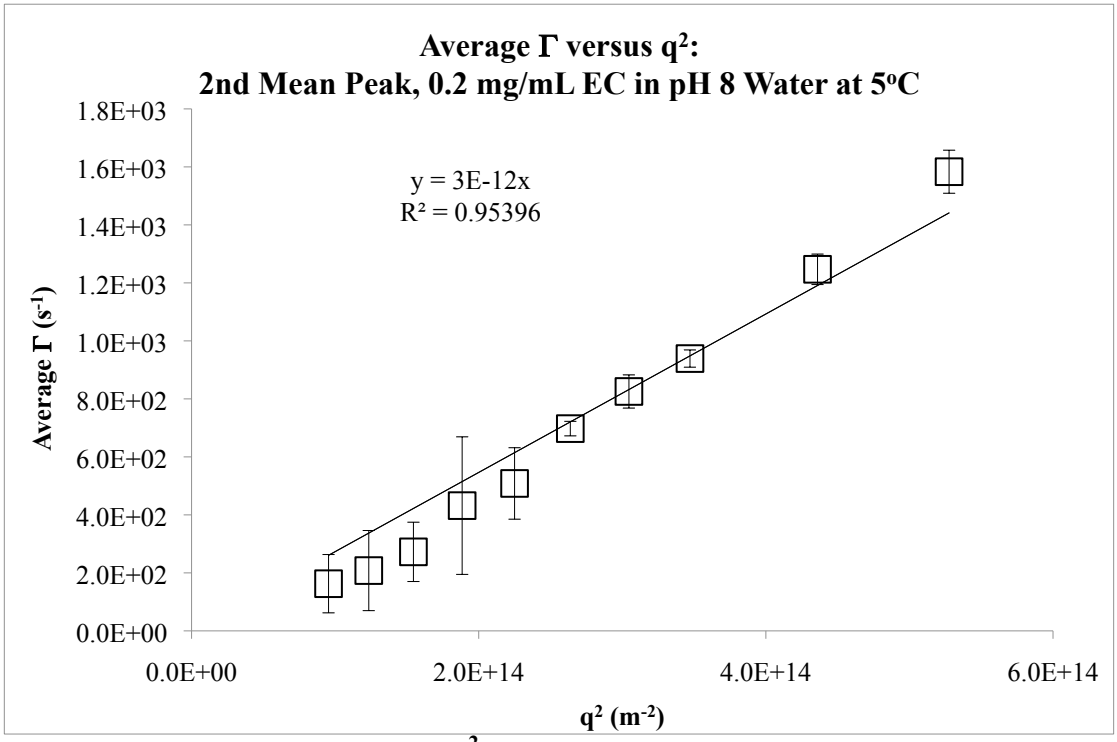


**Figure 3.22 The average Γ versus $q^2$ plot of the second mean peak of 0.2 mg/mL EC in pH 8 water at 5°C.**

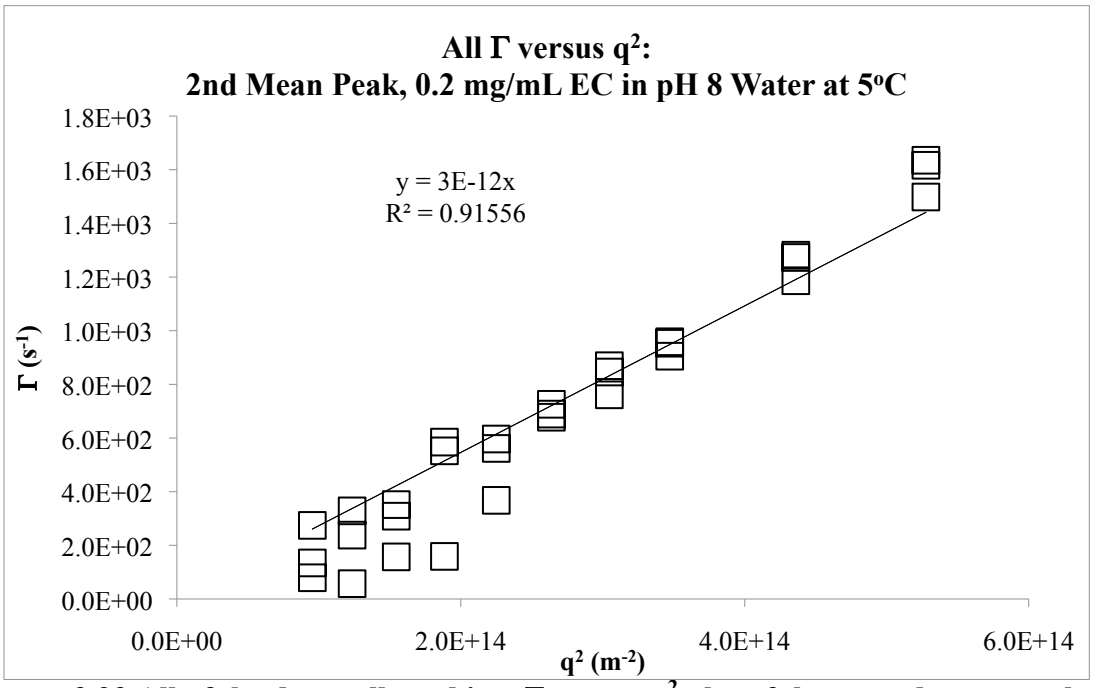


**Figure 3.23 All of the data collected in a Γ versus $q^2$ plot of the second mean peak of 0.2 mg/mL EC in pH 8 water at 5°C.**

At the transition temperature of 25°C the $R^2$ values derived from both methods of analysis were above 0.98, indicating a high degree of accuracy associated with the reported size-scale. The hydrodynamic radius was 78 nm.

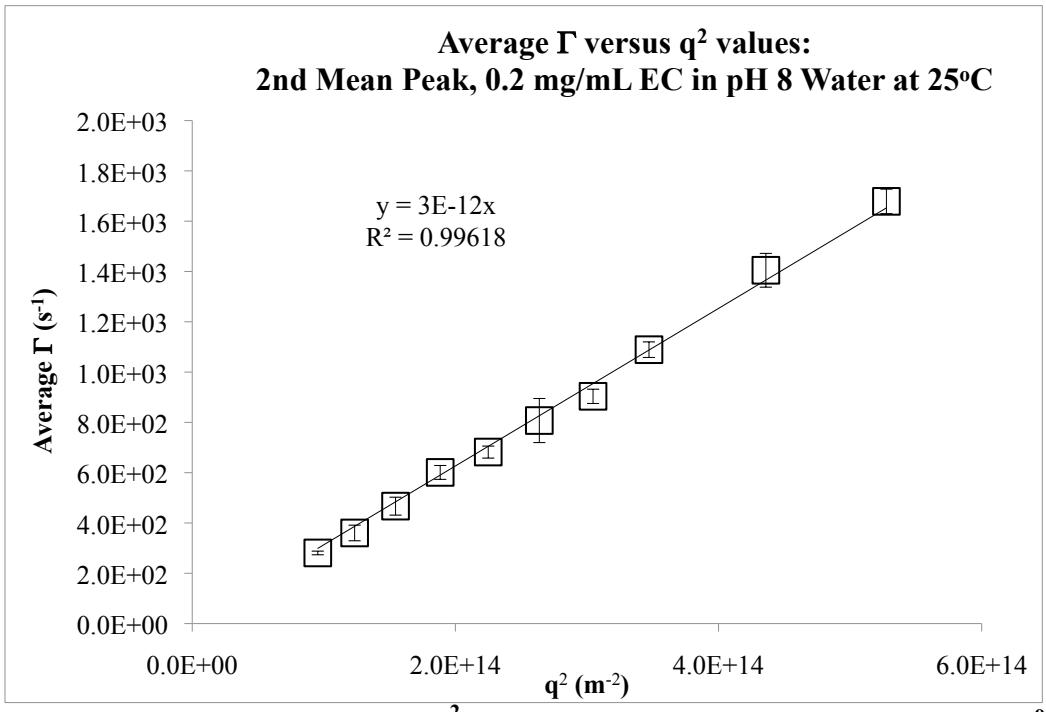


**Figure 3.24 The average Γ versus $q^2$ plot of 0.2 mg/mL EC in pH 8 water at 25°C.**

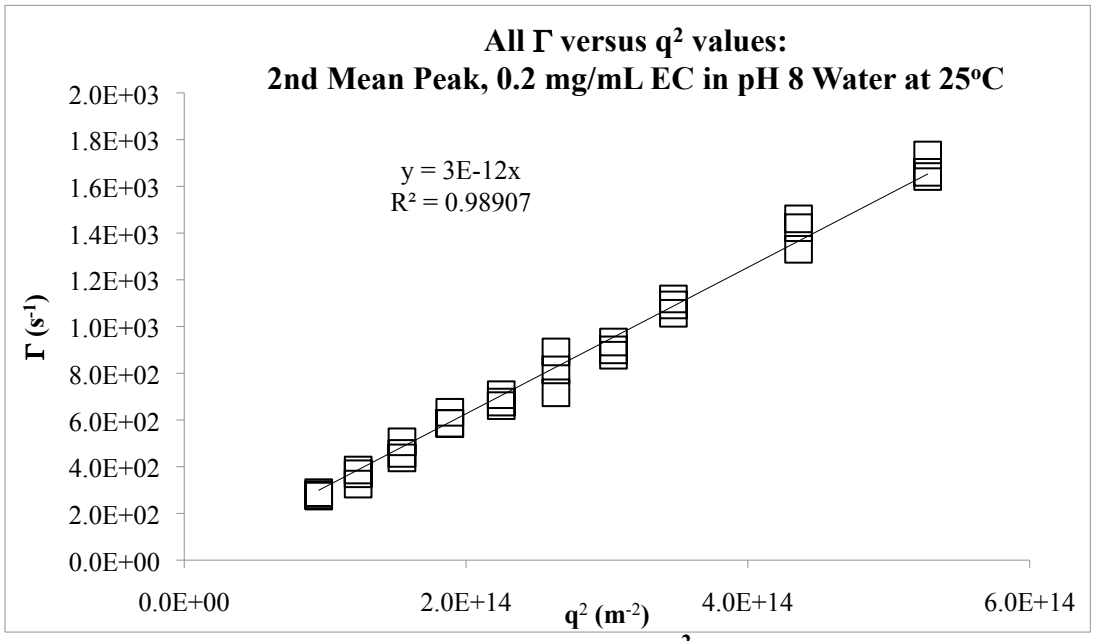


**Figure 3.25 All of the data collected in a Γ versus $q^2$ plot of 0.2 mg/mL EC in pH 8 water at 25°C.**

Below the transition temperature the micelle hydrodynamic radius of EC changed from 83.0 nm to 61.0 nm at 5°C and 20°C, respectively. The fast mode had a hydrodynamic radius of 4.0 nm at all temperatures studied below the transition temperature.

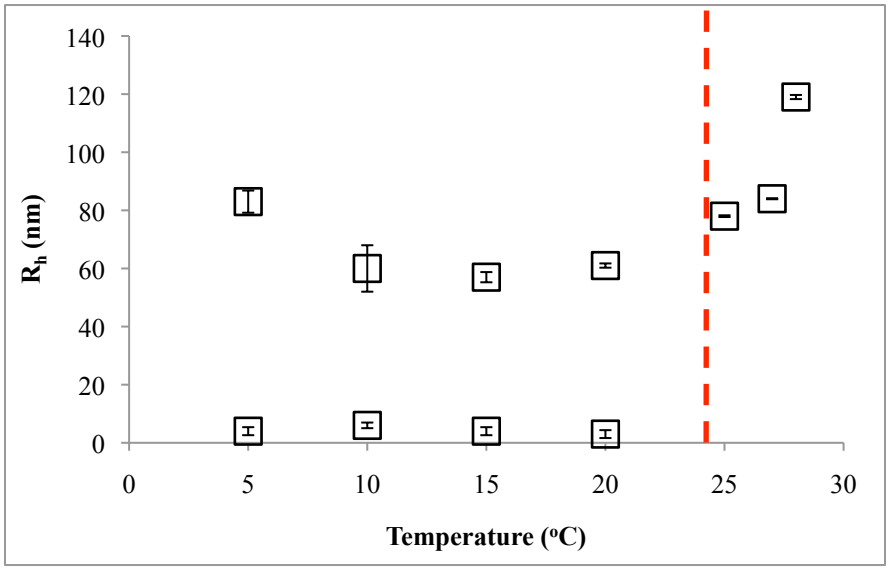


**Figure 3.26 A graph of the hydrodynamic radius, $R_h$, versus the temperature of 0.2 mg/mL EC at pH 8 deionized water. The transition temperature is marked with a dashed line at 25°C.**

One significant difference between ECE and EC is that EC exhibited spinodal decomposition above the transition temperature. Spinodal decomposition occurs when a system is brought into a thermodynamically unstable state. In this case that would be defined as having the system above the LCST binodal curve. The thermodynamic instability in the system results in concentration fluctuations that grow in amplitude and wavelength. The occurrence of spinodal decomposition was confirmed by SALS data that demonstrated an increase in an intensity peak with time. Spinodal decomposition indicated that the micelles were aggregating.[5]

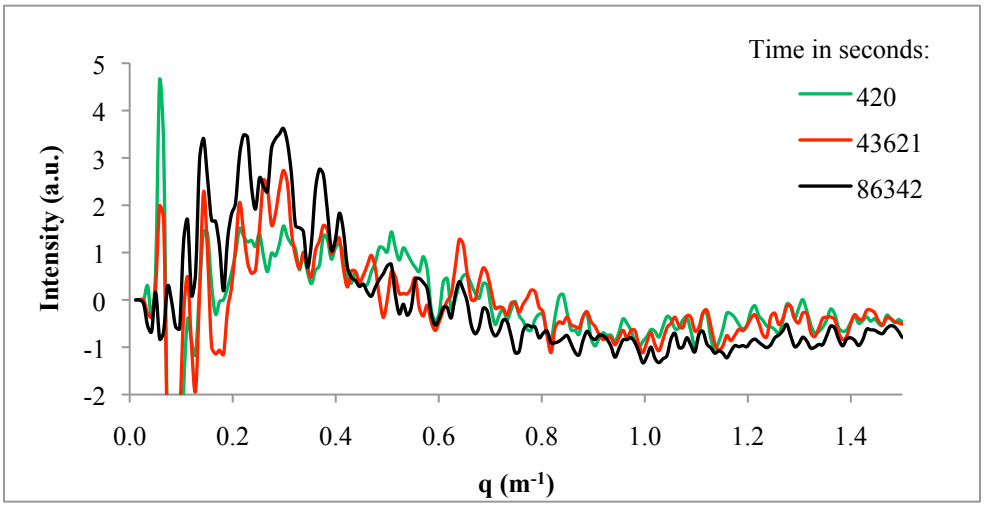


**Figure 3.27 EC demonstrated evidence of spinodal decomposition, which can be seen from this SALS data taken from a sample of 0.2 mg/mL EC in pH8 water at 25°C. Spinodal decomposition is suggested by the increase in the intensity peak with time.**

### 3.4.3 Analysis of CE Diblock

The behavior of CE was significantly different than both ECE and EC. CE was found to have a transition temperature of 15°C, which is lower than the transition temperatures of ECE and EC. According to the DLS data, three dominant size-scales were present in CE solutions below the transition temperature and four were found to exist above the transition temperature. One similarity that CE had to EC was the occurrence of spinodal decomposition.

A comparison of the normalized intensity correlation function below, at and above the transition temperature aids in understanding the data collected. Below the transition temperature the curves were rough at the highest y-axis value, however in an acceptable amount for data analysis. The smoothness of the curves is often improved through increasing the data collection time. It is acceptable to have the curve be rough at a y-axis

value close to one. The goal in data collection is to achieve smoothness at a y-axis value of zero.

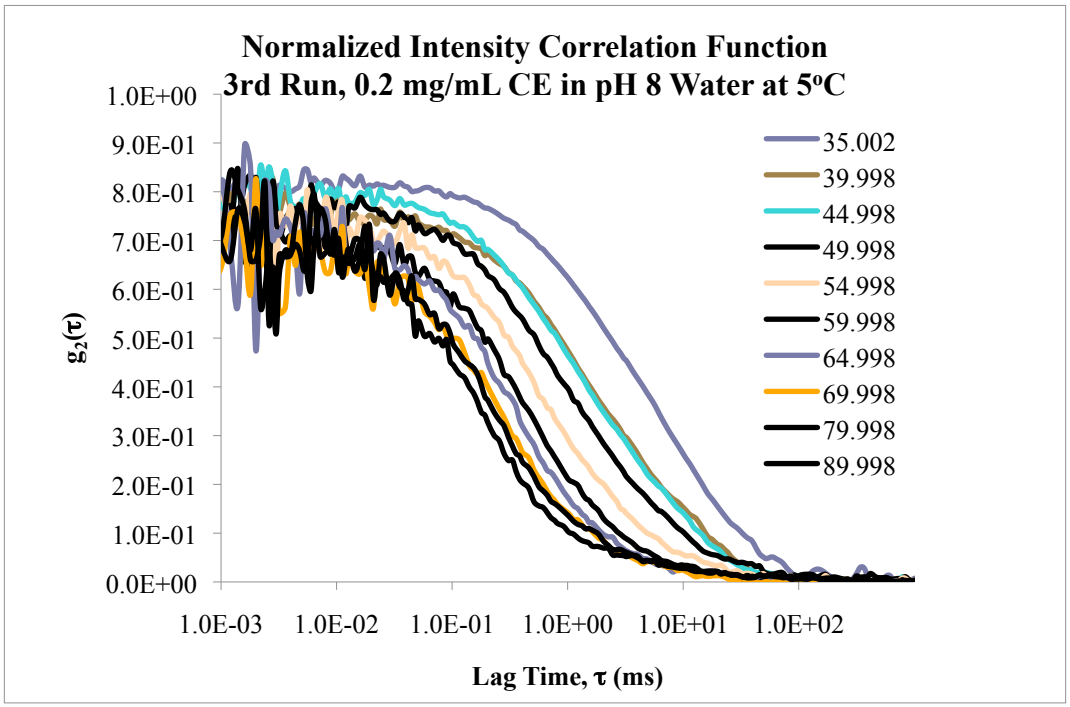


**Figure 3.28 A typical normalized intensity correlation function below the transition temperature of 0.2 mg/mL CE in pH 8 water.**

At the transition temperature the normalized intensity correlation function was also rough. There appears to be some irregularities in the pattern of how the curves shift with respect to angle. However, the irregularities are subtle and data analysis is still possible.

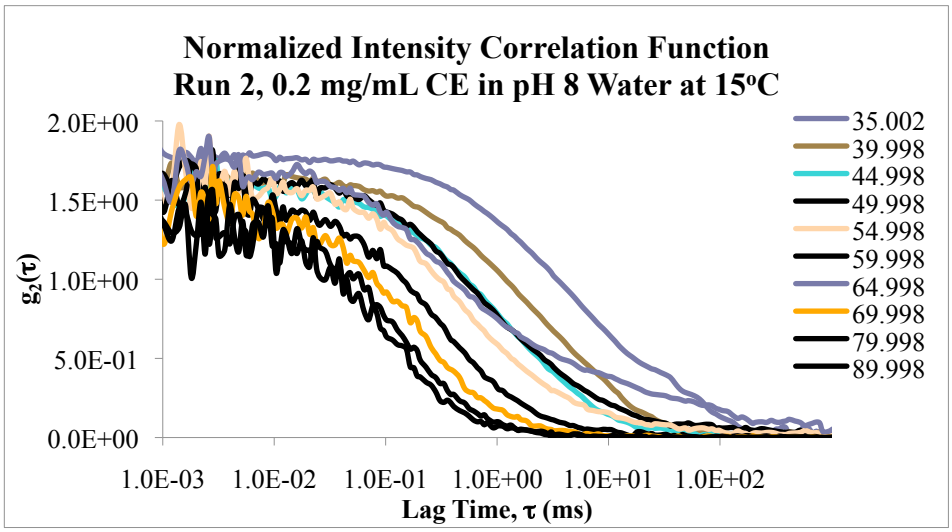


**Figure 3.29 A normalized intensity correlation function at the transition temperature of 0.2 mg/mL CE in pH 8 water.**

The normalized intensity correlation functions above the transition temperature were considerably more erratic than below the transition temperature. The irregular curves were most likely due to spinodal decomposition. The aggregates changed in size on the time-scale of the experiment resulting in shifted curves.

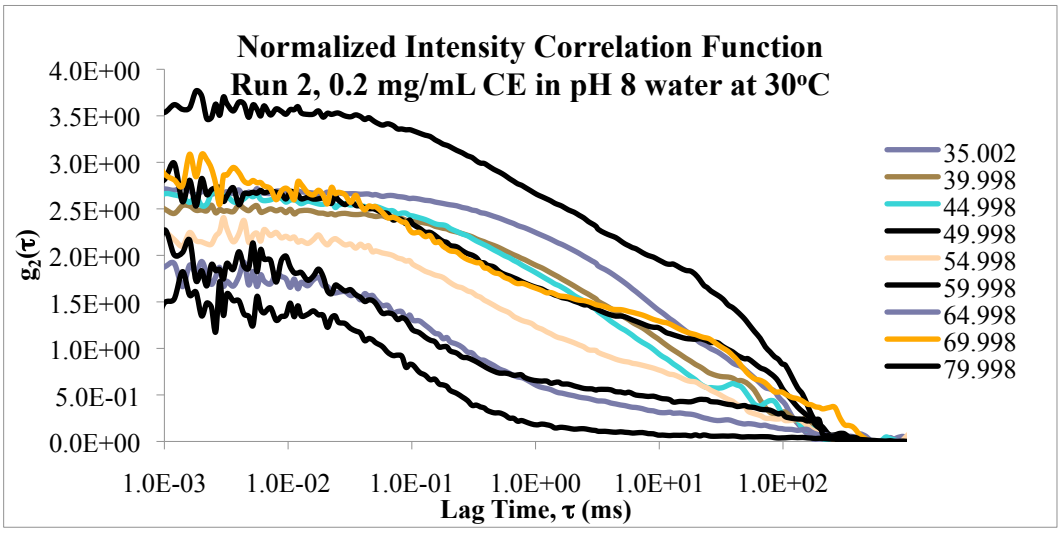


**Figure 3.30 A typical normalized intensity correlation function above the transition temperature of 0.2 mg/mL CE in pH 8 water.**

The probability distribution functions below and at the transition temperature differ in the number of modes present. There were three modes below the transition temperature and four modes above. Due to the presence of so many size scales the peaks often overlapped. When the modes overlapped it became difficult to determine the x-axis value corresponding to the peak. Origin's Laurentzian fit program was used to calculate the most probable peak positions. On a few occasions the modes lined up such that they were separately defined, that is how the conclusion was drawn that there were four peaks below and three peaks above the transition temperature.

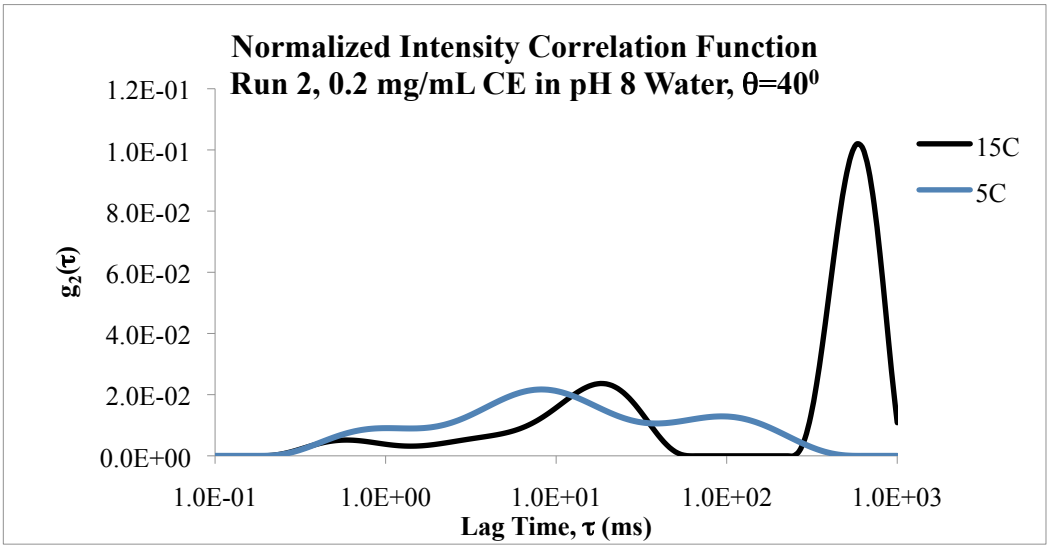


**Figure 3.31 A comparison of the probability distribution functions below and at the transition temperature of 0.2 mg/mL CE in pH 8 water. The goniometer was set at $40^{o}$ for both measurements.**

Most of the modes represented size-scales beyond the range of DLS and therefore could not be analyzed. The reliable hydrodynamic radius values that were determined did not follow a trend below or above the transition temperature.

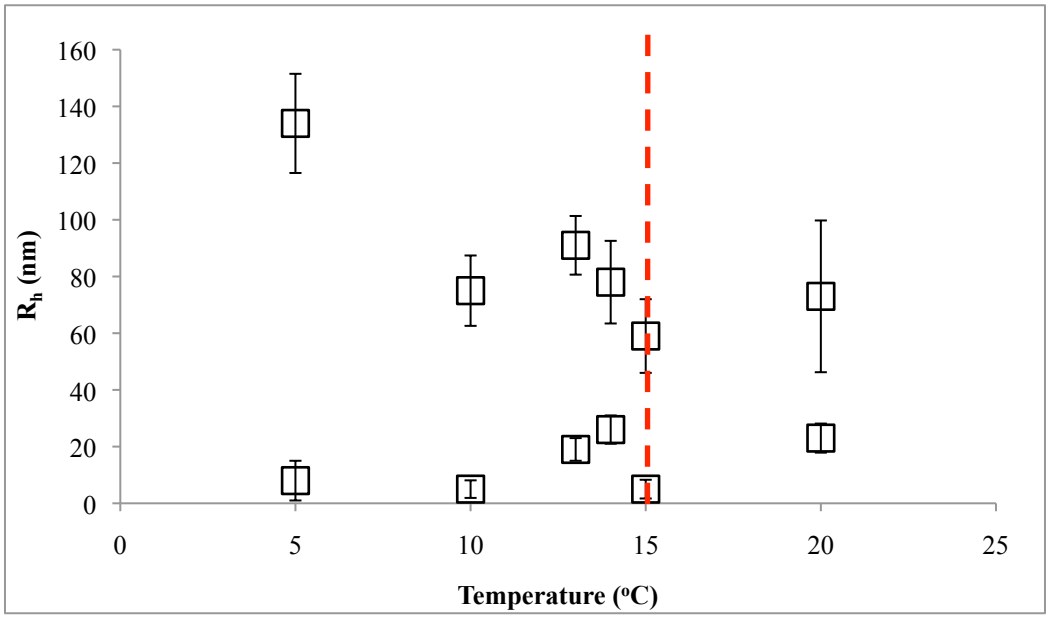


**Figure 3.32 A graph showing the two analyzable size-scales produced by 0.2 mg/mL CE in pH8 water using DLS.**

The Γ versus $q^2$ data below and at the transition temperature was analyzed with the two methods described in previous sections. Below the transition temperature only two size-scales resulted in reportable data within the range of DLS. The first mean peak at 5°C corresponded to a value of 34 nm. Both the average and all of the data have reasonable $R^2$ distribution fits indicating that the size reported is reliable.

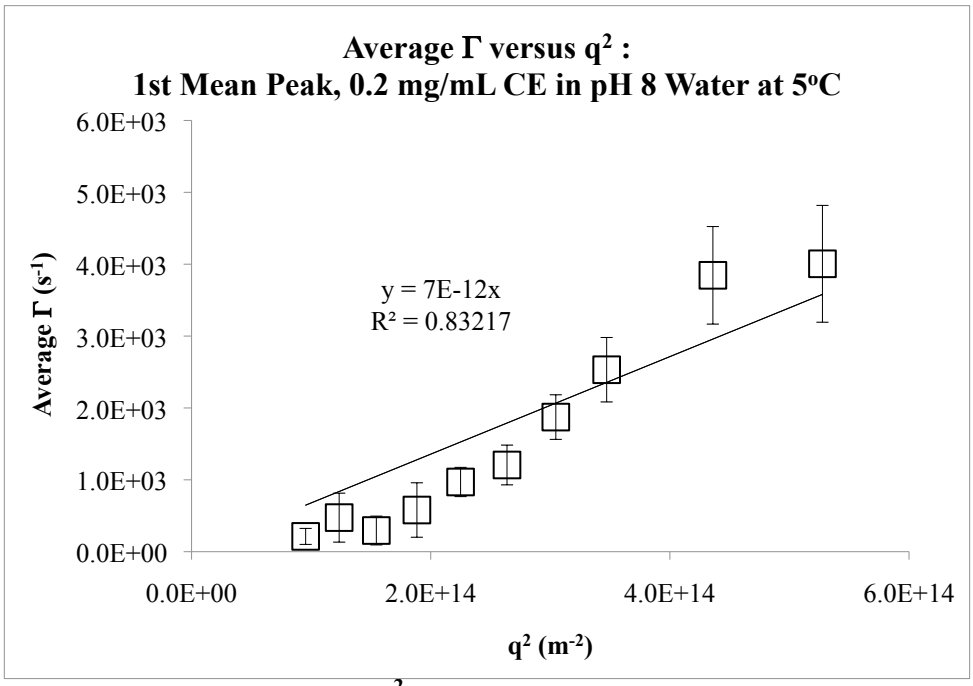


**Figure 3.33 The average Γ versus $q^2$ data of the first mean peak of 0.2 mg/mL CE in pH 8 water at 5°C.**

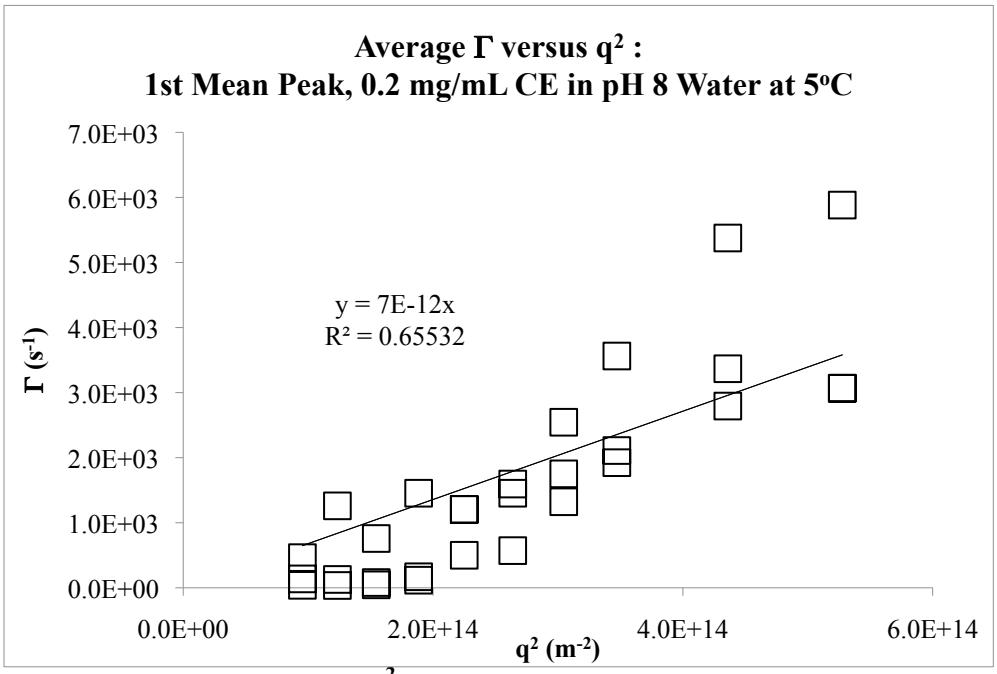


**Figure 3.34 All of the Γ versus $q^2$ data of the first mean peak of 0.2 mg/mL CE in pH 8 water at 5°C.**

The second mean peak produced at 5°C had a lower fit than the first mean peak. Part of the reason for the lower fit is the overlapping of the peaks in the probability distribution function. The fit values for the average and all of the data methods were 0.68 and 0.40, respectively. These low fit values associate a high degree of error to the reported size-scale of 180 nm.

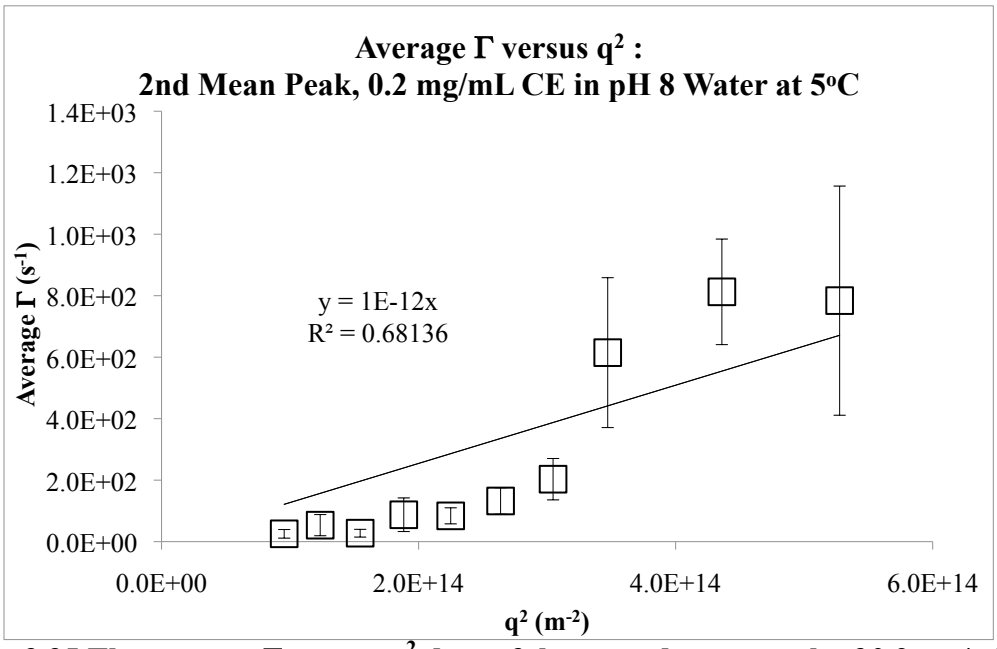


**Figure 3.35 The average Γ versus $q^2$ data of the second mean peak of 0.2 mg/mL CE in pH 8 water at 5°C.**

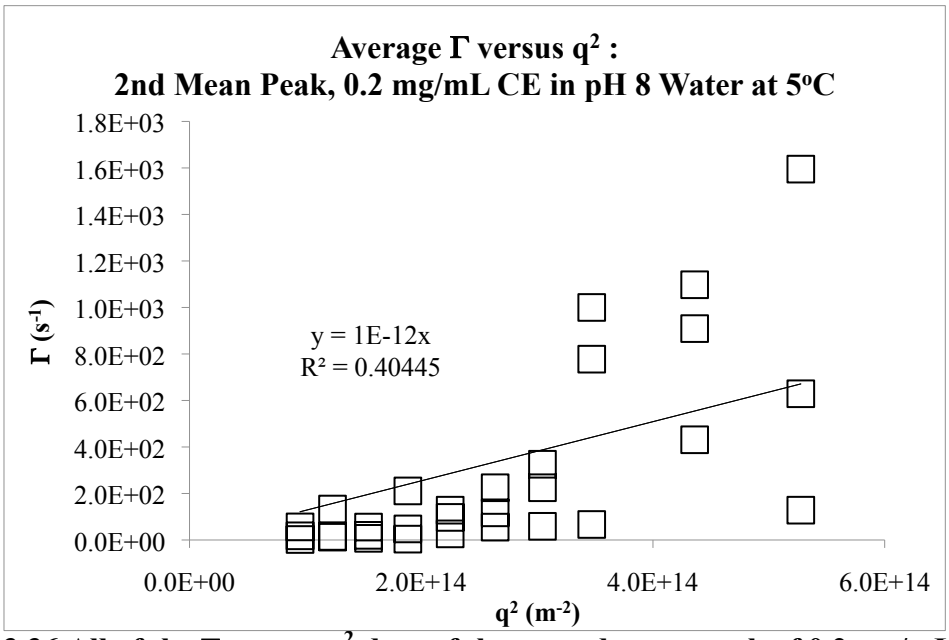


**Figure 3.36 All of the Γ versus $q^2$ data of the second mean peak of 0.2 mg/mL CE in pH 8 water at 5°C.**

At the transition temperature there were two mean peaks that were analyzable with DLS. The first mean peak corresponded to a hydrodynamic radius of 28 nm. Both methods of analyzing the Γ versus $q^2$ data produced high fits indicating that the reported size-scale is reliable.

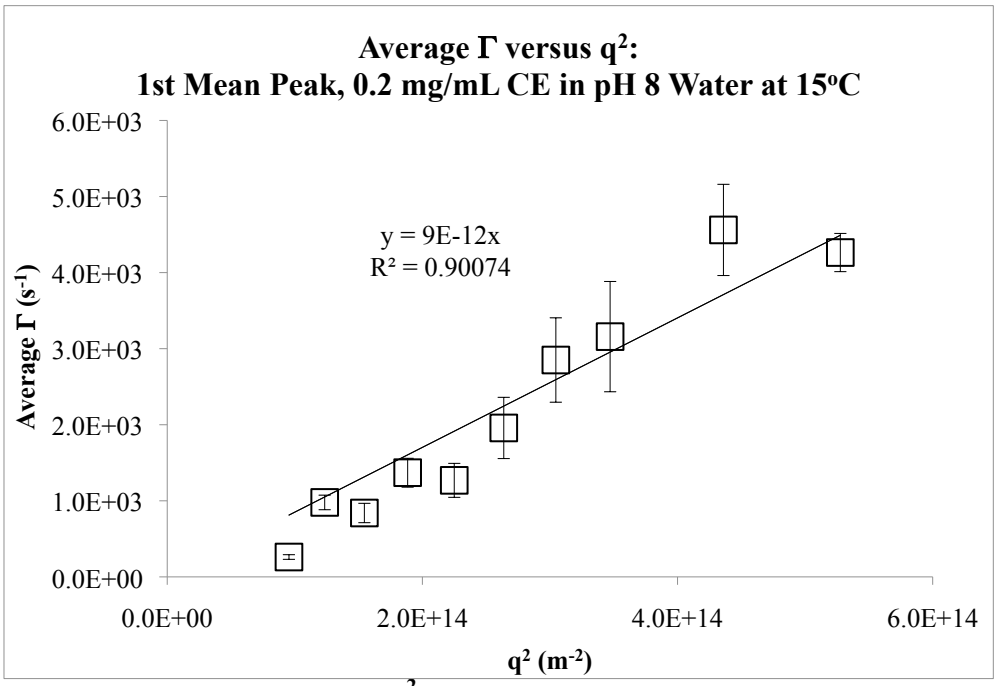


**Figure 3.37 The average Γ versus $q^2$ data of the first mean peak of 0.2 mg/mL CE in pH 8 water at 15°C.**

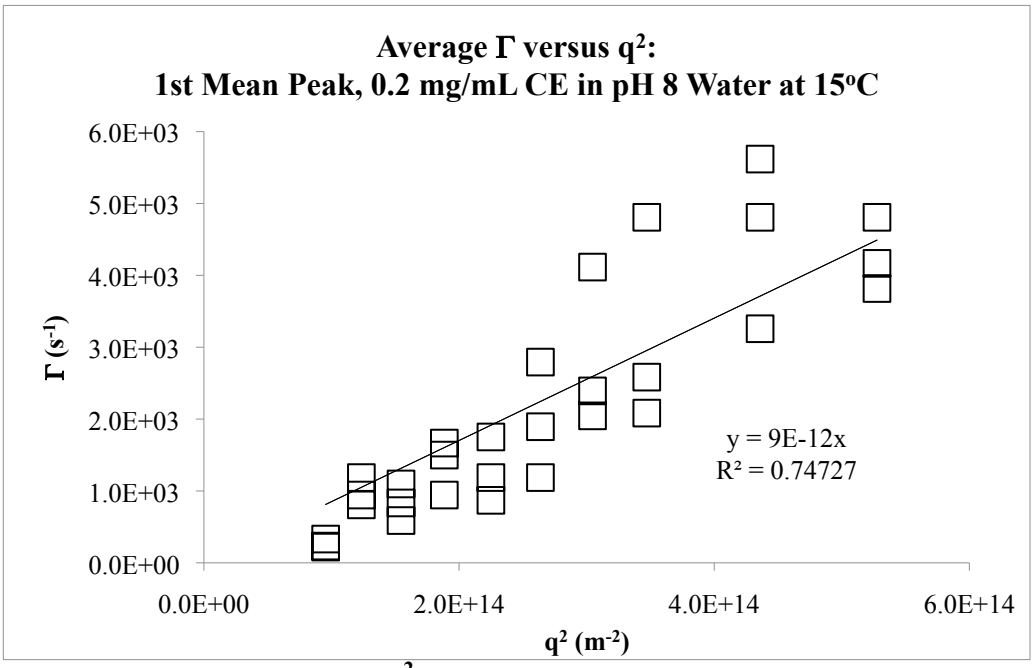


**Figure 3.38 All of the Γ versus $q^2$ data of the first mean peak of 0.2 mg/mL CE in pH 8 water at 15°C.**

The second mean peak had a high $R^2$ value for the average method, however when all of the data was plotted the $R^2$ value was significantly lower. This discrepancy is due to an erratic distribution at higher angles. At lower angles the data was repeatable.

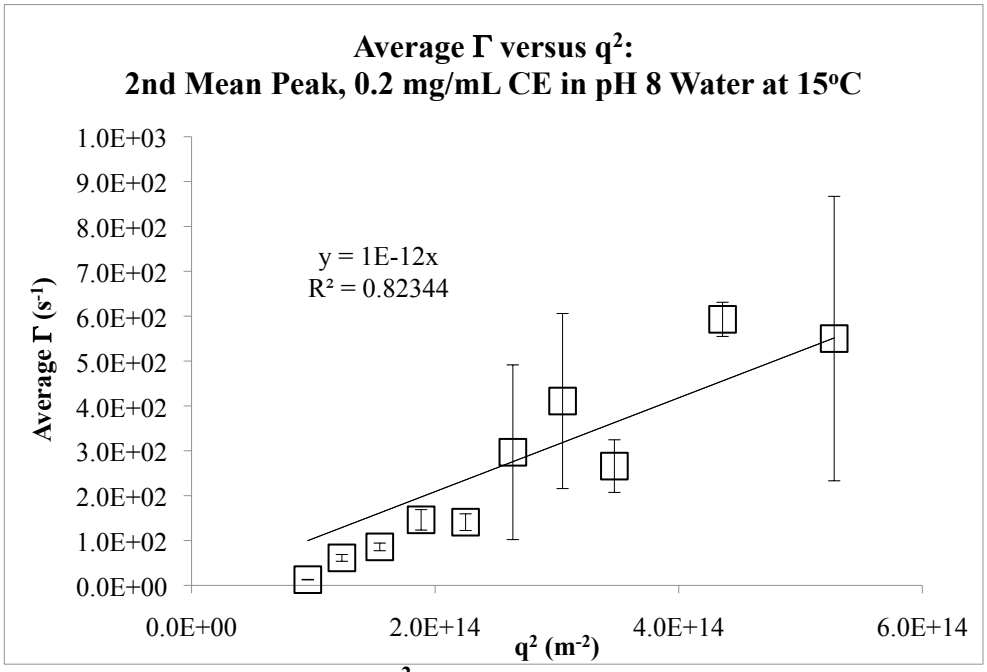


**Figure 3.39 The average Γ versus $q^2$ data of the second mean peak of 0.2 mg/mL CE in pH 8 water at 15°C.**

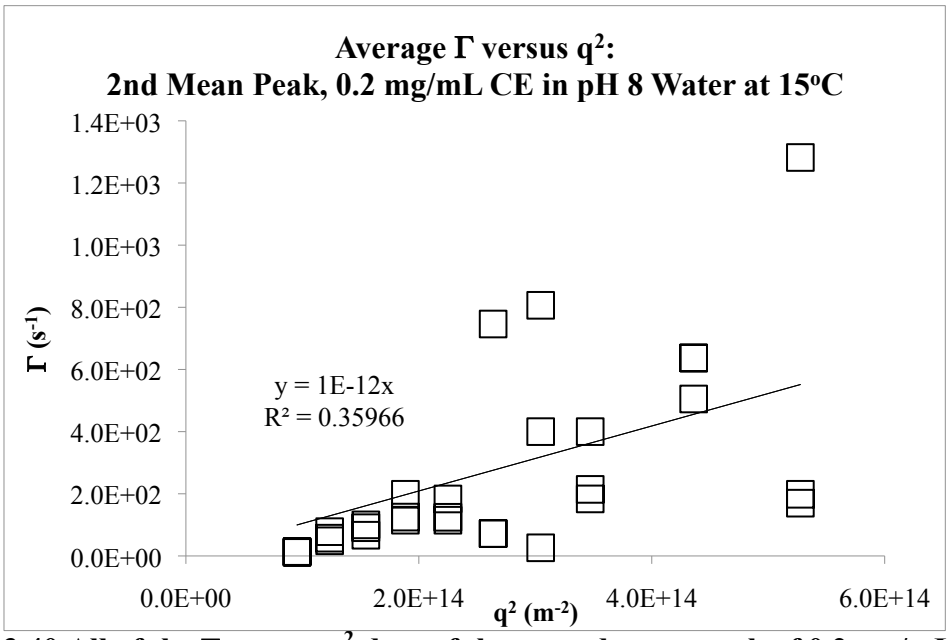


**Figure 3.40 All of the Γ versus $q^2$ data of the second mean peak of 0.2 mg/mL CE in pH 8 water at 15°C.**

CE, like EC, also exhibited spinodal decomposition above the transition temperature. SALS data confirmed that spinodal decomposition occurred. The change in peak intensity was very drastic with time, when compared to EC.

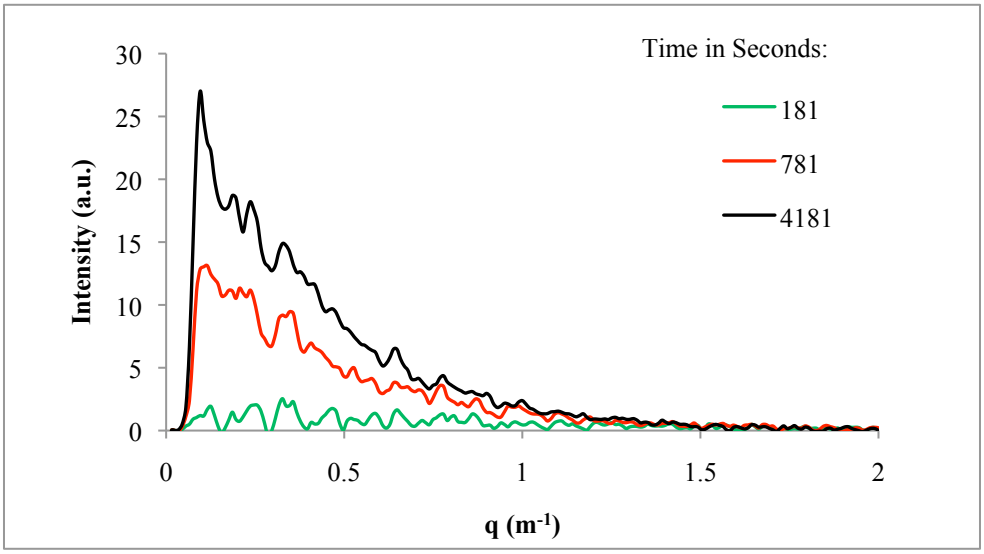


**Figure 3.41 SALS data of 0.2 mg/mL CE in pH 8 water indicating spinodal decomposition.**

The data produced by CE was, generally speaking, much more erratic than the data produced by EC and ECE. Both EC and ECE exhibited predictable trends, however CE did not. The only similarity CE shared was spinodal decomposition. Although CE and EC appear to be identical in sequence, the linkers used were different. The difference in linker groups is most likely part of the reason for the different behaviors exhibited by the different copolymers.

### 3.5 Conclusions

The significant difference in data trends between CE and the other two samples led to an investigation into the sequence and linkers used for each sample. The β-spiral elastin and COMPcc were bound together by linkers, therefore analysis was required not only of the proteins but the linkers. Highlighting the positively charged, negatively charged and hydrophobic amino acids aided in understanding the aggregation patterns. β-spiral elastin proved to be predominantly hydrophobic.

VPGVGVPGVGVPGFGVPGVGVPGVGVPGVGVPGVGVPGFGVPGVGVPGVGVP
GVGVPGVGVPGFGVPGVGVPGVGVPGVGVPGVGVPGFGVPGVGVPGVGVPGV
GVPGVGVPGFGVPGVGVPGVGVP

**Figure 3.42 A sequence analysis of β-spiral elastin where the hydrophobic regions are highlighted in green.**

The sequence of COMPcc was also studied. However, unlike β-spiral elastin, COMPcc exhibited a distribution of charges and hydrophobic groups. β-spiral elastin was predominantly hydrophobic, however COMPcc was hydrophilic. The proteins are

discussed in simplified terms in order to be able to loosely apply copolymer theory. By imagining β-spiral elastin as a hydrophobic block and COMPcc as a hydrophilic block the aggregation assembly can be visualized to assemble into micellar-like structures.

**DLA**PQ**ML**R**E**L**Q**E**TN**AAL**Q**D**V**R**E**LL**R**QQ**V**K**E**I**T**F**L**K**NT**V**M**E**S**D**A**SG

**Figure 3.43 A sequence analysis of COMPcc where the hydrophobic regions are highlighted in green, the positively charged amino acids are red, and the negatively charged amino acids are blue.**

To explain the differences in aggregation between CE and the other two protein copolymers, the linkers were analyzed. In both ECE and EC the hydrophobic block was placed next to a highly positively charged linker. Conversely, CE had the hydrophilic block placed next to the positively charged linker. This difference is responsible for the aggregation assembly. Both EC and ECE had at least three separate regions with alternating phobicity due to the linker. Three is an important number because it allows for the proteins to bend into hairpins and form micelles. CE only had two regions of alternating phobicity, therefore it did not form a micelle.

Positively Charged Side Chain: **R H K**
Negatively Charged Side Chain: **D E**
Hydrophobic Side Chain: **A I L M F W Y V**

ECE:
MRGSHHHHHHGSKPIAASA-
VPGVGVPGVGVPGFGVPGVGVPGVGVPGVGVPGVGVPGFGVPGVGVPGVGVP
GVGVPGVGVPGFGVPGVGVPGVGVPGVGVPGVGVPGFGVPGVGVPGVGVPGV
GVPGVGVPGFGVPGVGVPGVGVP-LEGSELAATATATATATATAACG-
DLAPQMLRELQETNAALQDVRELLRQQVKEITFLKNTVMESDASG-
LQAATATATATATATAVDKPIAASA-
VPGVGVPGVGVPGFGVPGVGVPGVGVPGVGVPGVGVPGFGVPGVGVPGVGVP
GVGVPGVGVPGFGVPGVGVPGVGVPGVGVPGVGVPGFGVPGVGVPGVGVPGV
GVPGVGVPGFGVPGVGVPGVGVP-LEGSGTGAKLN

EC:
MRGSHHHHHHGSKPIAASA-
VPGVGVPGVGVPGFGVPGVGVPGVGVPGVGVPGVGVPGFGVPGVGVPGVGVP
GVGVPGVGVPGFGVPGVGVPGVGVPGVGVPGVGVPGFGVPGVGVPGVGVPGV
GVPGVGVPGFGVPGVGVPGVGVP-LEGSELAATATATATATATAACG-
DLAPQMLRELQETNAALQDVRELLRQQVKEITFLKNTVMESDASG-
LQAATATATATATATAVDLQPS

CE:
MRGSHHHHHHGSACELAATATATATATATAACG-
DLAPQMLRELQETNAALQDVRELLRQQVKEITFLKNTVMESDASG-
LQAATATATATATATAVDKPIAASA-
VPGVGVPGVGVPGFGVPGVGVPGVGVPGVGVPGVGVPGFGVPGVGVPGVGVP
GVGVPGVGVPGFGVPGVGVPGVGVPGVGVPGVGVPGFGVPGVGVPGVGVPGV
GVPGVGVPGFGVPGVGVPGVGVP-LEGSGTGAKLN

**Figure 3.44 A sequence analysis of ECE, EC and CE where alternating regions of phobicity are highlighted in yellow.**

Three different arrangements of β-spiral elastin and COMPcc were studied with DLS and SALS. By analyzing the temperature-dependent behavior of these samples it was determined that the macroscopic assembly could be manipulated by changing the number and arrangement of the proteins. The goal of this project was to control the assembly of

the aggregate structure so that in the future the copolymers can be used as drug delivery systems.

### 3.6 Future Work

Jin Montclare's research group is in the process of synthesizing CEC. A clear next step would be to analyze that triblock with DLS. It would be interesting to see if CEC mimics the results of CE or ECE and EC. In other words, the question to answer is whether or not CEC demonstrate two modes below the transition temperature and one mode above. CEC has three regions of alternating phobicity, therefore I predict that CEC will form micelles and mimic the behavior of EC and ECE.

CEC:
MRGSHHHHHHGSACELAATATATATATATAACG-
DLAPQMLRELQETNAALQDVRELLRQQVKEITFLKNTVMESDASG-
LQAATATATATATATAVDKPIAASA-
VPGVGVPGVGVPGFGVPGVGVPGVGVPGVGVPGVGVPGFGVPGVGVPGVGVP
GVGVPGVGVPGFGVPGVGVPGVGVPGVGVPGVGVPGFGVPGVGVPGVGVPGV
GVPGVGVPGFGVPGVGVPGVGVP-LEGSGTG-
DLAPQMLRELQETNAALQDVRELLRQQVKEITFLKNTVMESDASG-LQASLIS

**Figure 3.45 A sequence analysis of CEC where alternating regions of phobicity are highlighted in yellow.**

One aspect of this project that could use further analysis is the inconsistency of end-groups and linkers on the proteins. Because the length of the end-groups and linkers between the proteins are on the order of one-half to one-third the length of the proteins themselves, they could impact the properties significantly.

# CHAPTER 4

# POLYELECTROLYTE COMPLEXATION

## 4.1 Introduction

The final project is in the inception phase and it will investigate the role of electrostatics in the aggregations mechanics of a polymer system containing a charged polymer. The two polymers are sodium polystyrene sulfonate (NaPSS) and the triblock polyethylene oxide - polypropylene oxide - polyethylene oxide (PEO-PPO-PEO). This project is of interest due to the tunability of the polymers through the molecular weight and polydispersity index, which is in contrast to the proteins studied in the other projects.

Block copolymers that form micelles are known to follow the model of closed association.[62-64] This model asserts that there is a concentration region at which isolated chains and micelles exist in equilibrium. Below that concentration only isolated chains exist and above that concentration only micelles exist.[64]

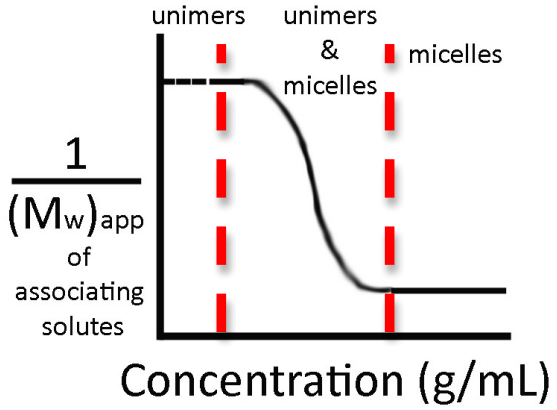


**Figure 4.1 The theoretical graph for a micellar system that follows closed association.**

In order for the data acquisition to be successful the transition from isolated chains to micelle must occur at a concentration range that is analyzable with light scattering. This means that the critical micelle concentration (CMC) must be less than the overlap concentration (c*).

Preliminary experiments are being performed on PEO-PPO-PEO and sodium polystyrene sulfonate to characterize their individual properties. Dilute solutions of PEO-PPO-PEO in water have been shown to form micelles.[65-68] Using DLS analysis, the individual polymers and micelles comprise a fast and slow mode, respectively.[13] NaPSS also forms a fast and slow mode.[5] However, NaPSS is a polyelectrolyte, whereas PEO-PPO-PEO is not.

It has been established in literature that the addition of an electrolyte to a system that forms micelles shifts the critical micelle temperature (CMT) to a lower value.[69, 70] In order to ensure that the transition from isolated chains to micelles can be captured using DLS, precautions will have to be taken to maximize the CMT and CMC.

By tuning concentration, pH, salt, and hydrophobic block length of two individually self-assembling polymers, (one of which is a polyelectrolyte,) the macrostructure, CMC and CMT can be controlled.[60, 71] This project is the natural next step after the previous two projects due to the tunability of the polymers being used. These polymers can be controlled by altering the polydispersity index, molecular weight and concentration.

Further, the placement and concentration of functional groups along these polymers will be well established unlike the proteins used in the first two studies.

### 4.2 Materials and Methods

Both sodium polystyrene sulfonate (NaPSS) and PEO-PPO-PEO can form fast and slow modes in water when individually solvated as homopolymers. Therefore, the goal of the first set of experiments will be to characterize each polymer in solution by itself.

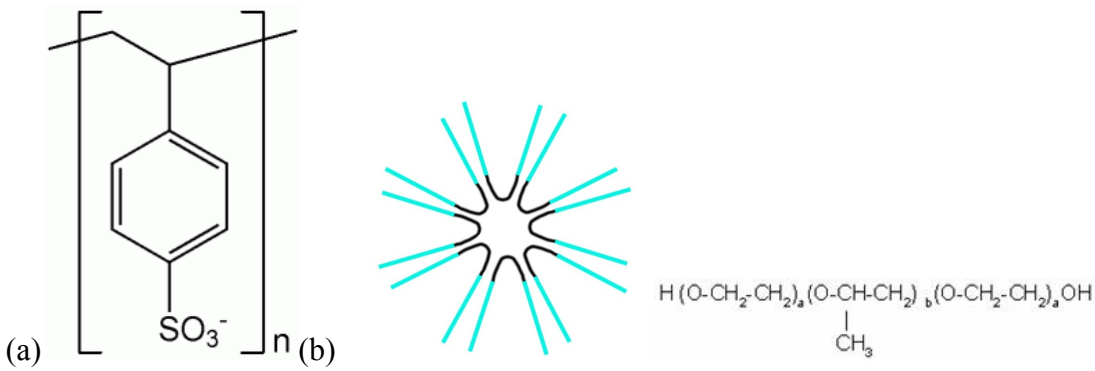


**Figure 4.2 An illustration of the structure of (a) NaPSS and (b) PEO-PPO-PEO in micelle form and the chemical structure.**

A paper by Brown *et* al. published in 1991 described a DLS analysis of PEO-PPO-PEO in water at a range of temperatures. The paper indicated that below the CMC, rather than getting one peak representing the individual polymer in solution, they saw multiple peaks due to impurities in the sample. The paper then asserted that above the CMC they saw two peaks, one represented the individual polymer in solution and the second peak represented the micelle. The disappearance of the other erratic peaks was attributed to the diblock impurities and other size-scales being contained within the micelles.[13]

In an effort to get one size-scale below the CMC, PEO-PPO-PEO with a polydispersity index (PDI) of 1.07 was ordered from Polymer Source (P6002-EOPOEO). This was the lowest PDI available, while still maintaining a polymer with a molecular weight comparable to the one used in the Brown paper.[13] The experiments in the Brown paper used a polymer of molecular weight ratio of 1.1-b-2.3-b-1.1, whereas 1.6-b-0.5-b-1.6 was purchased for the following experiments. The choice of a smaller hydrophobic block region was made in an effort to shift the CMC and CMT to higher values.[71]

Based on literature, it is important to consider three possible complex structures. A pearl necklace structure, where pluronic micelles decorate the NaPSS, is one potential configuration.[71] A different paper suggests the possibility of a hydrated PEO shell with NaPSS shielded at the interior.[72] A third complex structure to consider is a PEO shell, PPO core and NaPSS associates with the PEO through hydrogen bonding.[73]

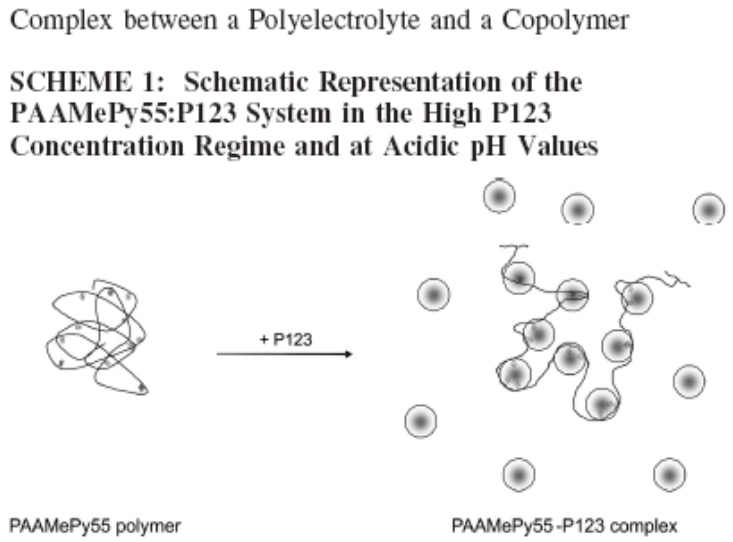


**Figure 4.3 Proposed pearl necklace structure between PAA and pluronic.[71]**

### 4.3 Preliminary Results

The general progression of this project will involve first characterizing NaPSS and PEO-PPO-PEO by themselves and then characterizing the complex. Because NaPSS is already well characterized in literature, and specifically by past group members of the Muthukumar Research Group, the logical place to start was in characterizing PEO-PPO-PEO.

The first set of experiments involved collecting DLS and SLS data at 10$^{o}$C and 25$^{o}$C with solution concentrations of 0.05 mg/mL, 0.1 mg/mL, 0.2 mg/mL, and 0.4 mg/mL. The choice of concentrations was to ensure that data acquisition occurred within the unimer region of the closed association model. All of these experiments were performed once with a filter and once without a filter. It is important to note the use of a filter in aggregation studies due to the possible interference with the achievement of equilibrium structures.

The Brown et al. paper also characterized PEO-PPO-PEO with DLS, however the lowest concentration studied was 1 wt%, which corresponds to 10 mg/mL of pluronic in water.[13] This value is significantly higher than all concentrations tested in the previously outlined experiments.

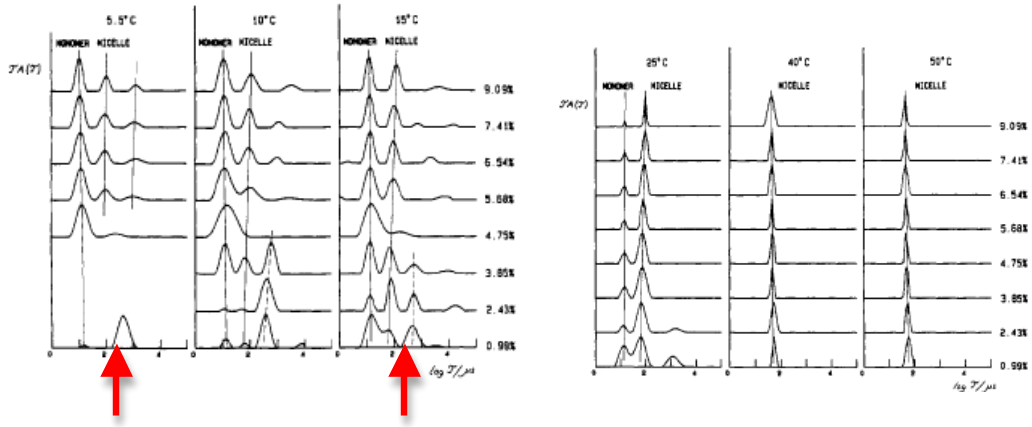


**Figure 4.4 Probability distribution function DLS data collected by Brown *et al.*[13]**

Data from the Brown paper is included above for comparison with data to be presented. Although the Brown paper asserts the formation of only unimers in solution at low concentrations, analysis of the probability distribution function indicates that is not true. The 0.99 wt% line is marked with red arrows where peaks occur to the right of the peak attributed to the micelle. For peaks to be occurring at larger lag times, size-scales larger than the micelle must be occurring. This data indicates that pluronic does not follow the model of closed association at low concentrations and my data supports this conclusion.

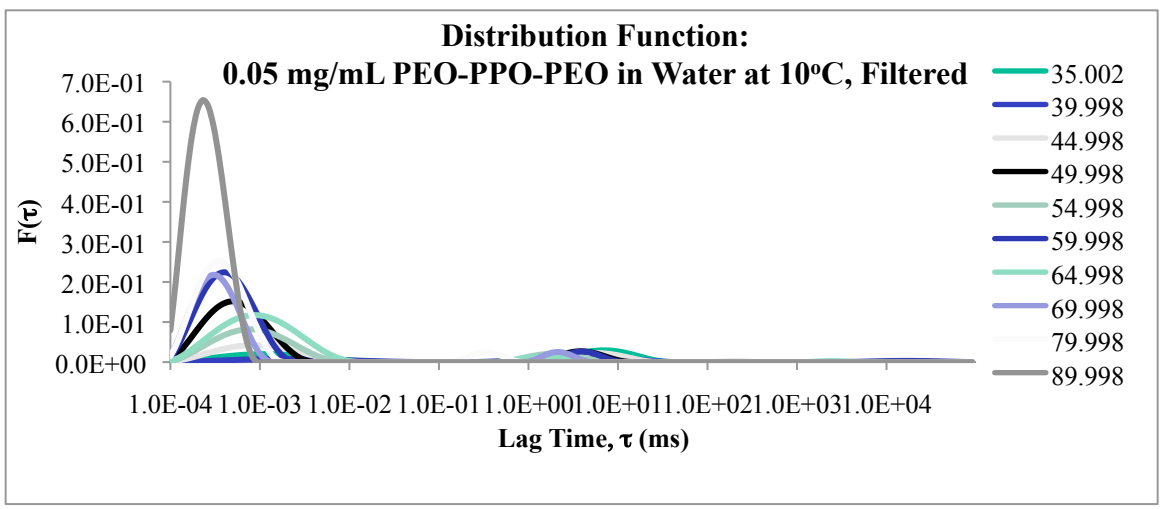


**Figure 4.5 A probability distribution function of pluronic showing a peak representative of a small and large size-scale.**

When analyzed, all of the filtered sample DLS data showed a second peak indicative of a large size-scale. Neither of the size-scales was reportable, which is most likely due to the low molecular weight analyzed. The correlation functions of the samples were very weak, and it is therefore likely that the low concentration combined with the low molecular weight made the data unreliable.

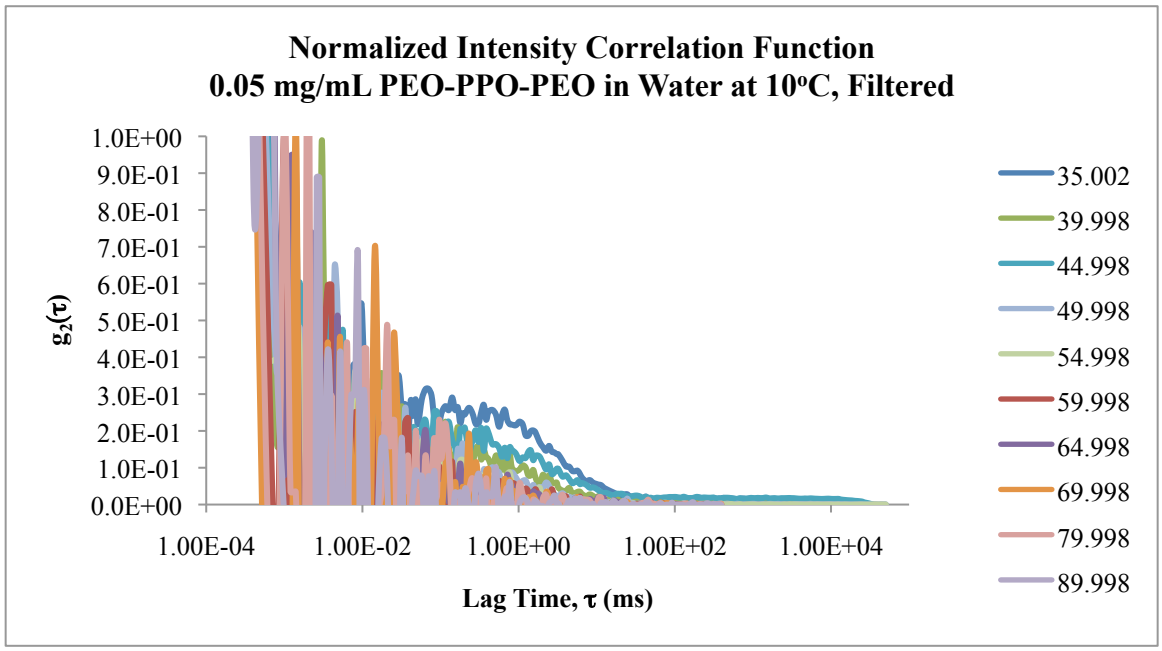


**Figure 4.6 The correlation functions of 0.05 mg/mL pluronic in water at 10°C.**

The correlation functions at a higher concentration of 0.1 mg/mL were even less pronounced, thus indicating that better preparation methods and/or a higher molecular weight sample needs to be used. The current light scattering apparatus is not in a clean room setting. Nor are the samples prepared in a clean room or sealed hood. Making changes to improve the sample quality will allow for lower concentration regimes to be explored accurately.

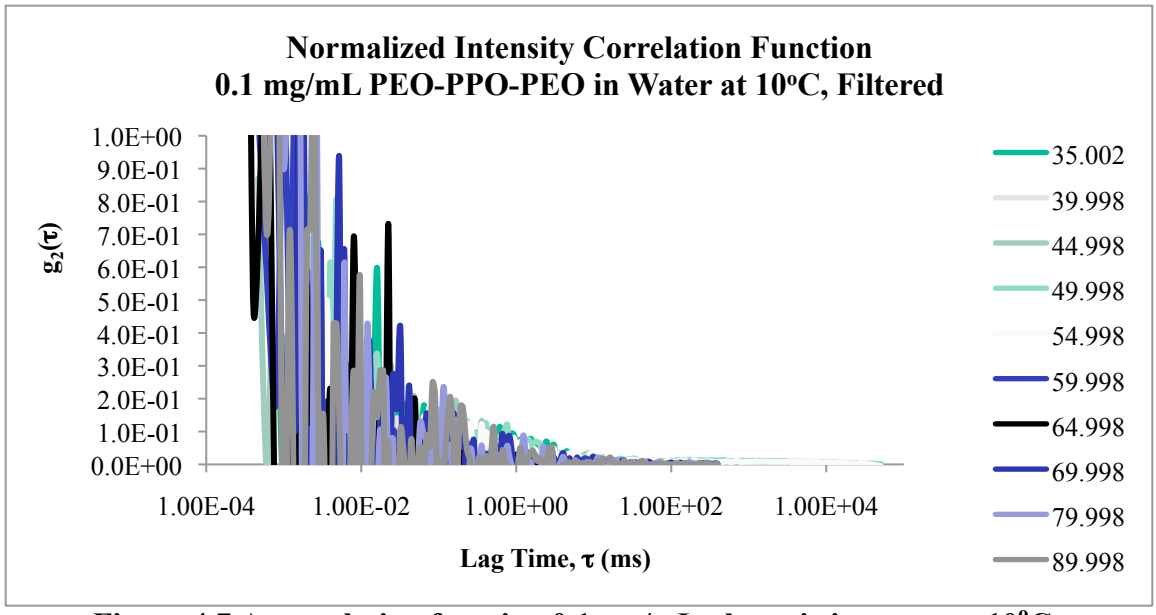


**Figure 4.7 A correlation function 0.1 mg/mL pluronic in water at 10°C.**

### 4.4 Future Work

The next series of experiments will need to investigate pluronic at a higher molecular weight. It would also be valuable to perform these experiments in a more secure clean room setting, due to the low concentrations being analyzed.

Future experiments for this project include studying the aggregation mechanics of PEO-PPO-PEO and other polyelectrolytes. Different polyelectrolytes can be selected dependent upon the pKa of their functional groups. By choosing a polyelectrolyte with a functional group that becomes charged only beyond an experimentally achievable pH, the importance of electrostatics versus charge neutral interactions can be explored.

## BIBLIOGRAPHY


1. Muthukumar, M., C.K. Ober, and E.L. Thomas, *Competing interactions and levels of ordering in self-organizing polymeric materials.* Science, 1997. **277**(5330): p. 1225-1232.
2. Chang, S.Y. and H. Morawetz, *POLYMER ASSOCIATION .3. MOLECULAR AGGREGATION AND INTRAMOLECULAR GROUP ASSOCIATION IN DILUTE SOLUTIONS OF STYRENE-METHACRYLIC ACID COPOLYMERS.* Journal of Physical Chemistry, 1956. **60**(6): p. 782-786.
3. Pappu, R.V., et al., *A polymer physics perspective on driving forces and mechanisms for protein aggregation.* Archives of Biochemistry and Biophysics, 2008. **469**(1): p. 132-141.
4. Berne, B.J. and R. Pecora, *Dynamic light scattering : with applications to chemistry, biology, and physics*. 1976, New York: Wiley. vii, 376 p.
5. Kanai, S. and M. Muthukumar, *Phase separation kinetics of polyelectrolyte solutions.* Journal of Chemical Physics, 2007. **127**(24): p. 14.
6. Walther, A., et al., *Multiple morphologies, phase transitions, and cross-linking of crew-cut aggregates of polybutadiene-block-poly(2-vinylpyridine) diblock copolymers.* Macromolecules, 2008. **41**(9): p. 3254-3260.
7. Benedek, G.B., *Cataract as a protein condensation disease - The Proctor Lecture.* Investigative Ophthalmology & Visual Science, 1997. **38**(10): p. 1911-1921.
8. Oyster, C.W., *The Human Eye: Structure and Function*. 1999, Sunderland, Mass: Sinauer Associates.
9. Ozbek, S., J. Engel, and J. Stetefeld, *Storage function of cartilage oligomeric matrix protein: the crystal structure of the coiled-coil domain in complex with vitamin D-3.* Embo Journal, 2002. **21**(22): p. 5960-5968.
10. Derham, B.K. and J.J. Harding, *alpha-crystallin as a molecular chaperone.* Progress in Retinal and Eye Research, 1999. **18**(4): p. 463-509.
11. Baker, P.J., J.S. Haghpanah, and J.K. Montclare, *Elastin-Based Protein Polymers*, in *Polymer Biocatalysis and Biomaterials Ii*, H.N. Cheng and R.A. Gross, Editors. 2008, Amer Chemical Soc: Washington. p. 37-51.
12. Urry, D.W., et al., *Elastin: a representative ideal protein elastomer.* Philosophical Transactions of the Royal Society of London Series B-Biological Sciences, 2002. **357**(1418): p. 169-184.
13. Brown, W., et al., *MICELLE AND GEL FORMATION IN A POLY(ETHYLENE OXIDE) POLY(PROPYLENE OXIDE) POLY(ETHYLENE OXIDE) TRIBLOCK COPOLYMER IN WATER SOLUTION - DYNAMIC AND STATIC LIGHT-SCATTERING AND OSCILLATORY SHEAR MEASUREMENTS.* Journal of Physical Chemistry, 1991. **95**(4): p. 1850-1858.
14. Bloemendal, H., et al., *Ageing and vision: structure, stability and function of lens crystallins.* Progress in Biophysics & Molecular Biology, 2004. **86**(3): p. 407-485.
15. Manning, G.S., *MOLECULAR THEORY OF POLYELECTROLYTE SOLUTIONS WITH APPLICATIONS TO ELECTROSTATIC PROPERTIES OF*

*POLYNUCLEOTIDES.* Quarterly Reviews of Biophysics, 1978. **11**(2): p. 179-246.
16. Srivastava, D. and M. Muthukumar, *INTERPENETRATION OF INTERACTING POLYELECTROLYTES.* Macromolecules, 1994. **27**(6): p. 1461-1465.
17. Prabhu, V.M., et al., *Polyelectrolyte chain dimensions and concentration fluctuations near phase boundaries.* Journal of Chemical Physics, 2003. **119**(7): p. 4085-4098.
18. Prabhu, V.M., et al., *Dimensions of polyelectrolyte chains and concentration fluctuations in semidilute solutions of sodium-poly (styrene sulfonate) as measured by small-angle neutron scattering.* Polymer, 2001. **42**(21): p. 8935-8946.
19. Sedlak, M. and E.J. Amis, *DYNAMICS OF MODERATELY CONCENTRATED SALT-FREE POLYELECTROLYTE SOLUTIONS - MOLECULAR-WEIGHT DEPENDENCE.* Journal of Chemical Physics, 1992. **96**(1): p. 817-825.
20. Kanai, S., *Phase Separation Kinetics of Polyelectrolyte Solutions*, in *Polymer Science & Engineering*. 2006, Univerisity of Massachusetts: Amherst. p. 113.
21. Jarrett, J.T., E.P. Berger, and P.T. Lansbury, *THE CARBOXY TERMINUS OF THE BETA-AMYLOID PROTEIN IS CRITICAL FOR THE SEEDING OF AMYLOID FORMATION - IMPLICATIONS FOR THE PATHOGENESIS OF ALZHEIMERS-DISEASE.* Biochemistry, 1993. **32**(18): p. 4693-4697.
22. Polymeropoulos, M.H., et al., *Mutation in the alpha-synuclein gene identified in families with Parkinson's disease.* Science, 1997. **276**(5321): p. 2045-2047.
23. Spector, A., *THE SEARCH FOR A SOLUTION TO SENILE CATARACTS PROCTOR LECTURE.* Investigative Ophthalmology & Visual Science, 1984. **25**(2): p. 130-146.
24. Benedek, G.B., *Theory of Transparency of Eye.* Applied Optics, 1971. **10**(3): p. 459-&.
25. Bloemendal, H., *VERTEBRATE EYE LENS.* Science, 1977. **197**(4299): p. 127-138.
26. Klein, B.E.K., R. Klein, and K.E. Lee, *Incidence of age-related cataract over a 10-year interval - The Beaver Dam Eye Study.* Ophthalmology, 2002. **109**(11): p. 2052-2057.
27. Truscott, R.J.W., *Age-related nuclear cataract - oxidation is the key.* Experimental Eye Research, 2005. **80**(5): p. 709-725.
28. Augusteyn, R.C. and A. Stevens, *Macromolecular structure of the eye lens.* Progress in Polymer Science, 1998. **23**(3): p. 375-413.
29. Augusteyn, R.C., *alpha-crystallin: a review of its structure and function.* Clin Exp Optom, 2004. **87**(6): p. 356-66.
30. Bindels, J.G., et al., *COMPARATIVE AND AGE-DEPENDENT ASPECTS OF CRYSTALLIN SIZE AND DISTRIBUTION IN HUMAN, RABBIT, BOVINE, RAT, CHICKEN, DUCK, FROG AND DOGFISH LENSES.* Comparative Biochemistry and Physiology B-Biochemistry & Molecular Biology, 1983. **76**(1): p. 47-55.
31. Lawson, E.Q., et al., *THE SOLUBILITY OF BOVINE LENS CRYSTALLINS.* Journal of Biological Chemistry, 1981. **256**(13): p. 6523-6525.
32. Bax, B., et al., *X-RAY-ANALYSIS OF BETA-B2-CRYSTALLIN AND EVOLUTION OF OLIGOMERIC LENS PROTEINS.* Nature, 1990. **347**(6295): p. 776-780.

33. Slingsby, C. and N.J. Clout, *Structure of the crystallins.* Eye, 1999. **13**: p. 395-402.
34. Groenen, P., et al., *STRUCTURE AND MODIFICATIONS OF THE JUNIOR CHAPERONE ALPHA-CRYSTALLIN - FROM LENS TRANSPARENCY TO MOLECULAR PATHOLOGY.* European Journal of Biochemistry, 1994. **225**(1): p. 1-19.
35. Horwitz, J., *ALPHA-CRYSTALLIN CAN FUNCTION AS A MOLECULAR CHAPERONE.* Proceedings of the National Academy of Sciences of the United States of America, 1992. **89**(21): p. 10449-10453.
36. Rao, P.V., et al., *Evidence that alpha-crystallin prevents non-specific protein aggregation in the intact eye lens.* Biochimica Et Biophysica Acta-General Subjects, 1995. **1245**(3): p. 439-447.
37. Raman, B. and C.M. Rao, *Chaperone-Like Activity and Quaternary Structure of Alpha-Crystallin.* Journal of Biological Chemistry, 1994. **269**(44): p. 27264-27268.
38. Khanova, H.A., et al., *Mechanism of chaperone-like activity. Suppression of thermal aggregation of beta(L)-crystallin by alpha-crystallin.* Biochemistry, 2005. **44**(47): p. 15480-15487.
39. Sun, Y. and T.H. MacRae, *The small heat shock proteins and their role in human disease.* Febs Journal, 2005. **272**(11): p. 2613-2627.
40. Sun, Y. and T.H. MacRae, *Small heat shock proteins: molecular structure and chaperone function.* Cellular and Molecular Life Sciences, 2005. **62**(21): p. 2460-2476.
41. Krivandin, A.V., K.O. Muranov, and M.A. Ostrovsky, *Studies of alpha- and beta(L)-crystallin complex formation in solution at 60 degrees C.* Molecular Biology, 2004. **38**(3): p. 447-458.
42. Kim, K.K., R. Kim, and S.H. Kim, *Crystal structure of a small heat-shock protein.* Nature, 1998. **394**(6693): p. 595-599.
43. Tricot, C., *Curves and fractal dimension*. 1995, New York: Springer-Verlag.
44. Burchard, W., *PARTICLE SCATTERING FACTORS OF SOME BRANCHED POLYMERS.* Macromolecules, 1977. **10**(5): p. 919-927.
45. Clackson, T. and J.A. Wells, *A HOT-SPOT OF BINDING-ENERGY IN A HORMONE-RECEPTOR INTERFACE.* Science, 1995. **267**(5196): p. 383-386.
46. Jin, L., F.E. Cohen, and J.A. Wells, *STRUCTURE FROM FUNCTION - SCREENING STRUCTURAL MODELS WITH FUNCTIONAL DATA.* Proceedings of the National Academy of Sciences of the United States of America, 1994. **91**(1): p. 113-117.
47. Berman, E.R., *Biochemistry of the eye*. 1991, New York: Plenum Press. 476.
48. McMurry, J., *Organic Chemistry*. Fifth Edition ed, ed. J. Huber. 1999, Pacific Grove: Brooks/Cole. 1284.
49. Bibette, J., F.L. Calderon, and P. Poulin, *Emulsions: basic principles.* Reports on Progress in Physics, 1999. **62**(6): p. 969-1033.
50. Claesson, P.M., et al., *Polyelectrolyte-mediated surface interactions.* Advances in Colloid and Interface Science, 2005. **114**: p. 173-187.

51. Marenduzzo, D., K. Finan, and P.R. Cook, *The depletion attraction: an underappreciated force driving cellular organization.* Journal of Cell Biology, 2006. **175**(5): p. 681-686.
52. Yodh, A.G., et al., *Entropically driven self-assembly and interaction in suspension (vol 359, pg 921, 2001).* Philosophical Transactions of the Royal Society of London Series a-Mathematical Physical and Engineering Sciences, 2001. **359**(1789): p. 2629-2629.
53. Asakura, S. and F. Oosawa, *INTERACTION BETWEEN PARTICLES SUSPENDED IN SOLUTIONS OF MACROMOLECULES.* Journal of Polymer Science, 1958. **33**(126): p. 183-192.
54. Malashkevich, V.N., et al., *The crystal structure of a five-stranded coiled coil in COMP: A prototype ion channel?* Science, 1996. **274**(5288): p. 761-765.
55. Urry, D.W., T.L. Trapane, and K.U. Prasad, *PHASE-STRUCTURE TRANSITIONS OF THE ELASTIN POLYPENTAPEPTIDE WATER-SYSTEM WITHIN THE FRAMEWORK OF COMPOSITION TEMPERATURE STUDIES.* Biopolymers, 1985. **24**(12): p. 2345-2356.
56. van Hest, J.C.M. and D.A. Tirrell, *Protein-based materials, toward a new level of structural control.* Chemical Communications, 2001(19): p. 1897-1904.
57. Petka, W.A., et al., *Reversible hydrogels from self-assembling artificial proteins.* Science, 1998. **281**(5375): p. 389-392.
58. Zhang, L.F. and A. Eisenberg, *MULTIPLE MORPHOLOGIES OF CREW-CUT AGGREGATES OF POLYSTYRENE-B-POLY(ACRYLIC ACID) BLOCK-COPOLYMERS.* Science, 1995. **268**(5218): p. 1728-1731.
59. Alexandridis, P. and R.J. Spontak, *Solvent-regulated ordering in block copolymers.* Current Opinion in Colloid & Interface Science, 1999. **4**(2): p. 130-139.
60. Astafieva, I., X.F. Zhong, and A. Eisenberg, *CRITICAL MICELLIZATION PHENOMENA IN BLOCK POLYELECTROLYTE SOLUTIONS.* Macromolecules, 1993. **26**(26): p. 7339-7352.
61. Khougaz, K., Z.S. Gao, and A. Eisenberg, *DETERMINATION OF THE CRITICAL MICELLE, CONCENTRATION OF BLOCK-COPOLYMER MICELLES BY STATIC LIGHT-SCATTERING.* Macromolecules, 1994. **27**(22): p. 6341-6346.
62. Huglin, M.B., *Light Scattering from Polymer Solutions*. 1972, London, New York: Academic Press.
63. Tuzar, Z. and P. Kratochvil, *BLOCK AND GRAFT COPOLYMER MICELLES IN SOLUTION.* Advances in Colloid and Interface Science, 1976. **6**(3): p. 201-232.
64. Tuzar, Z., et al., *BLOCK COPOLYMER MICELLES NEAR CRITICAL CONDITIONS.* Journal of Colloid and Interface Science, 1985. **105**(2): p. 372-377.
65. Zhou, Z.K. and B. Chu, *ANOMALOUS ASSOCIATION BEHAVIOR OF AN ETHYLENE-OXIDE PROPYLENE-OXIDE ABA BLOCK COPOLYMER IN WATER.* Macromolecules, 1987. **20**(12): p. 3089-3091.
66. Alexandridis, P., J.F. Holzwarth, and T.A. Hatton, *MICELLIZATION OF POLY(ETHYLENE OXIDE)-POLY(PROPYLENE OXIDE)-POLY(ETHYLENE OXIDE) TRIBLOCK COPOLYMERS IN AQUEOUS-SOLUTIONS - THERMODYNAMICS OF COPOLYMER ASSOCIATION.* Macromolecules, 1994. **27**(9): p. 2414-2425.

67. Beezer, A.E., et al., *AN INVESTIGATION OF DILUTE AQUEOUS-SOLUTION BEHAVIOR OF POLY(OXYETHYLENE) PLUS POLY(OXYPROPYLENE) PLUS POLY(OXYETHYLENE) BLOCK-COPOLYMERS.* Langmuir, 1994. **10**(11): p. 4001-4005.
68. Zhou, Z.K. and B. Chu, *LIGHT-SCATTERING STUDY ON THE ASSOCIATION BEHAVIOR OF TRIBLOCK POLYMERS OF ETHYLENE-OXIDE AND PROPYLENE-OXIDE IN AQUEOUS-SOLUTION.* Journal of Colloid and Interface Science, 1988. **126**(1): p. 171-180.
69. Alexandridis, P., *Poly(ethylene oxide) poly(propylene oxide) block copolymer surfactants.* Current Opinion in Colloid & Interface Science, 1997. **2**(5): p. 478-489.
70. Jorgensen, E.B., et al., *Effects of salts on the micellization and gelation of a triblock copolymer studied by rheology and light scattering.* Macromolecules, 1997. **30**(8): p. 2355-2364.
71. Costa, T., et al., *Complex Formation between a Fluorescently-Labeled Polyelectrolyte and a Triblock Copolymer.* Journal of Physical Chemistry B, 2009. **113**(18): p. 6205-6214.
72. Bello-Roufai, M., O. Lambert, and B. Pitard, *Relationships between the physicochemical properties of an amphiphilic triblock copolymers/DNA complexes and their intramuscular transfection efficiency.* Nucleic Acids Research, 2007. **35**(3): p. 728-739.
73. Tirumala, V.R., et al., *Well-Ordered Polymer Melts with 5 nm Lamellar Domains from Blends of a Disordered Block Copolymer and a Selectively Associating Homopolymer of Low or High Molar Mass.* Macromolecules, 2008. **41**(21): p. 7978-7985.